# POLITECNICO DI MILANO

School of Industrial and Information Engineering

Master of Science in Biomedical Engineering

Chemistry, Materials and Chemical Engineering Department "Giulio Natta"


# Development of fluorinated probes for cell tracking by 19F-MRI


Supervisor: Prof. Francesca BALDELLI BOMBELLI

Co-supervisor: Dr. Linda CHAABANE

Co-supervisor: Dr. Cristina CHIRIZZI

Master Thesis of:

Lodovico Gatti

Carrier ID: 883598



Academic Year 2019/2020

# TABLE OF CONTENTS

Table of Contents ..... 3

List of Figures ..... 5

List of Tables ..... 9

Abbreviations ..... 11

Abstract ..... 12

Sommario ..... 15

1 Introduction ..... 19

1.1 Cell-based therapies ..... 19

1.2 Cell Imaging Modalities ..... 21

1.2.1 Bioluminescence and Fluorescence optical Imaging ..... 22

1.2.2 Photoacoustic Imaging ..... 24

1.2.3 PET and SPECT ..... 24

1.2.4 Magnetic Resonance spectroscopy (MRS) and Imaging (MRI) ..... 25

1.2.5 Summary ..... 28

1.3 MRI Contrast Agents ..... 30

1.3.1 Gadolinium and Metal Chelates ..... 32

1.3.2 Iron Oxide Nanoparticles ..... 34

1.3.3 Introduction to $^{19}$F-MRI ..... 36

1.3.4 PERFECTA ..... 39

1.4 Fluorinated Nanoformulation ..... 41

1.4.1 Lipidic and Polymeric Nanoformulations ..... 42

1.4.2 PLGA-based Nanoformulations ..... 44

2 Experimental Part ..... 47

2.1 General Overview ..... 47

2.2 Materials ..... 48

2.3 Methods ..... 49

2.3.1 Nanoparticles Formulation ..... 49

2.3.2 Dynamic Light Scattering (DLS) ..... 50

2.3.3 Nanoparticle Tracking Analysis (NTA) ..... 52

2.3.4 Zeta Potential ..... 54
2.3.5 Fourier Transform Infrared (FTIR) spectroscopy ..... 56
2.3.6 Nuclear Magnetic Resonance (NMR) spectroscopy and quantitative Nuclear Magnetic Resonance (qNMR) spectroscopy ..... 58
2.3.7 Cell Culture ..... 61
2.3.8 Magnetic Resonance Imaging (MRI) ..... 62
3 Results and Discussion ..... 65
3.1 Introduction ..... 65
3.2 Nanoformulations Optimization and Protocol ..... 65
3.3 Nanoparticles Characterization ..... 71
3.3.1 Composition ..... 71
3.3.2 Colloidal stability of the PERFECTA loaded PLGA NPs ..... 74
3.3.3 $^{19}$F-NMR Analysis and Quantification ..... 81
3.4 *In Vitro* Experiment ..... 85
3.4.1 Labelling and Viability ..... 85
3.4.2 $^{19}$F-MRI ..... 87
4 Conclusions ..... 90
Supporting Materials ..... 93
Bibliography ..... 99
Ringraziamenti ..... 111

# LIST OF FIGURES

Figure 1.1: Perspective on preclinical (top) imaging modalities available for cell tracking and clinical (bottom) systems for cell imaging.[14] ..... 22
Figure 1.2: Comparison between T1 and T2 contrast in MRI; a) correlation between T2 contrast during the magnetization phase and TE (time to echo event); b) graph of T1 contrast in which the magnetization is observed in function of TR (time of repetition); c) T1 and T2 intensity levels for common structure and their grey-scale equivalent in T1W and T2W MRI; d,e) Magnetic resonance of the occipital view of a brain. T2 map (d) and T1 map (e).[30] ..... 27
Figure 1.3: Comparison between glioma cell labelled with MnO (T1 agent) and FeO (T2 agent) transplanted in a rat model. a-c) spin echo image, where the effects of both Cas on T1 and T2 are visible, d-f) R1 maps in which only the T1 effect of MnO is visible according to 1/T1 value, g-i) R2 maps in which is visible the effect of FeO according to 1/T2 value, j-l) merged maps (R1/R2) in which both labels are visible and tagged with different colours, green for MnO and red for FeO.[33] ..... 31
Figure 1.4: MRI of a brain before (left) and after (right) the administration of a Gd-chelate (Gd-DTPA) contrast agents, the bright spot is where the CA is located and highlight the presence of a tumour in the patient.[32] ..... 33
Figure 1.5: Pre-contrasted (left) and post-contrasted (right) T2-weighted MRI on inflamed mouse mammary gland tumours. The darker areas due to the negative contrast of SPIOs that accumulated in the inflamed tissue are indicated with arrows.[50] ..... 35
Figure 1.6: Examples of $^{19}F$ MRI. Murine DC cells labelled with perfluoropolyether (PFPE) and injected a) intramuscularly into the quadriceps of a mice, from left to right: 19F-MRI, H-MRI and their composition $^{19}F/^{1}H$ images. b) $^{19}F/^{1}H$ composite image of DC cell migration after hind foot pad injection. c) composite image of accumulation of DC cells injected intravenously in liver (L), spleen (S) and lungs (Lu).[59] ..... 37
Figure 1.7: PERFECTA structure and single crystal X-ray structure.[71] ..... 40
Figure 1.8: Fluorinated emulsion and nanoparticles schemes.[68] Emulsion are characterized by fluorinated compounds dispersed in a solvent and entrapped inside a lipidic or polymeric shell. Particles are more complex systems in which the PFC is dissolved with a solvent and confined with a polymeric coating stabilized with surfactants. ..... 42

Figure 1.9: Representation of the degradation of fluorinated emulsion (upper raw) and fluorinated NPs (lower raw)in the liver. Is possible to observe the disassembly of the NPs into smaller domains easily cleared by the liver respect to the bigger PFC core of the emulsions.[85] ..... 45
Figure 2.1: Schematic representation of the followed procedure for the preparation of the formulation. The oil-in-water emulsion is made mixing the aqueous phase, containing the surfactant, with the organic phase, in which PLGA and PERFECTA are dissolved. The tip sonication provides the energy needed to form the NPs, while the excess of organic solvent is let to evaporate during stirring. NPs are finally collected as pellet after centrifugation and then resuspended. ..... 49
Figure 2.2: Schematic representation of the optical configuration used by NTA systems.[92] The microscope on which the camera is mounted taken up the light scattered by NPs when it is illuminated by the light source. ..... 53
Figure 2.3 Representation of the electric double layer on a negatively charged surface and electrostatic potential function in function of the distance with emphasis on Stern layer and slipping (shear) plane.[94] ..... 55
Figure 2.4: Group frequencies and fingerprint regions in the infrared spectrum.[97] ..... 57
Figure 2.5: The energy difference between spin states as a function of the external magnetic field $B_0$.[98] ..... 59
Figure 2.6:MR imaging process that consist in the acquisition of RF signal from patient's body and its mathematical reconstruction into a 2D grey-scale image based on acquired signals. The brightness of the pixel is determined by the intensity of the RF signal emitted by the tissue voxel.[101] ..... 63
Figure 3.1: Schematic representation of the adopted protocol of the preparation of PLGA-based NPs. 1) addition of the organic phase to the aqueous phase, 2) probe sonication step, 3) mechanical agitation performed with a magnetic stir, 4) evaporation of the organic solvent at low pressure, 5) centrifugation of the obtained suspension and 6) resuspension of the pellet recovered after centrifugation. ..... 66
Figure 3.2: Fingerprint FT-IR spectra of PVA, PLGA RG 504, sodium cholate and PERFECTA. The box highlight the region chosen due to the presence of two intense peaks at 727 and 736 $cm^{-1}$ not observable for other compounds. ..... 72

Figure 3.3: FT-IR spectra of PLGA-H-NaC, PLGA-NaC, PLGA-PVA and PLGA-H-PVA formulations. The green box highlights the peaks used to verify the presence of PERFECTA (C-F bond stretching) while blue box highlights the C=O bond stretching characteristic of PLGA polymers backbone. Blue arrows point to the region characteristic of C-H bonds of PVA and sodium cholate. ..... 72
Figure 3.4: $^{19}$F-NMR spectra of PERFECTA and TFA (standard for quantification). The sharpness of the PERFECTA peak (-73.3 ppm) confirms that no chemical modification occurs during formulation. ..... 73
Figure 3.5: 19F-NMR spectra of PERFECTA and TFA acquired using a wider window for investigation of impurities inside the formulation and to verify the absence of artefacts raised from the cut-off effects at the extremities of the window. ..... 74
Figure 3.6: Hydrodynamic diameter of the four formulations (upper) and PDI measurements (lower) over three days. ..... 75
Figure 3.7: Correlation function (left column) and unweighted size distribution (right column) for nanoformulation administered to microglial murine BV-2 cells line taken at three different time points and 90°. ..... 77
Figure 3.8: NTA size distributions of the obtained formulations performed with NanoSight NS 300. The red profile represents the concentration profile of the NPs as a function of the hydrodynamic radius. ..... 79
Figure 3.9:Zeta-potential distribution of NPs in dilution 1:50 in 1mM NaCl solution. ..... 80
Figure 3.10: Zeta potential distribution for PLGA-H-PVA and PLGA-H-NaC formulation diluted 1:50 in mQw to verify the shielding effects of $Na^+$ and $Cl^-$ atoms on deprotonated carboxylic groups and alcohol groups of PLGA, sodium cholate and PVA. ..... 81
Figure 3.11: 19F-qNMR spectra of PLGA-H-PVA formulation with integral values used for the quantification of fluorine atoms in the formulation. The integral value of PERFECTA is normalized according to the value obtained from the standard, the normalization is performed by the software when the integral areas are taken. ..... 83
Figure 3.12: Viability of immortalized BV-2 cells labelled with different formulations performed with trypan blue exclusion assay. Control (H2O) and Control (PBS) are cultures in which the same volume added for each formulation was replaced with mQw or PBS... 86
Figure 3.13: Positions of the cells culture labelled with the different formulations inside the phantom and merged MR images of 19F (red) and 1H (gray). The signal around the sample

4 is due the high intensity obtained for the most concentrated reference (5x10^19 atoms) that is enlarged by increasing the intensity scale. ..... 88
Figure 0.1:Hydrodynamic diameters of the four formulations (upper) and PDI measurements (lower) over three days. ..... 93
Figure 0.2: Correlation function (left column) and unweighted size distribution (right column) for nanoformulations administered to cells for the first in vitro experiment at three different time points and 90°. ..... 94
Figure 0.3: Viability of immortalized BV-2 cells labelled with different formulations performed with trypan blue exclusion assay. Control (H2O) and Control (PBS) are cultures in which the same volume added for each formulation was replaced with mQw or PBS... 96
Figure 0.4: Positions of the cells culture labelled with the different formulations inside the phantom and merged MR images of 19F (red) and 1H (gray). ..... 96

# LIST OF TABLES

Table 1.1: List of contrast agents available for direct cell labelling and cells succefully labeled with them. ..... 28
Table 1.2: System available for cell imaging with their key features ..... 29
Table 1.3: List of main PFCs used for cells labelling with major properties and primary applications reported in literature (PFPE: perfluoropolyether, PFOB: perfluorooctyl bromide, PFCE: perfluoro-15-crown-5-ether). The magnetic properties as chemical shifts and relaxation times are related to formulated compounds while for relaxation times is reported the intensity of the magnetic field with which the measures were performed. ..... 39
Table 3.1: Nanoformulations proposed in this work: ..... 66
Table 3.2: PDI and hydrodynamic diameters of PLGA-NaC formulations at different PLGA/PERFECTA ratios. Values are expressed as mean value of the measures obtained over two weeks acquisition, SD is calculated on same data obtained at different time points over two weeks ..... 67
Table 3.3: Fluorine quantification obtained through $^{19}F$ qNMR of PLGA-NaC formulations at different PLGA/PERFECTA ratios. Theorical $^{19}F$ atoms are the number of fluorine atoms added at the beginning of the formulation procedure and equivalent to 50 mg, 20 mg and 10 mg of PERFECTA, respectively. ..... 68
Table 3.4: DLS and $^{19}F$-qNMR data for PLGA-NaC formulations with and without melting of PERFECTA before its addition to the organic phase. ..... 69
Table 3.5:Measure of hydrodynamic diameters and PDI values for the obtained formulations. Results are expressed as mean values over three time points. SD are calculated on same data. ..... 75
Table 3.6: Mean hydrodynamic diameter, standard deviation and mode obtained from NTA measurement. The SD values expressed are related to the broadness of the gaussian curve characteristic for the size distribution of these NPs. These values provide an idea of the polydispersity of the NPs. ..... 78
Table 3.7: Mean Zeta-potential values, standard deviation and conductivity of nanoparticles measured in a dilution 1:50 (V7V) in 1 mM NaCl solution. ..... 79
Table 3.8: Mean Zeta-potential values, standard deviation and conductivity of NPs diluted 1:50 in mQw. ..... 81

Table 3.9: Fluorine content and encapsulation efficiency measured through $^{19}$F-NMR of the nanoformulation proposed. Theorical $^{19}$F atoms are the number of fluorine atoms added at the beginning of the formulation procedure and equivalent to 30 mg of PERFECTA. ..... 83
Table 3.10: Measures of NP concentration (from NTA measurements) and fluorine concentration (from $^{19}$F-NMR) integrated to obtain the value of fluorine content for nanoparticle ..... 84
Table 3.11: SNR values related to the MRI acquisition on 300 000 BV-2 cells labelled with the different formulations and references. For two formulations, the collected cells were limited to 120 000 (*) and 160 000 cells (**). SNR values below 4 are considered as not detectable (nd). ..... 89
Table 0.1: Fluorine content and encapsulation efficiency measured through 19F-NMR of the nanoformulation proposed. Theorical 19F atoms are the number of fluorine atoms added at the beginning of the formulation procedure and equivalent to 20 mg of PERFECTA. ..... 95
Table 0.2: SNR values related to the MRI acquisition on 200 000 BV-2 cells labelled with the different formulations and references. SNR values below 4 are considered as not detectable (nd). ..... 97

# ABBREVIATIONS

| | |
|---|---|
| ASCs | Adipose Stem Cells |
| BLI | Bioluminescence Imaging |
| BM-MSCs | Bone Marrow Mesenchymal Stem Cells |
| CARs | Chimeric Antigen Receptors |
| CAs | Contrast Agents |
| CEST | Chemical Exchange Saturation Transfer |
| CT | Computed Tomography |
| DCs | Dendritic Cells |
| DH | hydrodynamic diameter |
| DLS | Dynamic light scattering |
| EDL | electronic double layer |
| EMA | European Medicines Agency |
| ESCs | Embryonic Stem Cells |
| EtOAc | Ethyl acetate |
| FDA | Food and Drug Administration |
| FDG | Fludeoxyglucose |
| FLI | Fluorescent Imaging |
| FT-IR | Fourier Transformed Infrared spectroscopy |
| GBCAs | Gadolinium Based Contrast Agents |
| IPSCs | Induced Pluripotency Stem Cells |
| mQw | MilliQ water |
| MR | Magnetic Resonance |
| MRI | Magnetic Resonance Imaging |
| MRS | magnetic resonance spectroscopy |
| MSCs | Mesenchymal Stem Cells |
| NIR | Near-Infrared |
| NK | Natural Killer T-Cells |
| NMR | Nuclear Magnetic Resonance |
| NPs | Nanoparticles |
| NTA | nanoparticle tracking analysis |
| PAI | Photoacoustic Imaging |

| | |
|---|---|
| PBS | Phosphate buffer solution |
| PD | Proton density |
| PEG | Polyethylene Glycol |
| PERFECTA | suPERFluorinatEdContrasT Agent |
| PET | Positron emission Tomography |
| PFA | paraformaldehyde |
| PFCE | Perfluoro-15-crown-5-ether |
| PFCs | Perfluorocarbons |
| PFOB | Perfluorooctyl Bromide |
| PFPE | Perfluoropolyether |
| PGA | Polyglycolic acid |
| PLA | Polylactic acid |
| PLGA | Poly(lactic-co-glycolic Acid) |
| PVA | Polyvinyl Alcohol |
| QDs | Quantum Dots |
| qNMR | quantitative Nuclear magnetic resonance |
| RES | Reticuloendothelial System |
| RF | Radiofrequency |
| SCs | Stem Cells |
| SNR | signal-to-noise ratio |
| Sodium Cholate | NaC (DS-Na) |
| SPECT | Single Photon Emission Computed Tomography |
| SPIO | Superparamagnetic Iron Oxide |
| T1W | T1-weighted |
| T2W | T2-weighted |
| TE | echo time |
| TFA | Trifluoroacetic acid |
| TR | Repetition Time |
| TSPSCs | Tissue Specific Progenitor Stem Cells |

# ABSTRACT

A fundamental branch of regenerative medicine is based on the use of selected cells able to promote a therapeutic effect once transplanted into the patient's body. These therapeutic cells are generally either stem cells or pluripotent cells or immune cells. Despite the incredible results obtained in preclinical trials, in fact over 6000 registered clinical studies have been done with approval from the major international certification institutes (FDA and EMA), their application is still far from being common and limited due to their long-term effects and toxicity risks, also related to off-target distributions of these cells. Thus, a non-invasive imaging technique able to localize cells distribution could be a key tool to support the development of such therapeutic approach.

To track cells, different labelling systems have been developed for various imaging techniques. Bioluminescence (BLI), fluorescence (FLI) or photoacoustic imaging (PAI) have proven to have a great potentiality in preclinical studies but, due to their limited depth penetration in the soft tissues, are not adapted for clinical studies. PET and SPECT imaging, based on the use of radionuclides, are efficient in terms of penetration, but their low spatial resolution, short half-life, lack of detection of anatomical images and necessity to expose patients to ionizing radiations limited the development of these systems for cell tracking.

MRI proved to be the most promising tool as anatomical and functional data could be obtained without depth penetration limits and the use of radio-active contrast agents. However, MRI sensibility is limited. For cell labelling, conventional available MRI contrast agents, as gadolinium-chelates and superparamagnetic nanoparticles, have been widely investigated but showing several limitations due to toxicity and non-specific signal detection. In the last decade, $^{19}$F-MRI has been proposed as a complementary technique to $^{1}$H-MRI, for in vivo cell tracking since the lack of organic fluorine in soft tissues labelled cells are specifically detected without background signal.

To improve $^{19}$F-MRI sensibility, highly fluorinated molecules, i.e. perfluorocarbons, are essential to reach sufficiently high concentrations of $^{19}$F within cells. Perfluorocarbons such as PFPE, PFOB and PFCE were mainly investigated for cell labelling. More recently, a



*Keywords: Fluorinated probes, PLGA NPs, in vitro cell labelling, $^{19}$F-MRI*

superfluorinated molecule called PERFECTA has been successfully used as a sensitive $^{19}$F-MRI probe and was chosen in the present thesis work. PERFECTA is easily synthesized in high amounts, well tolerated by cells and the presence of 36 equivalent fluorine atoms provide a single and sharp signal in $^{19}$F-MRI.

To enable cell labelling, PERFECTA must be formulated either in an emulsion or in a NP to be dispersed in an aqueous solution in order to be applied in a cellular environment. Emulsions, based on the stabilization of fluorinated compounds with polymers and lipids, were initially developed and, although these systems are subject to colloidal instability, they are still widely used, especially in preclinical research. Recently, PLGA nanoparticles containing a perfluorocarbon core and stabilized with biocompatible surfactants have acquired interests thanks to their biocompatibility and biodegradability as well as for their modular structure making the formulation easily adaptable to specific needs.

For these reasons, PLGA has been chosen as carrier for PERFECTA in the present thesis work. For the stabilization of PLGA nanoparticles, a zwitterionic surfactant (polyvinyl alcohol, PVA) or an ionic surfactant (sodium cholate, NaC) were both evaluated for their potential impact on cell labelling efficiency.

Four different formulations, PLGA-H-PVA, PLGA-H-NaC, PLGA-PVA and PLGA-NaC, using the above mentioned surfactants and two PLGA polymers differently functionalized, were developed and chemically characterized by Fourier transformed infrared spectroscopy (FTIR), $^{19}$F nuclear magnetic resonance, ($^{19}$F-NMR) and their colloidal stability was analysed by dynamic light scattering (DLS), nanoparticle tracking analysis (NTA) and zeta potential measurement.

Following the optimization of these formulations to obtain stable NP with a high encapsulation of PERFECTA, NPs were used to label murine microglial cells (BV-2) to study their cytocompatibility and labelling efficiency through analysis performed with $^{19}$F-MRI.

A first protocol was developed and optimized on PLGA-NaC NPs and subsequently adapted to the other proposed formulations. The analysis with FTIR confirmed the composition of the NPs and the encapsulation of PERFECTA inside PLGA nanoparticles without the use of fluorinated solvents. The $^{19}$F-NMR also demonstrated that no chemical change of



*Keywords: Fluorinated probes, PLGA NPs, in vitro cell labelling, $^{19}$F-MRI*

PERFECTA occurred during NPs formulation. The formulation optimization allowed to improve nanoparticles stability in the aqueous environment up to two weeks and to achieve a high encapsulation efficiency to label cells suitable for MRI sensibility.

All the formulation stabilized with either NaC and PVA, used for *in vitro* labelling experiments, have a PDI values lower than 0.2 and a size of approximately 100 nm and 200 nm, respectively, and confirmed by NTA measurements. Zeta-potential measurements showed a steric stabilization of PVA, for which a weak negative charge of - 5 mV was measured, and an electrostatic stabilization was obtained with NaC, with a superficial charge of about - 40 mV. The $^{19}$F-NMR analysis confirmed the concentration of fluorine atoms between $1.39 \times 10^{20}$ and $2.96 \times 10^{20}$ $^{19}$F/ml, corresponding to an encapsulation efficiency between 22% and 46%. With these formulations, cells could be incubated with a suitable concentration $1 \times 10^{14}$ $^{19}$F/cell.

Following 4 hours of incubation, an excellent cell's viability was obtained (85% - 98%) almost similar to normal conditions (93% - 95%). The same cells were subsequently fixed and observed in MRI showing a higher cellular uptake with PLGA-H-NaC NPs compared to PLGA-H-PVA, PLGA-PVA and PLGA-NaC.

To conclude, the developed nanoparticles could be internalized by murine microglia cells with an uptake sufficient for MRI. Further investigations are needed to improve cellular labelling in non-phagocytic cells, such as T-cells and stem cells. The use of a PLGA functionalised with a fluorophore could also permit the development of bimodal imaging systems exploiting the modularity of the formulation protocol.



*Keywords: Fluorinated probes, PLGA NPs, in vitro cell labelling, $^{19}$F-MRI*

# SOMMARIO

Un ramo fondamentale della medicina rigenerativa si basa sull'utilizzo di cellule in grado di promuovere un effetto terapeutico una volta trapiantate nel corpo del paziente. Queste cellule terapeutiche sono generalmente cellule staminali o pluripotenti o cellule del sistema immunitario. Nonostante gli incredibili risultati ottenuti in fase di sperimentazione preclinica, infatti alcuni tra gli oltre 6000 studi clinici registrati hanno ottenuto l'approvazione dai maggiori organi certificatori internazionali (FDA e EMA), l'applicazione di queste terapie è ancora lontana dal diventare comune ed è limitata dalla mancanza di informazioni riguardanti gli effetti a lungo termine ed ai rischi di tossicità, legati anche alla biodistribuzione di queste cellule in distretti corporei non di loro interesse.

Negli anni sono stati studiati sistemi di labelling cellulare per diverse tecniche di imaging. La bioluminescenza (BLI), la fluorescenza (FLI) e l'imaging fotoacustico (PAI) hanno dimostrato di avere una ottima applicabilità in studi preclinici ma, a causa della limitata penetrazione nei tessuti molli, non altrettanto buoni in clinica. La PET e la SPECT, basati sull'utilizzo di radionuclidi, non hanno limiti di penetrazione ma l'impossibilità di ottenere dettagli anatomici, la corta half-life, la bassa risoluzione spaziale e l'esposizione dei pazienti a radiazioni ionizzanti ne hanno limitato lo sviluppo in campo cellulare.

La MRI ha dimostrato di essere la più promettente permettendo l'acquisizione contemporanea di dettagli anatomici e funzionali senza limiti di penetrazioni e utilizzando agenti di contrasto non radioattivi. Anche se la sensibilità è limitata. Per il labelling cellulare sono stati ampiamente studiati mezzi di contrasto convenzionali, come ioni di gadolinio chelati e nanoparticelle superparamagnetiche, ma hanno dimostrato seri problemi di tossicità e di non specificità nel rilevamento del segnale. Negli ultimi anni la $^{19}$F-MRI ha dimostrato di essere una ottima tecnica complementare da affiancare alla $^{1}$H-MRI, grazie ad una sensibilità paragonabile, per il tracking di cellule in vivo grazie all'assenza di fluoro nei tessuti molli, che permette di rilevare in maniera distintiva le cellule marcate.

Allo scopo di migliorare la sensibilità in $^{19}$F-MRI, molecole ad alto contenuto di fluoro, i.e. perfluorocarburi, sono necessari per raggiungere una concentrazione sufficientemente alta



*Parole chiave: Sonde fluorurate, PLGA NPs, labelling cellulare in vitro, $^{19}$F-MRI*

di $^{19}F$ nelle cellule. Perfluorocarburi come PFPE, PFOB e PFCE sono stati studiati per il labelling cellulare. Recentemente, una molecola super fluorurata chiamata PERFECTA è stata impiegata con risultati positivi come agente di contrasto in $^{19}F$-MRI ed è stata scelta per il presente studio. PERFECTA è facilmente sintetizzabile in elevate quantità, è ben tollerata dalle cellule e la presenza di 36 atomi di fluoro equivalenti permette di osservare un singolo e chiaro segnale in $^{19}F$-MRI.

Per permettere il labelling cellulare è necessario formulare PERFECTA in emulsioni o NP per poi essere dispersa in una soluzione acquosa e impiegata in ambiente cellulare. Le emulsioni, basate sulla stabilizzazione dei composti fluorurati con polimeri o lipidi, si sono rivelate inizialmente adatte allo sviluppo di sistemi di labelling e, nonostante questi sistemi siano soggetti a fenomeni di instabilità colloidale, sono tuttora molto utilizzati, soprattutto in ricerca preclinica. Recentemente sono stati investigate nanoparticelle di PLGA contenenti un core di PFC e stabilizzati da surfactanti biocompatibili si sono dimostrati interessanti, principalmente grazie alla loro biocompatibilità, biodegradabilità e alla struttura modulare che permette di adattare la formulazione alle richieste specifiche con minime modifiche al protocollo.

Per queste ragioni è stato scelto di usare il PLGA come carrier per PERFECTA in questo lavoro di tesi. Per la stabilizzazione delle nanoparticelle di PLGA sono stati proposti un surfactante zwitterionico (Alcol polivinilico, PVA) o uno ionico (colato di sodio, NaC), al fine di indagare gli effetti sull'internalizzazione cellulare di queste nanoparticelle.

Quattro differenti formulazioni, PLGA-H-PVA, PLGA-H-NaC, PLGA-PVA e PLGA-NaC, sono state ottenute, usando i due surfactanti menzionati precedentemente e due polimeri di PLGA funzionalizzati diversamente, e caratterizzate da un punto di vista chimico, tramite spettroscopia infrarossa e risonanza magnetica nucleare dell'atomo $^{19}F$, ed da un punto di vista di stabilità colloidale con diffusione dinamica della luce (DLS) e analisi del tracciamento di nanoparticelle (NTA) e Zeta-potential.

Ottimizzato il protocollo di formulazione per ottenere NP stabili con una elevata efficienza di incapsulamento di PERFECTA, queste sono state usate per marcare cellule murine microgliali (BV-2) per studiare la citocompatibilità e l'efficienza di labelling tramite analisi svolte in $^{19}F$-MRI.



*Parole chiave: Sonde fluorurate, PLGA NPs, labelling cellulare in vitro, $^{19}F$-MRI*

Un primo protocollo è stato sviluppato e ottimizzato sulla formulazione PLGA-NaC e successivamente adattato alle altre tre formulazioni proposte. L'analisi IR ha confermato la composizione delle NPs e dimostrato l'incapsulamento di PERFECTA all'interno delle nanoparticelle di PLGA senza l'utilizzo di solventi fluorurati. Tramite $^{19}$F-NMR si è verificato che PERFECTA non subisca modificazioni chimiche durante la formulazione. L'ottimizzazione del protocollo di sintesi ha la stabilità delle NPs in ambiente acquoso oltre le due settimane e di raggiungere un'efficienza di incapsulazione sufficiente per marcare le cellule con una concentrazione sufficiente tale da avere sensibilità in MRI.

Tutte le formulazioni stabilizzate con NaC e con PVA, usate per gli esperimenti di labelling *in vitro*, hanno un valore di PDI inferiore allo 0.2, e una dimensione approssimativamente di 100 nm e 200 nm, rispettivamente, ulteriormente confermate dalle misure NTA. Le misure di Zeta-potential mostrano una stabilizzazione sterica ad opera della PVA, le cui NPs hanno un valore leggermente negativo di -5 mV, ed un effetto di stabilizzazione elettrostatica per quelle con NaC, risultando in NPs con una carica superficiale di -40 mV. Le analisi in $^{19}$F-NMR hanno confermato una concentrazione di atomi di fluoro compresa tra $1.39x10^{20}$ e $2.94x10^{20}$ $^{19}$F/ml, corrispondenti ad una efficienza di incapsulazione che varia tra il 22% e il 46%. Con queste formulazioni è stato possibile marcare le cellule con una concentrazione di $1x10^{14}$ $^{19}$F/cellula.

In seguito a 4 ore di incubazione, sono stati ottenuti ottimi risultati di vitalità (85% - 98%), confrontabili con quelli ottenuti in condizioni di incubazione normali (93% - 95%). Le stesse cellule sono state fissate e osservate in MRI dimostrando una elevata fagocitosi delle NPs PLGA-H-NaC rispetto alle NPs PLGA-H-PVA, PLGA-PVA e PLGA-NaC.

In conclusione, le nanoparticelle sviluppate sono state internalizzate da cellule fagocitarie in quantità sufficienti per la MRI. Ulteriori ricerche e ottimizzazioni sono necessarie al fine di migliorare il labelling cellulare per cellule non-fagocitarie, come i linfociti T e le cellule staminali. Mentre, l'utilizzo di un PLGA funzionalizzato con un fluoroforo permetterebbe di ottenere sistemi bimodali sfruttando la modularità del protocollo di formulazione.



*Parole chiave: Sonde fluorurate, PLGA NPs, labelling cellulare in vitro, $^{19}$F-MRI*

# 1 INTRODUCTION

## 1.1 CELL-BASED THERAPIES

The need of non-invasive tools for *in vivo* cell tracking rises from the increasing interest and promising results obtained in last decades from regenerative medicine, a therapeutic approach in which the capacity of specific cells to regenerate diseased tissues are explored. The term "regenerative medicine" was first used by Leland Kaiser in 1992 in a paper entitled "The future of multihospital systems". In that paper Kaiser stated "A new branch of medicine will develop that attempts to change the course of chronic disease and in many instances will regenerate tired and failing organs systems" [1], a hope that in last three decades has seen the first application in clinical trials raising to more than 6000 registered clinical studies on clinicaltrials.gov last year for stem cells therapies.[2] A core branch of regenerative medicine are the cell-based therapies, in which the therapeutic effect is provided by stem cells (SCs) or immune cells.

From a regenerative point of view SCs can be divided into four different types as a function of their potency and applicability: i) embryonic stem cells (ESCs), ii) induced pluripotency stem cells (iPSCs), iii) mesenchymal stem cells (MSCs) and iv) tissues specific progenitor stem cells (TSPSCs). ESCs are the most interesting because they have a greater differentiability and potentially can be used to generate any other cell phenotype, those cells can only be collected from an embryo and regardless of their beneficial effect the ethical problems related to their harvest is a key point that limits the utilization of ESCs. Another problem raised in last years that prevents the application of ESCs to clinical research is the high risk associated to the evolution of ESCs into teratomas form.[3], [4]

From ethical restriction and high risk associated to ESCs researcher tried to induce the pluripotency reprogramming adult cells into stem-like cells. Between 2006 and 2009 the first results were obtained, and the so obtained cells were called induced pluripotency stem cells, iPSCs. Similarly to ESCs they are pluripotent and can be induced to differentiate into any trilaminar germinal line, the ethical problem was overcome as they are obtained from manipulating adult cells and with the possibility to directly harvest from patients and the

availability issue was also solved. However, since their first application genetic instabilities and tumorigenic features limited their clinical translation.

Mesenchymal stem cells were discovered in 1909 but only in 1970 they were identified as multipotent and since 1990 their potential differentiation capacity and regenerative abilities started to be studied for clinical purposes.[3] MSCs can be directly isolated from SC niches present in different adult tissues as bone marrow, adipose tissue, umbilical cord, dental pulp and skin.[5], [6] Their multipotency and availability make them the perfect candidate for cell-based therapies as they do not have ethical issue related to their collection and present minor adverse effects when compared with ESCs and iPSCs. Recent studies demonstrate that the beneficial properties of MSCs are related to tissue of origin, isolation and application procedures. For clinical purpose, MSCs derived from bone marrow (BM) and adipose tissues (ASCs) are the most promising, however BM-MSCs were excluded due to the limited number of cells available and fatal complications related to their collection. ASCs demonstrated excellent proliferation and differentiation in the trilineage cell lines, suitable for both autologous and allogenic transplantation and can easily be collected, even in large number, through liposuction.[7]

Tissue specific progenitor SCs possess the lower potency above all, as they can differentiate in few types of cells. However, application of these cells are reported in the treatment of diseases in which the maintenance of the tissue homeostasis is required even if their application is limited by the low collectable number of these cells from niches in which they reside. These reasons lead to prefer the use of MSCs rather than tissue specific progenitor SCs.[8]

Immune cells have seen a major role in cell-based immunotherapies and in cancer therapies with promising results. Among all immune cells the most relevant, for therapeutic purposes, are: i) T cells, ii) natural killer (NK) cells and iii) dendritic cells (DCs).[9] DCs was firstly investigated for cancer therapies for their antigen presenting behaviour and the ability to regulate the adaptive immune response, they are developed as vaccine against some tumoral forms.

T cells and NK cells have the ability to actively target cancer cells and stimulate an immune response against them, for T cells, or directly kill them, in case of NK cells. T lymphocytes and NK cells need to be engineered in order to recognize cancer cells, more recently,

chimeric antigen receptor (CARs) [10] was developed to enhance the selectivity to target tumour cells and stimulate the immune system against malignant formation. On other side, manipulation of NK cells can increase the cancer cells detection, but recent studies demonstrate a reduction in their therapeutic potency.[11]

Cell-based therapies have provided incredible results in preclinical studies and recently also in clinical field as recently approved by FDA and EMA. However, collateral effects were reported caused by off-target distribution of these cells in the body following administration and long-term risks are still unknown. To overcome at least one of these issues, in 2008 the Cell, Tissues and Gene Therapies Advisory Committee of the FDA Center for Biologics Evaluation and Research asked for the development of labelling methods able to track cells in vivo.[12]

## 1.2 Cell Imaging Modalities

Since many years, several imaging approaches are investigated to image cells in vivo such as: i) bioluminescence imaging (BLI), ii) fluorescent imaging (FLI), iii) photoacoustic imaging (PAI), iv) positron emission tomography (PET), v) single photon emission computed tomography (SPECT), vi) computed tomography (CT) and vii) magnetic resonance imaging (MRI).[13] For each imaging modality (Fig. 1.1) different labelling probes were developed with proper advantage and limitations.

The main challenge relies on the development of labelling systems able to be detectable in vivo, in real time and safe. The development of labelling systems started from clinically available contrast agents (CAs) optimized for in vivo cell tracking, however with several limitations. Upon the CAs type, the main problems were photo-blenching, tissue penetration depth limits, interference with tissues, metabolic degradation or chemical instabilities and a poor transfection efficiency leading to low detection sensitivity.

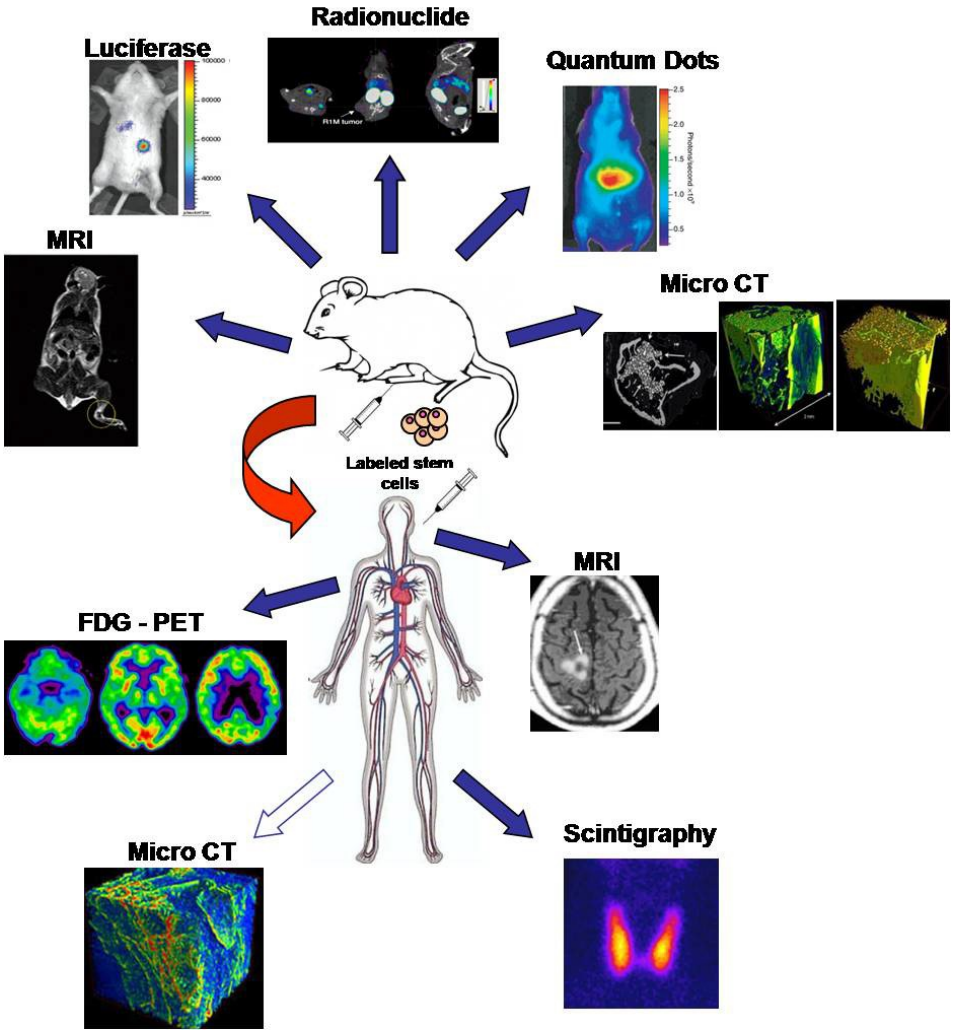


*Figure 1.1: Perspective on preclinical (top) imaging modalities available for cell tracking and clinical (bottom) systems for cell imaging.*[14]

### 1.2.1 Bioluminescence and Fluorescence optical Imaging

Bioluminescence (BLI) and fluorescence (FLI) imaging are molecular optical imaging techniques based on light emission, both had a rapid development for in vivo imaging with numerous applications principally due to their low cost and high throughput.

BLI is based on the light emitted in the 530-640 nm wavelength range (North America firefly luciferase) [15] by the oxidative reaction between the luciferase enzyme and the luciferin substrate.[16] Bioluminescence is applied as cell culture assays, for gene transfection

principally, and in biological environment studies like apoptosis, protein-protein interaction, gene expression and tumorigenesis. Since mammalian cells have no luminescence properties, BLI has a low background signal and has also the advantage to be sensitive with a high tissue penetration depth and highly biocompatible.[17] In order to be tracked, cells need to be engineered with a gene encoding for luciferase enzyme while the luciferin need to be administered at the moment of the analysis, the genetic manipulation of SCs and immune cells could introduce instabilities in genetic code with the associated risk to enhance tumorigenic behaviour or introduce phenotype alterations of these cells increasing the risk associated in the application of this tracking modality.[18] Actually the main limit to this application is the low tissues penetration of few millimetres making this modality applicable only in superficial tissues.

FLI is based on the application of fluorophores able to emit light when excited by UV light, it is largely diffused for cytofluorimetric analysis, in vitro cell imaging and immunofluorescence microscopy. Different types of labels are available as organic dyes, quantum dots and biological fluorophores; according to the specific application each of these can be the most suitable: QDs are quite photostable and their emission wavelengths fall in a wide wavelength range, but being constituted of metals there are toxicity issues related to their use, biological fluorophores are usually proteins, thus their application can be quite complex with respect to other systems due to the administration of the gene encoding for the protein, while organic dyes are often highly susceptible to photobleaching.

Organic dyes are used for several imaging applications such as vascular mapping, tissue perfusion as well as inflammation, atherosclerosis, protein activity and apoptosis [19], although tissue penetration is limited to few centimetres similarly to BLI systems.

Recent progress in BLI and FLI has been reached combining the two technologies trying to improve tissue penetration depth with NIR fluorophores applied to BLI [20], but despite the encouraging results for in vivo cell tracking their application in clinics is still unreached.

### 1.2.2 Photoacoustic Imaging

The operative principle of photoacoustic imaging (PAI) consists in a nanosecond light pulse able to generate a transient thermoelastic expansion in light-adsorbing structures, this expansion generates ultrasound waves detected and resolved into an image.[21] First application in biomedical imaging of PAI was seen in mid 1990s, but only a decade later the first *in vivo* images were obtained.[22] This system can be used without the administration of exogenous CAs using biological chromophores like haemoglobin, lipids, melanin and water. Beyond preclinical interests, several clinical applications were proposed, as: breast tumour detection, structural and functional imaging of skin and skin burn, in cardiovascular imaging of atheromatous plaques, macular degeneration and diabetic retinopathy in ophthalmology.[22], [23]

Being based on optical microscopy, as for BLI and FLI, PAI has limitations in tissue penetration, this issue is enhanced by the acoustic attenuation in soft tissues for which light attenuation is also critical. To increase the performance, exogenous CAs such as organic dyes, metallic nanorods/shells and nanoparticles are used as they are characterized by absorption wavelengths in the NIR where tissue penetration is greater.[22], [24]

The penetration depth of PAI is proportional to the excitation energy of the electromagnetic wave, with limitation due to safety reasons. Due to attenuation in soft tissues the theorical deep limit reachable by PAI systems is around 10 cm but this penetration can be reached with a consequent lost in spatial resolution due to a trade-off between these two features.[23]

### 1.2.3 PET and SPECT

Positron emission tomography (PET) is based on the annihilation reaction between a positron, emitted by a radionuclide, and electrons of neighbouring atoms, the reaction produces two gamma rays that travel in opposite direction up to a detector. The data collected are then reconstructed into an image.[25] Almost the same principle is applied for SPECT imaging which detects the emission of gamma ray photons.

PET and SPECT were largely developed for clinical diagnosis and it has been demonstrated that they are suitable to *in vivo* cell tracking thanks to the unlimited tissue penetration and high sensitivity. The main disadvantage of PET and SPECT is the short half-life of radioisotopes that is generally in the range of few hours, moreover it requires a second imaging modality to obtain anatomical features for localizing the radiations.[26] Although their high sensitivity, PET and SPECT have a low spatial resolution that limits their use for cell tracking.[3]

These technologies have been used for many applications from molecular imaging to clinical investigations of several diseases. They employ a wide number of radiolabels functionalized to be selective for specific cells [27], these labels are generally small (180 Da for 18F-FDG) to have a higher cellular uptake. Furthermore, these techniques require long-term acquisitions due to the radiolabel decay times (8-24h) [28], so the number of exams a patient can do without risks is limited due to the long radiation exposure needed to make the analysis.

### 1.2.4 Magnetic Resonance spectroscopy (MRS) and Imaging (MRI)

Magnetic resonance is based on the polarization of certain atoms under a magnetic field ($B_0$). Following a given radiofrequency (RF) impulse, these atoms absorbs the RF energy that generates a spin polarization which produces an RF signal in a radio frequency coil and thereby can be detected. These atoms return to their equilibrium state with specific movements of spin and their duration is characterized by relaxation times correlated to the magnetic field orientations, chemical composition and their environment: T1, the longitudinal component related to spin-lattice interaction and T2, transversal component related to spin-spin interaction.[29]

Nuclear magnetic resonance (NMR) is a spectroscopic analytical tool in which the resonance frequencies of atoms (usually $^{1}H$, $^{13}C$, $^{15}N$) are investigated. The information content is provided by resonance peaks, characteristics for each atom and its chemical environment. NMR is widely used to determine the chemical structure of a sample by chemical shift assignment.

For imaging, the hydrogen nucleus (a single proton) is mainly used since it is the most sensitive and abundant atom in tissues. Moreover, MRI has the ability to provide multicontrast images reflecting the tissue composition and structure thanks to tissue intrinsic longitudinal relaxivity (T1), transversal relaxivity (T2) and proton density (PD). In PD-weighted image the contrast effect arises from the concentration of protons, usually hydrogen atoms. Tissues rich in water (high concentration of hydrogens) produce strong signals resulting in brighter spot. T1 contrast explores the gradual recovery of spin magnetization following a brief RF impulse and the related signal depends on the repetition time (TR) at which the data are acquired. T2 contrast is related to the transversal relaxation time for which the signal is loss due to the rapid spin dephasing. In Fig. 1.2 is possible to see the differences between T1-weighted (T1W) and T2-weighted (T2W) images of human brain in which the structural differentiations of the cerebral fluid, white and grey matters are clearly observed. This multicontrast capacity of MRI is a key tool commonly used to detect pathological tissues.[30]

MRI is a well-established diagnostic tool with key advantages also for in vivo cell tracking with respect to the other imaging techniques: its tissue penetration, it does not need to use radioactive agents provides high anatomical details and spatial resolution, and is non-invasive allowing longitudinal studies. To further enhance the contrast, CAs are also used to provide additional functional characteristics as vascularization or tissue perfusion enabling functional imaging.

In the last two decades the increasing interest for MRI-based cell tracking applications has led researchers to focus on this technology for which the only limit is its low sensibility. A variety of contrast agents were proposed as labels to track phagocytic cells, stem cells and immune cells like T-cells.

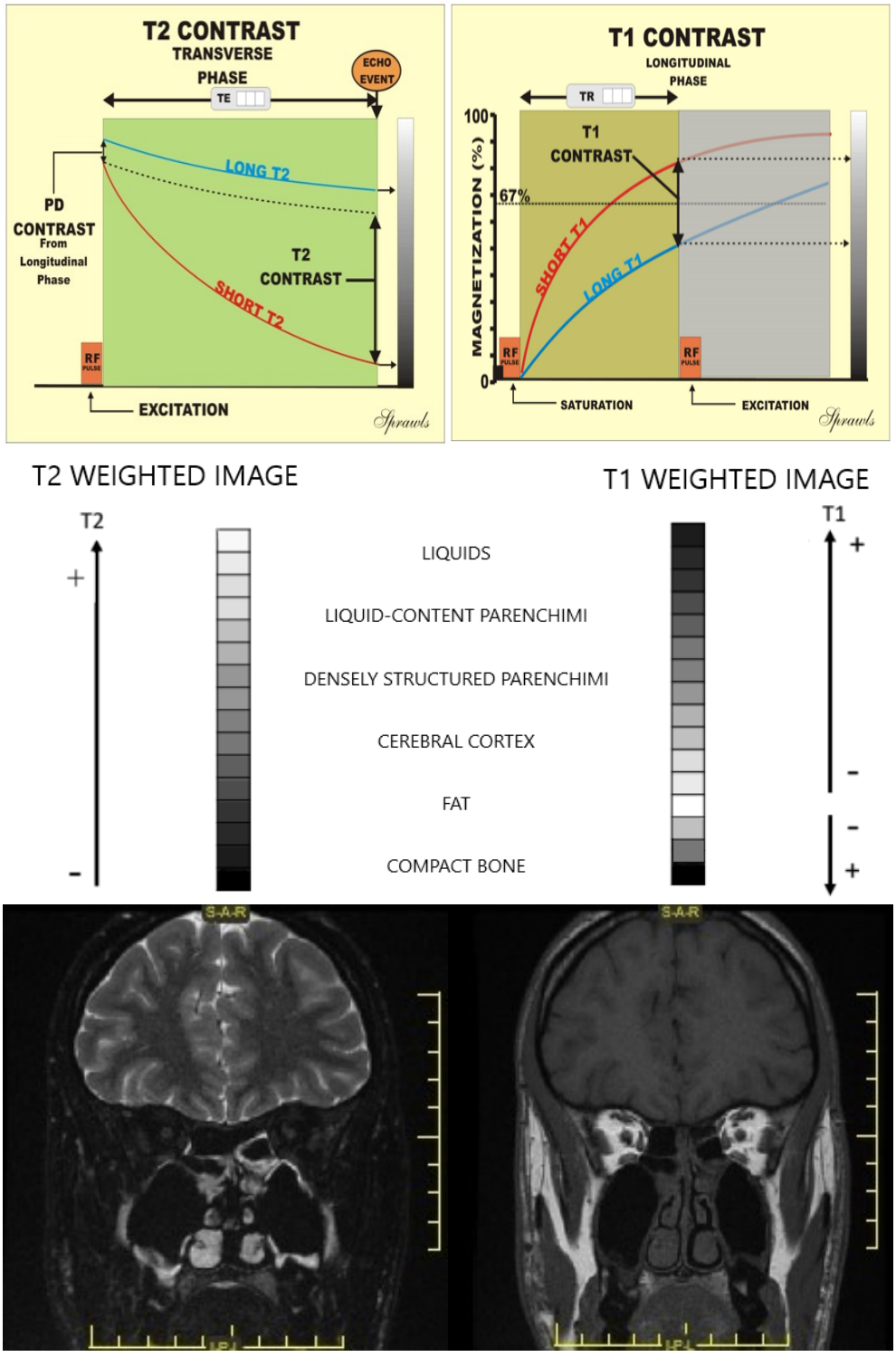


*Figure 1.2: Comparison between T1 and T2 contrast in MRI; a) correlation between T2 contrast during the magnetization phase and TE (time to echo event); b) graph of T1 contrast in which the magnetization is observed in function of TR (time of repetition); c) T1 and T2 intensity levels for common structure and their grey-scale equivalent in T1W and T2W MRI; d,e) Magnetic resonance of the occipital view of a brain. T2 map (d) and T1 map (e).*[30]

### 1.2.5 Summary

For each of these imaging modalities specific imaging agents for cell tracking with advantages and disadvantages have been developed. An overview of the main cell tracking CAs for each imaging modality is reported in Tab 1.1.

*Table 1.1: List of contrast agents available for direct cell labelling and cells succefully labeled with them.*

| | **CONTRAST AGENT** | **CELL TYPE** | **REFERENCES** |
|---|---|---|---|
| **BLI/FLI** | QDs | hMSCs | Rosen et al. 2007 [12] |
| | QDs | murine neural SC/progenitor cells | Stotkin et al. 2007 [12] |
| | NIR-QDs | murine DC | Noh et al. 2008 [8] |
| | NIR NPs | murine B cells | Thorek at al. 2010 [8] |
| | NIR dye | Murine NK | Daldrup-Link et al. 2011 [8] |
| **PAI** | Gold NPs | hMSCs | Nam et al. 2012 [12] |
| | Silica-coated gold NPs | hMSCs | Jokerst et al. 2014 [12] |
| | Silica-coated gold NPs | ADSc | Nam et al. 2015 [12] |
| **PET/SPECT** | $^{18}$F-SFB | Murine DC | Olasz et al. 2002 [8] |
| | $^{89}$Zr | Murine B-cells | Walther at al. 2011 [8] |
| | $^{11}$C | Murine NK | Melder et al. 1993 [8] |
| | $^{111}$In | Leukocytes | McAfee et al. 1984 [30] |
| | 18-FDG | Cardiac SCs | Collantes et al. 2017 [30] |
| **MRI** | SPIO | Murine macrophage | Gramoun et al. 2014 [8] |
| | SPIO | hMSCs | Hu et al. 2012 [12] |
| | IOPC-$NH^2$ | Murine T-cells | Daldrup-Link et al. 2011 [8] |
| | Gd-DTPA | Murine | Yang et al. 2014 [30] |
| | Fluorine-19 | macrophage/Murine NK | Bouchlaka et al. 2016 [30] |

Despite the wide applicability of each imaging technique it can be summarised the following:

- BLI, FLI and PAI have penetration limits that prevent their application for clinical purposes. They can be used to develop multimodal systems when coupled with other imaging modalities (MRI and PET).
- PET and SPECT cannot provide anatomical information, they need to be coupled with MRI or CT to have functional and anatomical details, moreover their limited spatial resolution and long radiative exposure times limit their use for cell tracking applications.
- MRI has the lowest sensibility among these imaging modalities, thus the use of sensitive CAs and optimized imaging sequence are mandatory for having a good response.

A summary of sensibility, tissue penetration, spatial resolution values and input signal is summarized in Tab 1.2.

*Table 1.2: System available for cell imaging with their key features.*

| Imaging modality | INPUT SIGNAL TYPE | TISSUE PENETRATION | SENSITIVITY (M) | SPATIAL RESOLUTION (MM) |
|---|---|---|---|---|
| **BL and FL imaging** | UV - NIR light | < 2 cm | $10^{-13}$ - $10^{-17}$ (BLI)<br>$10^{-9}$ - $10^{-12}$ (FLI) | 2-5 |
| **Photoacoustic imaging** | Light | < 6 cm | $10^{-9}$ - $10^{-11}$ | 0,005 – 1 |
| **PET/SPECT** | Radionuclide | unlimited | $10^{-10}$ - $10^{-12}$ | 1-2 (preclinical)<br>5-10 (clinical) |
| **MRI** | Radio frequency | unlimited | $10^{-3}$ - $10^{-5}$ | 0,1 (preclinical)<br>1 (clinical) |

Of note, the Center for Devices and Radiological Health of FDA in 2010 has recommended to reduce unnecessary radiation exposure from medical imaging [31], thus the use of radionuclides, necessary in PET and SPECT, should be avoided when a different method is available, in this case MRI is preferred in order to protect patient health.

## 1.3 MRI Contrast Agents

MRI contrast is based on the relaxation time of hydrogen protons differently present in various tissues with specific molecular composition and chemical environment that allows a high image contrast to define anatomical structures and identify pathological tissues. To further enhance MRI signal, contrast agents (CAs) based on metal atoms that can interact with the protons of the surrounding molecules, were initially developed to highlight the vascular system and successively have found a crucial use to enhance diseased from healthy tissues.

Besides the type of metal atom, CAs can be classified according to their magnetic properties, chemical composition, route of administration, biodistribution and applications.[32] Based on their relaxation effects on the surrounding water molecules, two family of CAs could be distinguished: T1, or positive agents, and T2, or negative agents. A recent class of CAs comprises the chemical exchange saturation transfer (CEST) effect, where the contrast agent protons directly exchange with the surrounding hydrogen atoms.

T1 contrast agents enhance the longitudinal relaxivity ($R_1 = 1/T1$) [33] by reducing the T1 relaxation time of water protons, which could be visualized as bright signal in T1-weighted (T1W) images. CAs belonging to this class are paramagnetic elements, mainly gadolinium and manganese ions. T2 contrast agents enhance the transversal relaxivity ($R_2 = 1/T2$) [32], with a magnetic dipole that locally alters the magnetic field and thus shorten the T2* relaxation time and diphases the magnetic moment of water protons which reduces the signal in T2-weighted (T2W) images. Such CAs are mainly superparamagnetic nanoparticles as iron oxide nanoparticles that are commonly called negative contrast agents.

CEST agents are a new class of MRI contrasts that can be classified according to their magnetic properties into: diamagnetic (DIACEST), or paramagnetic (PARACEST).[34], [35] PARACEST contrast agents, based on $Eu^{3+}$ and $Yb^{3+}$ chelates, have shown interesting

applications in brain imaging and recently for cell labelling thanks to the possibility to turn on or off the CEST signal produced by the CAs by modulating the RF pulse.[27]

As an example of positive and negative contrast agents in Fig. 1.3 is possible to observe the effects of both kind of CAs with their effects on $R_1$ and $R_2$, respectively. Rat glioma cells where labelled with manganese oxide (MnO) nanoparticles, T1 contrast agent, and iron oxide (FeO) nanoparticle, T2 contrast agent. The labelled cells were then transplanted into the brain of a rat and the MR images, $R_1$ and $R_2$ maps were collected.[33]

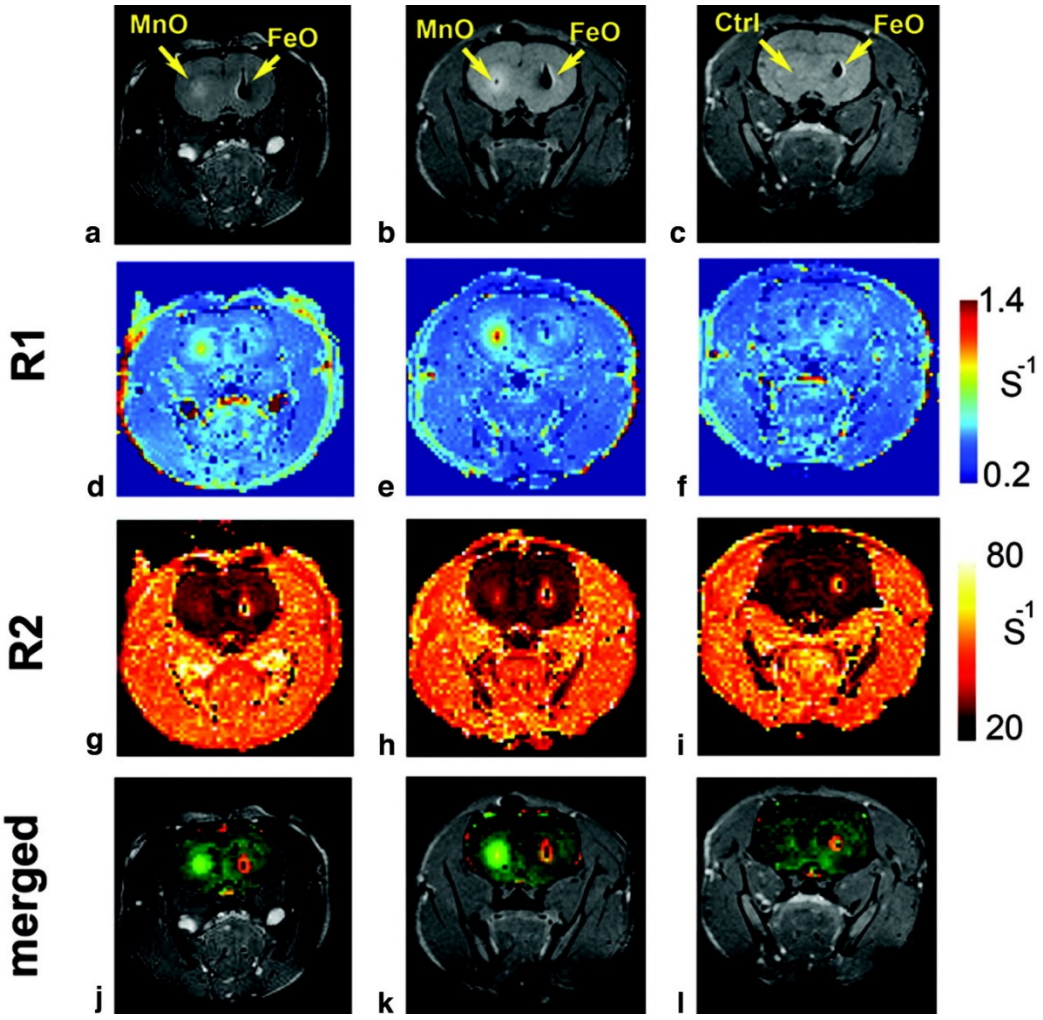


*Figure 1.3: Comparison between glioma cell labelled with MnO (T1 agent) and FeO (T2 agent) transplanted in a rat model. a-c) spin echo image, where the effects of both Cas on T1 and T2 are visible, d-f) R1 maps in which only the T1 effect of MnO is visible according to 1/T1 value, g-i) R2 maps in which is visible the effect of FeO according to 1/T2 value, j-l) merged maps (R1/R2) in which both labels are visible and tagged with different colours, green for MnO and red for FeO.*[33]

### 1.3.1 Gadolinium and Metal Chelates

Several transitional and lanthanide metals were used as MR CAs where the high magnetic momentum, due to high number of unpaired electrons, has effects on the relaxation times of the surrounding protons. Since 1984, the main developed CAs are based on dysprosium ($Dy^{3+}$), manganese ($Mn^{2+}$), iron ($Fe^{3+}$) [36] and gadolinium ($Gd^{3+}$).[37]

Gadolinium is a lanthanide metal with seven unpaired electrons and its ion ($Gd^{3+}$) presents a strong magnetic momentum able to significantly shorten the longitudinal (T1) relaxation time of water protons and also the transversal relaxation time (T2) at high concentration. Free $Gd^{3+}$ ions are toxic in unbound state and thus are chelated for in vivo applications. Different gadolinium complexes are commercially available: ionic compounds (Gd-DTPA and Gd-DOTA), characterized by a low toxicity and high osmolarity, and non-ionic compounds (Gd-DTPA-BMA and Gd-HP-DO3A), with a lower osmolarity and solubility. Several other formulations where developed for specific applications like blood pool agents for angiography or hepatobiliary agents to enhance liver tumours.[38]

Being based on relaxation time of surrounding protons, T1 contrast agents cannot be directly observed in MRI, in fact their effects are visible only by comparing the pre-contrasted image with an image acquired after the administration of the CA. In Fig. 1.4 MRI images obtained before and after the administration of Gd-DTPA, clearly shows the enhanced signal of the tumour in a patient indicating a highly permeable area compared to healthy tissues.

Since early 2000, nephrogenic systemic fibrosis (NSF) following certain gadolinium based contrast agents administration have been reported and a correlation was demonstrated in 2006 by Grobner.[39] More recently, Gd accumulation in the brain was reported and in 2017 the EMA and FDA restricted the use of linear gadolinium complexes.[40], [41] Although there are no evidences for toxicity of cyclic complexes, the administration of Gd based contrast agents was reduced in clinics. Consequently, alternative metal ions have gained interests in last decades, like manganese (II), iron (III) and copper (II).[37] Manganese, being involved in some biological activities, has been increasingly applied as contrast agent for brain structure and activity [42], hepatic lesions [37] and small metastases detection.[33]

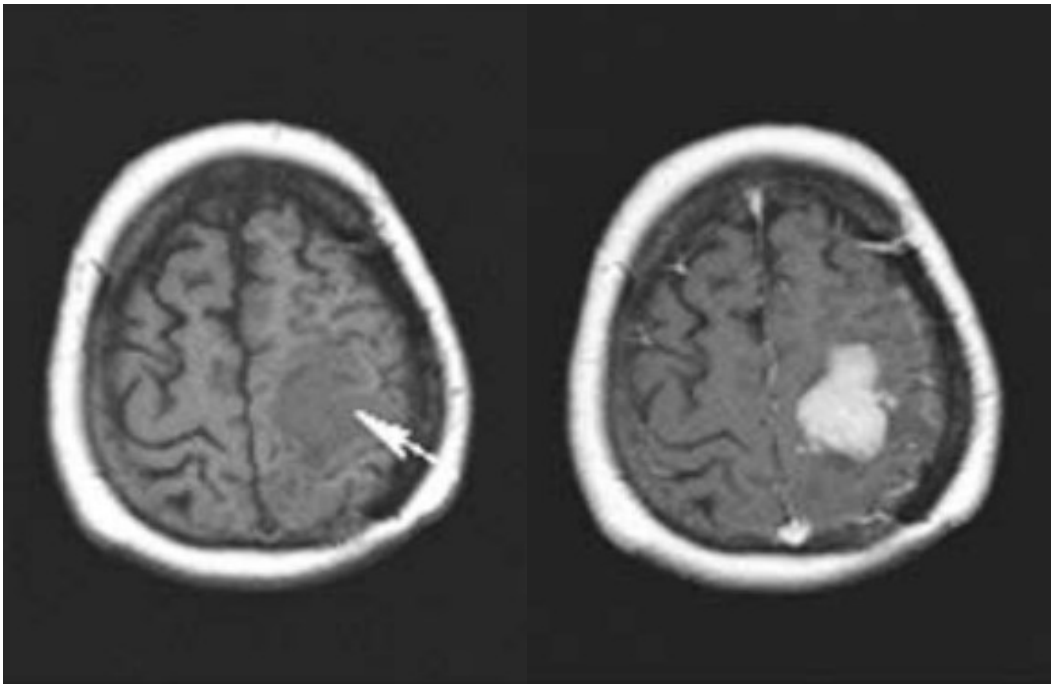

*Figure 1.4: MRI of a brain before (left) and after (right) the administration of a Gd-chelate (Gd-DTPA) contrast agents, the bright spot is where the CA is located and highlight the presence of a tumour in the patient.*[32]

Manganese ions can be administered in chelated form (Mn-DPDP) or in free state form ($MnCl_2$ solution). The free $Mn^{2+}$ ions application is mainly used to enhance cerebral structures and cellular activity since $Mn^{2+}$ is taken intracellularly through the calcium channels [37]. Its use is still limited to clinical studies, due to toxicity effects as it accumulates in cells as neurons and cardiomyocytes.[43], [44]

A more recent approach, aimed at reducing the dose-depending toxicity of heavy metals as CAs, saw their administration in the form of paramagnetic nanoparticles ($Gd_2O_3$, $GdPO_4$ and MnO). These nanoparticles demonstrated to provide comparable results to the those of conventional CAs (Gd-chelates or Mn-chelates) at a 10-fold lower concentration. The lower concentration, the better stability and clearance of these nanoparticles (excretion in 15 to 90 min) are the main advantages compared to common chelated products, which make them suitable to in vivo applications as contrast agents or for cell labelling.[27], [36], [45]

For cell labelling, Gd-chelates and Mn ions saw minor interest due to toxicity concerns and limited sensitivity at low concentrations. More recently, several development of Gd-

nanoparticles demonstrated an improvement in stability and sensitivity with the potential use of cell penetrating peptides suitable for cell labelling.[46], [47]

### 1.3.2 Iron Oxide Nanoparticles

Magnetic iron oxide nanoparticles are mainly composed of an iron oxide core (magnetite, maghemite or other ferrites) coated with an organic shell usually made of polymers, proteins or polysaccharides.[32] The iron core possesses a high magnetic momentum able to locally interact with the main magnetic field ($B_0$) and disturb spin-spin interactions among water protons by significantly reducing their T2 relaxation, which is observed as signal loss/reduction in T2W images (Fig. 1.5).[48], [45] When the diameter of the iron oxide core is lower than 50 nm these nanoparticles exhibit superparamagnetic behaviour showing strong magnetization and enhanced T2 relaxation.

Although determining the presence of SPION (Superparamagnetic iron oxide nanoparticles), a pre-contrast image must be acquired before they are administrated as the effects are not specific and could be confused with endogenous signals due to susceptibility artefacts (blood clots, vessels, necrosis, fat chemical shift) or to RF defects.

SPIONs present several advantages compared to other metal based NPs: i) high relaxation effects at low concentrations, ii) non-toxic at low dose, iii) easy surface modification of coating for nanoparticle functionalization and iv) possible tuning of the magnetic properties as a function of the NP size and addition of dopants (heavy metals added in the core to improve the magnetic properties of iron oxides).[36], [49]

Iron oxide based NPs can be classified according to their hydrodynamic diameter : i) micrometer (MPIOs) with diameters greater than 1µm, superparamagnetic iron oxide (SPIOs) with diameters of 50-300nm and ultra-small superparamagnetic iron oxide (USPIOs) for NPs under 50 nm.[45], [48] Indeed, as for most NPs, the biodistribution and blood half-life strongly depends on nanoparticles size. Moreover, by decreasing the size of particles of iron oxide, the longitudinal relaxation rate can be improved.[27]

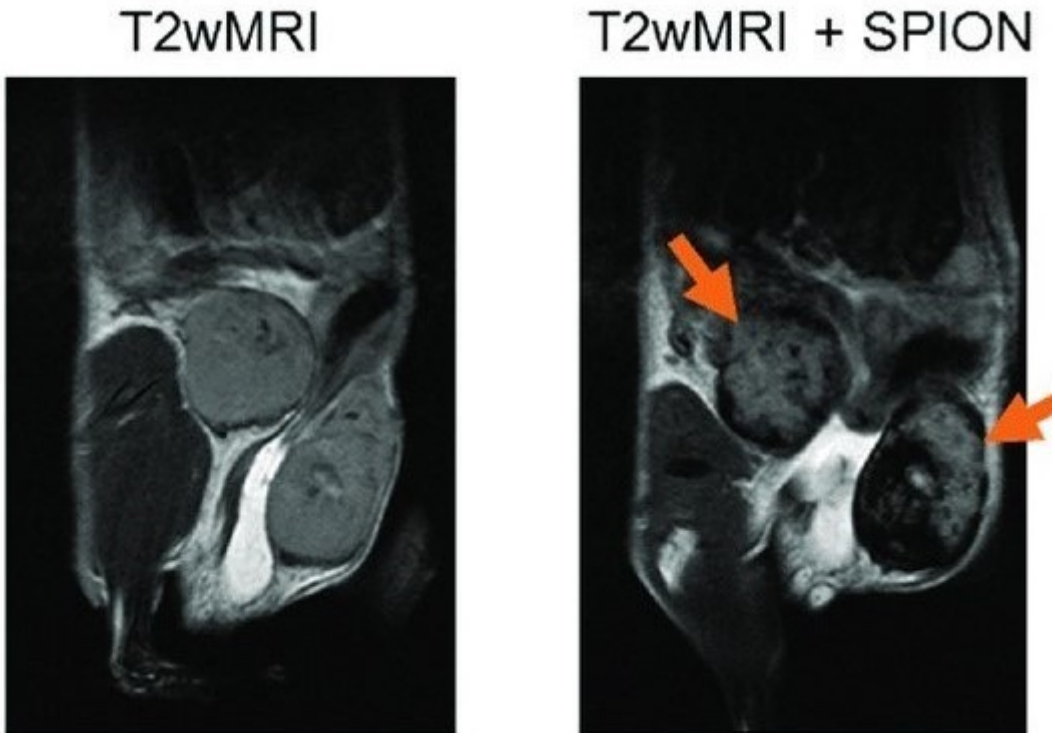


*Figure 1.5: Pre-contrasted (left) and post-contrasted (right) T2-weighted MRI on inflamed mouse mammary gland tumours. The darker areas due to the negative contrast of SPIOs that accumulated in the inflamed tissue are indicated with arrows.*[50]

Indeed, iron oxide particles were initially developed in 1986 as a T1 contrast agent and since then were used as alternative to GBCAs for clinical imaging of liver, spleen, bone marrow, tumour cells and as blood-pool agents for angiography.[36], [45] The application of SPIO NPs as contrast agents was firstly reported in 1995 [51] and declared safe for human application by FDA in 1996.[49] In the last two decades several SPIOs were approved for clinical applications and commercially available, but more recently many of them were removed from the market due to the insurgence of side effects after intravenous administration or due to failure in showing benefits compared to standard CAs.[52] Nevertheless, further developments are still ongoing for cell tracking.[51], [50]

As most nanoparticles, SPIOs are taken up by the cells of the reticuloendothelial system (RES) in particular macrophages, monocytes and Kupffer cells.[50], [9] Subsequently, SPIOs were largely developed for imaging inflammation and cell tracking. Several studies were reported using different types of SPIOs to label either stem cells [51] or different

immune cells.[53] Compared to other CAs, low amounts of SPIOs are detectable by MRI allowing the detection of small number of labelled cells. Dextran, polyethylene glycol (PEG) and other materials adopted for the coating are well known to enhance the uptake by phagocytic cells while the addition of transfection agents, like lipofectamine and protamine, [51] or membrane-translocating signal peptide [13], usually cross-linked to nanoparticles surface, are needed for stem cells and T cells.

Although SPIOs are easily visualized by MRI through the loss of signal due to magnetic-susceptibility, this negative contrast effect could be confounded with bleeds, blood vessels or air which makes SPIOs detection poorly specific and hardly detectable in heterogeneous organs.[45], [54]

With more than two decades of use, SPIOs toxicity is still not totally well established, different studies report divergent results. From i*n vitro* experiments, the toxicity effects of SPIOs are clearly reported with cellular stress, alterations in gene expression and proliferation, while other studies demonstrated that no effects were found even at high concentrations of nanoparticles. It has been demonstrated that these effects could depends on cell phenotype and particle formulations, however more studies need to be conducted to better investigate the potential toxicity of SPIOs.[51], [55]

### 1.3.3 Introduction to $^{19}$F-MRI

Beyond hydrogen, several nuclei like $^{13}$C, $^{23}$Na, $^{31}$P and $^{19}$F, can be detected by Magnetic Resonance with different levels of sensitivity.[56] Among those atoms, fluorine ($^{19}$F) has recently gained increased interest as the sensitivity is almost similar to that of the proton (83%) and is suitable to be used in cell tracking as the $^{19}$F signal is not present in the human body (except in teeth and bones) and thus it is proportional to the amount of $^{19}$F-nanoparticles and [57] directly imaged as shown in Fig. 1.6.

Moreover, the gyromagnetic ratio is close to the protons (40.08 MHz/T, 94.1% of $^{1}$H) allowing the acquisition of fluorine signal using almost similar radiofrequency coils on standard MRI scanners.[56], [58]

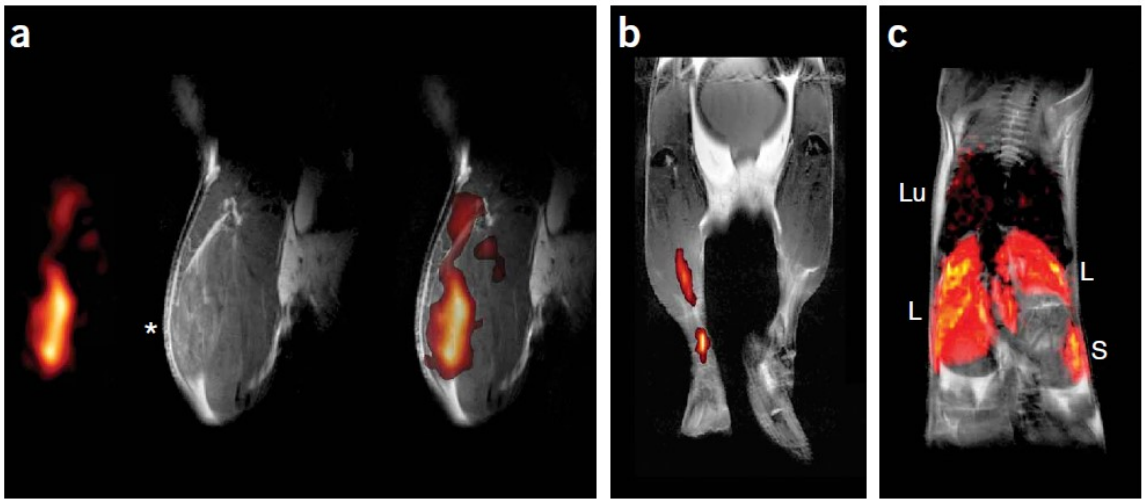


*Figure 1.6: Examples of $^{19}F$ MRI. Murine DC cells labelled with perfluoropolyether (PFPE) and injected a) intramuscularly into the quadriceps of a mice, from left to right: 19F-MRI, H-MRI and their composition $^{19}F/^{1}H$ images. b) $^{19}F/^{1}H$ composite image of DC cell migration after hind foot pad injection. c) composite image of accumulation of DC cells injected intravenously in liver (L), spleen (S) and lungs (Lu).*[59]

The first application of $^{19}F/^{1}H$ was proposed in 1970s by demonstrating the linear relationship between fluorine atoms and signal intensity. The main limitation of $^{19}F$-MRI is the large density of fluorine nuclei needed to obtain an image with a quality comparable with those obtained through $^{1}H$-MRI, considering that almost two-thirds of atoms presents in human body are hydrogen atoms.[60] To overcome this limit, highly fluorinated molecules, perfluorocarbons (PFCs), were adopted. PFCs are chemical compounds derived from hydrocarbons by replacement of hydrogen with fluorine. PFCs were firstly used in the biomedical field in early 1980s as inorganic blood substituents thanks to their ability to transport a large amount of oxygen to tissues.[61]

The physico-chemical properties of PFCs, due to the strength of C-F bond, grant them a high chemical, thermal and oxidative stability, but they are both hydrophobic and lipophobic, thus it is not trivial to formulate them in aqueous solutions. In biological environment they behave as bioinert compounds, they are not degraded at physiological pH and there are no enzymes able to cleave the C-F bond in the human body. The clearance of PFCs depends on the reticuloendothelial system (RES) and the excretion of C-F groups in lungs with respiration. However, due to their lipophobic and hydrophobic behaviours PFCs need to be incorporated

in delivery vectors, usually nanoparticles or emulsions, that enhance their water solubility and clearance profile.[56], [57]

For cell labelling, fluorine probes should fulfil the following characteristics:[56], [57]

- Biological inertness and chemical stability
- Stability in aqueous environment
- Low cytotoxicity and without effects on cell functions
- High density of fluorine atoms
- Simple synthesis and possible scalable formulation
- Simple $^{19}$F-NMR spectrum preferentially with one single peak to avoid artifacts and maximise the MRI signal
- Favourable relaxation times, with short T1 and long T2 for short MRI acquisition duration and maximise the MRI signal.

In Tab. 1.3 are shown the most used PFCs for cell labelling with their magnetic properties and applications.[62], [63]

Linear PFCs, like PFPE and PFOB, can be easily chemically modified to suit particular applications, but it is known that they resonate at multiple frequencies inducing artifacts, on other side symmetrical PFCE, with a single sharp peak, is difficult to modify without losing the symmetry of equivalent fluorine atoms and thus the generation of multi-peaks.

*Table 1.3: List of main PFCs used for cells labelling with major properties and primary applications reported in literature (PFPE: perfluoropolyether, PFOB: perfluorooctyl bromide, PFCE: perfluoro-15-crown-5-ether). The magnetic properties as chemical shifts and relaxation times are related to formulated compounds while for relaxation times is reported the intensity of the magnetic field with which the measures were performed.*

| PFC | $^{19}$F/ MOLECULE | $^{19}$F CHEMICAL SHIFTS (PPM) | RELAXATION TIMES (MS) | APPLICATIONS |
|---|---|---|---|---|
| PFPE | 28-36 | Main: -90.7; -90.9<br>minor: -58; -93 | T1: 423<br>T2: 155<br>[3T] | Primary T-cell[64]<br>Neural SCs[65]<br>hDCs[66]<br>Macrophages[67] |
| PFOB | 17 | Main: -81.82<br>minor: -63.7; -117.5; -122; -126.6 | T1: 1092<br>T2: 283<br>[3T] | SCs[68]<br>Progenitor SCs[68] |
| PFCE | 20 | -92.8 | T1: 1180<br>T2: 610<br>[7T] | hDCs[62]<br>Macrophages[69]<br>Murine microglia[70] |

### 1.3.4 PERFECTA

Recently, as alternative to these compounds, it was proposed another PFC, named suPERFluorinatEdContrasT Agent (PERFECTA), suitable for cell labelling and tracking). PERFECTA is a branched and highly fluorinated (36 fluorine atoms/molecule) compound developed to fulfil all the requirements shown before, in particular it is characterized by a single sharp peak, due to its symmetrical structure, and can be easily functionalized with minor effects on the $^{19}$F-NMR spectrum. PERFECTA can be easily produced through a single step Mitsubono reaction between pentaerythritol and perfluoro-t-butanol in good yield.

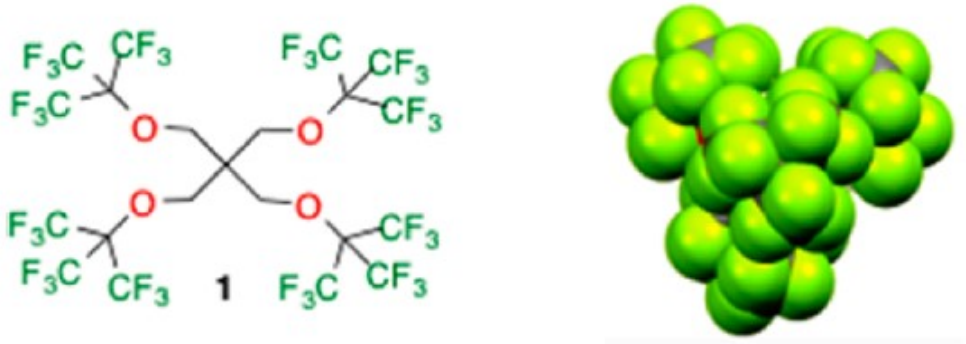


*Figure 1.7: PERFECTA structure and single crystal X-ray structure.*[71]

Differently to others PFCs that are liquids, PERFECTA appears as a crystalline white powder, insoluble in water and common organic solvents. To be active in $^{19}$F-NMR it needs to be formulated with stabilizers such as lecithin and safflower oil [71], Pluronic [70] or PLGA [72] in aqueous solutions. Nanoformulations of PERFECTA are stable in the aqueous environment and show a single and sharp peak around -73.4 and -73.5 ppm (depending on formulation), while the relaxation times are favourable to acquisition using fast sequences (T1: 690 ms and T2: 202 ms at 7T and 20 °C).[70], [71]

The shelf-life of these nanoformulations was assessed to be at least 6 weeks at room temperature, except for PLGA based ones due to the biodegradability of the polymer. Previous works demonstrated the biocompatibility of the lecithin emulsions *in vitro* in hamster fibroblast (BHK-21) and Lewis rat bone-marrow derived DCs with no evidence of toxicity of functional impairment even at high dose (9.92 mM) of the fluorinated emulsion.[71] Similarly, Pluronic coated NPs of PERFECTA did not show any acute toxicity *in vitro* using murine microglial cell lines (BV-2) and also *in vivo* in murine models (C57BL/6).[70] In both cases it was observed that a sufficient cellular uptake of PERFECTA to be imaged by 19F-MRI occurred with incubation times in the range of 4 to 8 hours, labelling was still visible 48h after injection [71] and even 11 days after in *in vivo* study.[70]

Recently, it was investigated the feasibility to administer two different PFCs (PERFECTA and PFCE) to have a “two colours” contrast, this was possible thanks to the sharpness of both 19F-NMR peaks and their distinct chemical shift. Thanks to these features it was possible to observe simultaneously the inflammation process and the fate of labelled cells

[70] and to study both degradation and biodistribution for drug delivery applications in vitro.[72]

## 1.4 FLUORINATED NANOFORMULATION

PFCs, due to their hydrophobicity, need to be formulated into emulsions to be viable in physiological conditions, where hydrophilic or lipophilic emulsifiers stabilize the formulation segregating PFCs droplets from the aqueous solution. Liquids PFCs appear as dense oil by themselves, and in aqueous environment tend to form a separated phase from water. These emulsions were initially developed as blood substitutes, where phospholipids or poloxamers were added as emulsifiers, due to their ability to load high amount of PFCs forming quite stable emulsions. Emulsions are simpler, kinetically stable biphasic systems usually composed of a PFC core and a surfactant coating [73], while more sophisticated systems was lately proposed in which the PFC core was hidden in polymeric NPs stabilized with a surfactant.[74] Alternatives to emulsions, other systems based on dispersions of fluorinated peptides/polymers and fluorinated sugars were early investigated due to their specificity to study aspect of the cellular functionality [68], but the chemical alteration in their structure, caused by high electronegativity of fluorine atoms, the loss of bio inertness behaviour and the lower payload of 19F/molecule make their applications as cell labels more difficult respect nanoemulsions and nanoparticles.

These systems need to fit several design criteria to be efficiently used for cell labelling and in vivo tracking by $^{19}$F-MRI:[75]

- Small droplet size
- Polydispersity index (PDI) <0.2
- High fluorine/surfactant or fluorine/polymer ratio
- Surface able to promote cell membrane interaction
- Long-term intracellular retention
- Biocompatibility


*Figure 1.8: Fluorinated emulsion and nanoparticles schemes.*[68] *Emulsion are characterized by fluorinated compounds dispersed in a solvent and entrapped inside a lipidic or polymeric shell. Particles are more complex systems in which the PFC is dissolved with a solvent and confined with a polymeric coating stabilized with surfactants.*

The main controversial criterion is represented by the definition of droplet size because usually are intended a mean size lower than 200 nm but several studies reports that optimal nanoparticles size depends on cell adopted.[73], [76]

### 1.4.1 Lipidic and Polymeric Nanoformulations

The most conventional nanoformulations are composed of a perfluorocarbon core stabilized by a lipidic or polymeric shell. These emulsions were developed initially as contrast agents in ultrasonography due to echogenic properties of PFC.[77] Lately, these formulations were studied to develop a dual contrast agent with gadolinium chelates for detection, quantification and *in vivo* targeting of atherosclerosis lesions. These systems were composed of a PFC emulsion stabilized by lipidic surfactant with Gd-chelates conjugated on the droplets surface, in which the role of the emulsion is to concentrate the Gd ions onto their surface and to present functionalized groups able to selective bind determined target for specific applications.

Due to fluorine properties and thanks to the results obtained in dual contrast systems the application of PFC emulsions as positive contrasts for detection of inflammation has taken place also for cell labelling. In 2005 Ahrens published the first work in which a PFPE

emulsion, stabilized by lecithin and safflower oil, was used to label dendritic cells and subsequently was tested on murine models for in vivo tracking.[59] Lecithin and safflower oil are the main components of PFC emulsions due to their improved stability and reduced degradation via Ostwald ripening, that is the main problem for PFC emulsions. Ostwald ripening is the main cause of instability for these formulations and lead to the degradation of the emulsion and to phase separation between oil and water, the effect is driven by a gradually increase of larger droplets resulting in a difference in chemical potential with respect to the smaller ones destabilizing the colloidal suspension.[78]

Alternative to lipidic emulsifiers can be found in poloxamers, non-ionic block-copolymers formed by poly(ethylene oxide) and poly(propylene oxide) (PEO-PPE-PEO). These copolymers are amphiphilic compounds that expose the hydrophobic domain to PFC and the hydrophilic regions to water interface. Non-ionic surfactants were re-proposed with the aim to reduce the Ostwald ripening effect, in fact adsorbed polymers are more robust than lipidic coating and slow down the aggregation of droplets that lead to emulsion instabilities [79], this behaviour is principally related to their steric interactions that stabilize the emulsion preventing also flocculation. The improved stability of these nanoformulations is indicated by a lower PDI, index of a better homogeneity in the formulation. Indeed, for example PFPE emulsions stabilized with Pluronic F68 and a linear short chain of polyethyleneimine (PEI) has demonstrated narrow sizes and colloidal stability for 4 months and no signs of Ostwald ripening for 14 months.[75], [80]

Overall, nanoformulations developed for $^{19}$F-MRI cell tracking are composed of PFCs providing the MR information and surfactants/polymers needed to stabilize the emulsion in the aqueous environment to provide interface properties for the interaction between cell membrane and emulsions. Moreover, the emulsifier provides a binding site for other compounds, as fluorescent dye or Gd-chelates, permitting the development of bimodal systems.

The main problem related to these nanoformulations is their relatively low colloidal stability often related to oxidation and hydrolysis problems for the lipidic emulsifiers and to the formation of highly viscous emulsion for poloxamers.[74]

Although the best results in terms of stability can be reached with fluorinated surfactants that give lower interfacial tension between perfluorocarbon and water. Unfortunately, these

surfactants are quite toxic to be used in biomedical applications and could introduce artifacts in $^{19}F$ MRI, this is why they have not been investigated.[75], [78]

### 1.4.2 PLGA-based Nanoformulations

Polymeric nanoparticles approach for the development of fluorinated nanosystems is relatively new and is inspired by the rapid increased trend in the application of biodegradable poly(lactic-co-glycolic acid) (PLGA) NPs as drug delivery systems and tissue engineering scaffolds.[81] The suitability of these polymers to develop NPs for cell tracking was studied with the specific aim to develop multifunctional devices for theragnostic applications starting from devices for drug delivery and adding to them something through which it was possible to observe the fate of these devices after their administration.[81], [82]

New PLGA-based formulations for stabilizing PFCs in water comprise the three following materials: i) the polymer coating (PLGA), that grants stability and functionalization site, ii) the surfactant, that works as co-stabilizer and according to the used surfactant can provide specific characteristic to the surface, i.e. charge, and iii) PFC, that possesses the magnetic properties of interest. PLGA formulations have their key advantage in a modular structure that enable suitability to experimental setup. This modularity in their composition permits to obtain different type of formulations, due to the possibility to use different compounds (i.e. a different surfactant or PFC) or include something new (i.e. a dye), without great modification to the protocol.[83] These emulsions immediately showed the ability to encapsulate and stabilize high amount of PFC.[74]

PLGA is an amphiphilic copolymer composed by polylactic acid (PLA) and polyglycolic acid (PGA). PLA is a hydrophobic polymer with a long degradation time while PGA is rapidly degraded in physiological environment due to its high hydrophilicity, the overall properties of PLGA depends on the ratio of the two polymers and on the molecular weight (Mw). Increasing the PLA/PGA ratio in favour of PLA increase the hydrophobic behaviour and consequently the degradation occurs slowly, the same effect on degradation mechanism can be observed for PLGA with higher Mw (confronted at same PLA/PGA ratio).[84] The possibility to control the degradation time, on which depends the release rate of the

encapsulated compound, working on these two parameters is what made PLGA appetible to biomedical applications. A recent study, aimed to investigate the clearance of fluorinated PLGA nanoparticles, shows that the $^{19}F$ signal associated to NPs decay more rapidly respect the one related to a lipidic emulsion demonstrating a faster clearance for the NPs in which the disassembly into a smaller domains helps in their depletion from the host system as represented in Fig. 1.9.[85]

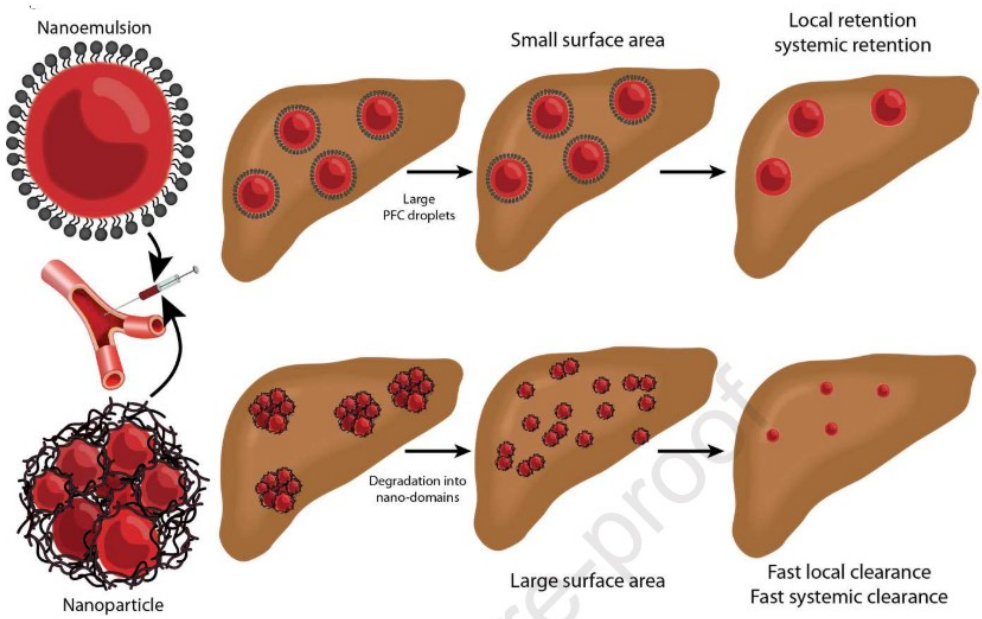


*Figure 1.9: Representation of the degradation of fluorinated emulsion (upper raw) and fluorinated NPs (lower raw)in the liver. Is possible to observe the disassembly of the NPs into smaller domains easily cleared by the liver respect to the bigger PFC core of the emulsions.*[85]

Moreover, the carboxylic acid termination of PLGA can be easily functionalized with a plentiful of moieties able to provide specific characteristic to the final device. Particular interest can be found in conjugation with fluorescent dye, for the development of bimodal probe for imaging, with polyethylene glycol (PEG), to enhance the blood half-life, or with cell-penetrating peptides or specific ligands, to improve cellular recognition and uptake.

The choice of the right surfactant should be accurately evaluated because there are several compounds available as stabilizers and each of them provides specific properties to the final

formulation, moreover several studies stated that also the concentration of these compounds can dramatically affect the final results. The choice of the surfactant is probably one of the most crucial steps in the development of a formulation for biological applications because on it will depend the surface charge, contributing to cellular uptake and colloidal stability, the formulation fate and "stealth" properties, influencing the blood half-life, and also, for this particular case, the PFC encapsulation. Among all commercially available surfactants the most used for PFC-PLGA NPs are: polyvinyl alcohol (PVA), polysorbate (Tween 20 or 80) sodium cholate, poloxamers (as Pluronic F68) and polyvinyl pyrrolidone (PVP).[74], [86] These surfactants are all FDA approved and enhance the colloidal stability of PLGA NPs through steric or electrostatic interactions, they are amphiphilic (Pluronic F68), zwitterionic (PVA) or negative charged compounds (sodium cholate) that can enhance or shield the negative charge of PLGA in the physiological environment, although often the resulting formulations still maintain a net negative charge needed to communicate with cell membrane proteins and being phagocyted.

In conclusion, PFC-PLGA nanoformulations are obtained as oil-in-water emulsions with the help of sonication or microfluidizers to provide the needed energy to encapsulate the PFC. Further functionalization can be provided either by addition of specific compounds adsorbing on the NP surface or through chemical linking of functional group to PLGA backbone before the preparation of the NP dispersion.

Despite these nanoformulations have shown promising results in terms of high value of $^{19}F$ encapsulation, these results are still too low for clinical MRI scanners sensibility and major improvement is required for clinical use. Formulation optimizations are necessary to overcome MRI sensibility limits and cellular uptake, starting from these needs we chose to encapsulate a highly fluorinated compound as PERFECTA into PLGA nanoparticles to develop fluorinated probes for cells tracking by $^{19}F$ MRI.

In particular in this thesis work will be presented the development of different PERFECTA loaded PLGA NP dispersions and their optimization for $^{19}F$-MRI cell tracking. The stability and $^{19}F$ content of the probes obtained will be studied and, at the end, their cytocompatibility and uptake will be investigated *in vitro* by $^{19}F$-MRI to explore their overall performance looking for a candidate suitable for therapeutic cells applications.

# 2 EXPERIMENTAL PART

## 2.1 GENERAL OVERVIEW

The main aim of the present master thesis was the development of new fluorinated probes and in their application for cell tracking by $^{19}F$ MRI. These probes are based on the perfluorocarbon PERFECTA, which is encapsulated in a PLGA NP stabilized by a surfactant. Different nanoformulations were developed and characterized using differently functionalized PLGA and different surfactants. These formulations were lately used to label murine microglial cells and their uptake was investigated through $^{19}F$-MRI and $^{19}F$-MRS.

The physical and chemical properties of these probes were initially characterized before testing on cells. Fourier-transform infrared (FT-IR) spectroscopy was employed to investigate the presence of PERFECTA inside the probes while quantitative $^{19}F$ nuclear magnetic resonance spectroscopy ($^{19}F$-NMR) was used to quantify the amount of $^{19}F$ inside the nanoformulations. Dynamic Light Scattering (DLS) and Nanoparticle Tracking Analysis (NTA) were used to investigate the physical properties of nanoparticles as hydrodynamic diameter, polydispersity index (PDI) and NP concentrations. Zeta Potential was also measured to investigate the superficial charge and verify the colloidal stability of nanoparticles.

Colloidal stability depends mainly on polymer and surfactant properties, it could be reached through steric or electrostatic interaction that prevent the aggregation of nanoparticles. For this work two different surfactants were investigated, polyvinyl alcohol (PVA) and sodium cholate (DS-Na), that stabilize the system respectively via steric and electrostatic interactions. DLS and zeta-potential analysis were performed to verify the stability of the NPs in solution since these parameters strongly influence NP-cell interactions in terms of uptake, targeting and trafficking.[87], [88] $^{19}F$-NMR with external references were performed to determinate the total number of $^{19}F$ atoms, as [$^{19}F$] should be in the $10^{-3}$-$10^{-5}$ M range to be detectable through MRI.

An immortalized murine microglial cell-line (BV-2) was used as it is a stable model of phagocytic cells which do not require the use of animals to obtain cells. Cytotoxicity was

investigated through Trypan blue exclusion method and NP cellular uptake was verified on a preclinical 7T magnetic resonance imaging (7T-MRI) scanner at IRCCS San Raffaele (MI). Light field microscopy was used to confirm the internalization of NPs by the cells.

## 2.2 MATERIALS

For the NP formulation the following reagents were used: poly(lactic-co-glycolic acid) (PLGA) Resomer 502H (50:50, 7000 - 17000 Da, acid terminated, Sigma Aldrich, Germany) and Resomer 504 (50:50, 38000 - 54000 Da, ester terminated, Sigma Aldrich, Germany), polyvinyl alcohol (PVA, 30000 - 70000 Da, 87-90% hydrolysed, Sigma Aldrich, Germany), sodium cholate (DS-Na, Sigma Aldrich, Germany), PERFECTA was synthesized at the SupraBioNanoLab (SBNLab) at Politecnico di Milano according to protocol published by Ilaria Tirotta *et al.* [71], ethyl acetate (EtOAc, purity ≥ 99.5%, Sigma Aldrich, Germany), water ultrapure Type-I Milli-Q water (mQw) (18.2mΩ/cm) provided by a Simplicity® water purification system.

For in vitro experiments the following reagents were used: immortalized murine microglial cell-line (BV-2) (kindly provided by Dr. R. Furlan's lab, San Raffaele Hospital, Milano), Dulbecco's modified Eagle's medium (DMEM; Lonza) was used as culture medium supplemented with 10% fetal bovine serum (FBS), 100 mg/ml of streptomycin, 100 U/ml of penicillin and 2 mM of L-glutamine (Gibco-Invitrogen). Trypan blue (0.4% solution, Sigma Aldrich, Germany) was used for cytotoxicity assays. 4% paraformaldehyde (PFA) was used to fix cells before MRI analysis.

For NPs characterization analysis the following reagents were used: phosphate buffered saline (PBS), sodium chloride solution (NaCl, 10 mM), trifluoroacetic acid (TFA, purity ≥ 99.9%, Sigma Aldrich, Germany), deuterium oxide ($D_2O$, Sigma Aldrich, Germany).

## 2.3 METHODS

### 2.3.1 Nanoparticles Formulation

The protocol to prepare the proposed NP formulations is based on the emulsification of an organic solution containing PLGA and PERFECTA in an aqueous phase, in which the surfactant is dissolved. Hydrophobic compounds as PERFECTA requires an organic solvent to be dissolved, ethyl acetate (EtOAc) was chosen as it was the only solvent able to dissolve PERFECTA. PLGA is also dissolved in EtOAc while both surfactants used (PVA and DS-Na) are soluble in mQw. After the dissolution of each compound in a suitable solvent, the two organic solution are mixed in order to obtain a single organic phase, this last is added to the aqueous phase and sonicated with a tip sonicator obtaining an oil in water (o/w) emulsion, in which PERFECTA is entrapped in the core of the PLGA NP stabilized by a surfactant shell that enhances the system stability due to steric or electrostatic interactions among different NPs. The organic solvent (EtOAc) is subsequently removed by evaporation with the help of a desiccator. The resulting solution was centrifuged and washed and then resuspended into mQw for further analysis and cell labelling.

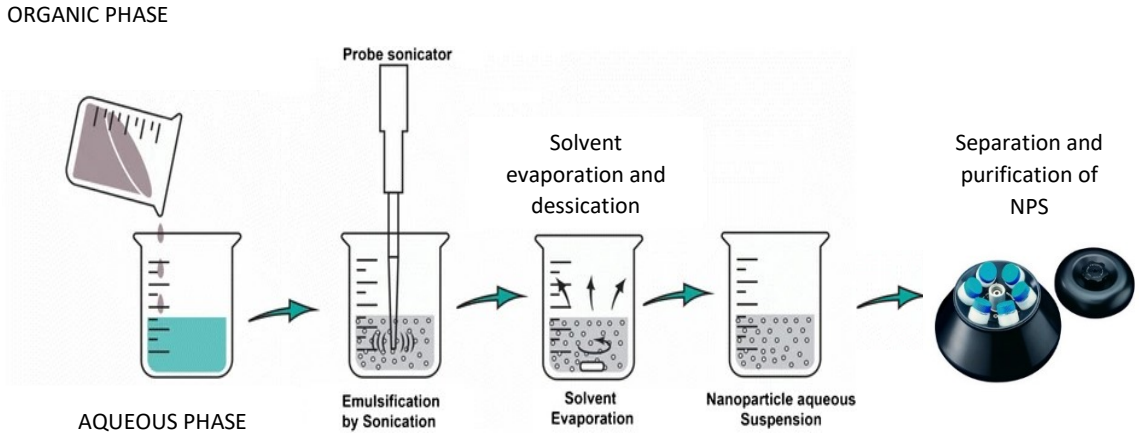


*Figure 2.1: Schematic representation of the followed procedure for the preparation of the formulation. The oil-in-water emulsion is made mixing the aqueous phase, containing the surfactant, with the organic phase, in which PLGA and PERFECTA are dissolved. The tip sonication provides the energy needed to form the NPs, while the excess of organic solvent is let to evaporate during stirring. NPs are finally collected as pellet after centrifugation and then resuspended.*

In Figure 2.1 is represented a scheme of the formulation procedure, however all formulation protocols will be shown in Fig. 2.1.

An aliquot of each nanoformulation was taken for characterization, while the amount designed to *in vitro* experiment was sterilized with UV light for 30 min.

### 2.3.2 Dynamic Light Scattering (DLS)

Dynamic Light Scattering (DLS), known also as Photon Correlation Spectroscopy (PCS), is a technique that gives information about the dimension and the polydispersity of colloidal particles inside a solution. The motion of the particles in a solution is based on the Brownian motion theory, observed firstly in 1827 by Robert Brown and theorized in 1905 by Albert Einstein, for which the dispersed materials in a solution are subject of random motions caused by collisions with solvent molecules, these movements depends on the particle size and temperature and viscosity of the solvent. The energy exchanged during the collision is almost constant, while the diffusion is related to the hydrodynamic diameter ($D_H$) according to *Stokes-Einstein equation*:

$$D_0 = \frac{K_B T}{6\pi\eta\, R_H} \quad (1)$$

Where $\eta$ is the viscosity of the solvent, $K_B$ is the Boltzmann constant, $D_0$ is the diffusion coefficient and $R_H$ is the hydrodynamic radius.[89], [90] Knowing all the parameters the dimension of the particles can be easily calculated. DLS instruments are used to easily obtain diffusion coefficient of particles in the nanometer-micrometer ranges in a solution.

In DLS analysis a monochromatic light beam (laser) goes through a liquid sample and if there are any particles dispersed in the solvent the incident light is scattered in all the directions and it is recorded by a detector. The scattering can be divided into anisotropic Mie Scattering, when the scattered light energy is unequal to the incident light energy due to inelasticity in the scattering leading to angle dependency, this occur when the particles are bigger than one tenth of the incident light wavelength, and isotropic Rayleigh Scattering, in which the energy is maintained between incident and scattered light resulting in independency from angle, this is observed for particles smaller than one tenth of the incident

light wavelength.[89], [91] Moreover, due to the random fluctuations of the particles in the solution, the interference caused by them can be constructive, resulting in a detectable signal, or destructive, with no signal detection, these fluctuations depends on nanoparticles radius and have effects on the intensity of the scattered light. At the end, the scattered light hits the detector and all these signals are correlated by a digital autocorrelator that calculates the integral of the correlation function at time 0 and after a delay from which the diffusion coefficient could be obtained.

More in detail, DLS measures the normalized time correlation function, $g_2(\tau)$, of the scattered light intensity (I):

$$g_2(\tau) = \frac{|I(0) + I(\tau)|}{|I(0)^2|} \quad (2)$$

Where $\tau$ is the correlation delay time. The same can also be expressed also in terms of the correlation function, $g_2(\tau)$, of the scattered light field through *Siegert relation*:

$$g_2(\tau) = 1 + \beta[g_1(\tau)]^2 \quad (3)$$

Where $\beta$ is the coherence factor, a parameter characteristic of the instrument. In the case of equal-sized particles, $g_1(\tau)$ can be expressed as a mono-exponential function:

$$g_1(\tau) = exp(-\Gamma * \tau) \quad (4)$$

Where $\Gamma$ is the decay rate defined as $\Gamma = D_0 * q^2$, in which $q$ is the scattering vector and depends on the scattering angle $\theta$ through the following relation:

$$q = \frac{4\pi n}{\lambda} * sin\left(\frac{\theta}{2}\right) \quad (5)$$

From these equations related to the theory behind DLS technique, the particles size is determined. Nonetheless, when the sample is polydisperse and each particle has its own exponential decay the correlation function results in a more complex expression as:

$$g_1(\tau) = \int G(\Gamma) + exp(-\Gamma * \tau) d\Gamma \quad (6)$$

Where $G(\Gamma)$ is the normalized distribution of the decay rates. Thus, $g_1(\tau)$ resembles the Laplace transform of $G(\Gamma)$, which can be obtained by inverse transformation. This operation is not simple, and several techniques have been implemented to achieve it, like exponential

sampling, regularization, maximum entropy, maximum likelihood and non-negatively constrained least squares.[90], [91]

In our work, data analysis was performed according to standard procedures that use Laplace inversion of the time auto-correlation functions was obtained through a non-cumulant method using CONTIN algorithm. Multiangle DLS was measured with the ALV compact goniometer system, equipped with ALV-5000/EPP Correlator, special optical fiber detector and ALV/GCS-3 Compact goniometer, with He-Ne laser ($\lambda = 633$ nm, 22 mW output power) as light source. The temperature was controlled with a thermostatic bath and set at 25° C. A volume of 1 ml of formulation 1:100 v/v was used for the analysis and stored at + 4° C between subsequent analysis. Nanoformulations stability were analysed through DLS measurements performed at different time points (0, 24 h, 48 h, 5 days and 1 week) and scattering angles (θ) of 70°, 90°, 110° and 130°. Each measure was the result of the average of three subsequent runs of 10 seconds each, with a threshold sensibility of 5%. Data analysis was done with ALV-Correlator software with automatic and manual modality. The decay rates $\Gamma$ at each detection angle were plotted as a function of the square of the scattering vector $q$ and they were all fitted on a line. From the slope of this line the diffusion coefficient $D_0$ was retrieved. Using the value of $D_0$ in Stokes-Einstein relation, the average hydrodynamic radius ($R_H$) was estimated.

### 2.3.3 Nanoparticle Tracking Analysis (NTA)

Nanoparticles Tracking Analysis (NTA) exploits the properties of both light scattering and Brownian motion to obtain the particle size distributions of samples in liquid environment. Differently from DLS systems, the NTA systems (Fig. 2.2) have a charge-coupled device (CCD) camera able to visualize and record the particles in the solution. Indeed, the laser beam that is refracted when the interface between the glass and the sample is reached resulting in a reduction of the beam profile and in an increment in the power density, due to a calibration of the angle of incidence of the laser and the refractive index of the glass. Particles in the suspension scatter the light in a manner that permits their visualization via long working distance, 20x magnification microscope objective that record the field of view for the analysis.[92], [93]

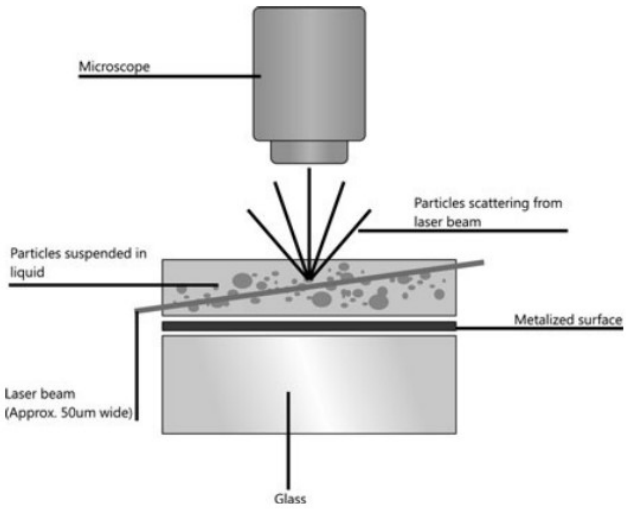


*Figure 2.2: Schematic representation of the optical configuration used by NTA systems.*[92] *The microscope on which the camera is mounted taken up the light scattered by NPs when it is illuminated by the light source.*

NTA software records a 30 s to 60 s video of the light scattered by particles moving under Brownian motion and simultaneously identifies and tracks the centre of each particle and determines the average distance travelled by each particles in the x and y directions. From these information the software initially determines the diffusion coefficient, according to the *Stokes-Einstein equation*, and from this the hydrodynamic diameter.[92], [93]

NTA systems provides more accurate results with respect to the DLS system because the measurement is based on the tracking of single particles and so it is not biased toward the detection of larger particles.[93]

NTA measurements were performed with a NanoSight NS300 (NanoSight, Amesbury, United Kingdom) equipped with a green laser ($\lambda$ = 532 nm) and a sCMOS camera. Samples were prepared in a dilution range between 1:1000 and 1:10000 V/V in MilliQ, based on the formulation, they were loaded in the sample chamber with a sterile syringe until the liquid fits the discharge tube at the end of the glass camera, on which the sCMOS camera is mounted. Then the syringe was mounted on a peristaltic pump set at 100µl/min that pumps the liquid while the analysis is running. Each sample has been recorded for 60 s video for three times at room temperature (25°C). These analyses were done at the SCITEC institute (MI) of Consiglio Nazionale delle Ricerche (CNR).

### 2.3.4 Zeta Potential

Zeta potential ζ (ZP), also called electrokinetic potential, is the electrostatic potential measured in correspondence of the slipping plane of a colloidal particle dispersed in motion inside a liquid under the effect of an electric field. The measure of the zeta potential is a useful tool for the determination of the colloidal suspension stability. In case of rigid charged particles was observed that an electronic double layer (EDL) is formed on its surface, this adsorbed double layer is composed by the *Stern*, or inner, layer constituted by ions with opposite charge (*counter ions*) with respect to the charge of the particle, while the outer, or *Gouy-Chapman*, layer is made of a diffuse layer in which both, positive and negative, ions and molecules are present (Fig 2.3). This lead to a "fixed" layer, contiguous to the nanoparticle, in which the ions move within the particle, and a "mobile" layer, defined diffusive layer of the EDL, in which the ions and molecules are free to diffuse when they are less affected by charged particles.[89], [94] The electrostatic interaction between the particle surface and an ion/molecule decreases with the distance according to the *Debye's law*:

$$\psi = \psi_d e^{-kx} \quad (7)$$

Where $\psi$ is the surface potential at distance x from the *Stern layer*, $\psi_d$ is the surface potential at the *Stern layer, k* is the Debye-Hückel parameter and x is the distance.

Zeta potential is the electrostatic potential present at the slipping/shear plane, that is a hypothetical plane, in the diffusive layer, that acts as the interface between the moving particles and the layer of the dispersant around it. However, due to the impossibility to directly determine the particle charge, known as *Nernst potential*, the charge of the NP is measured indirectly through the analysis of the Zeta potential based on the measurement of the electrophoretic mobility, defined by *Henry's equation* as:

$$\mu_e = \frac{2\varepsilon\zeta F(ka)}{3\eta} \quad (8)$$

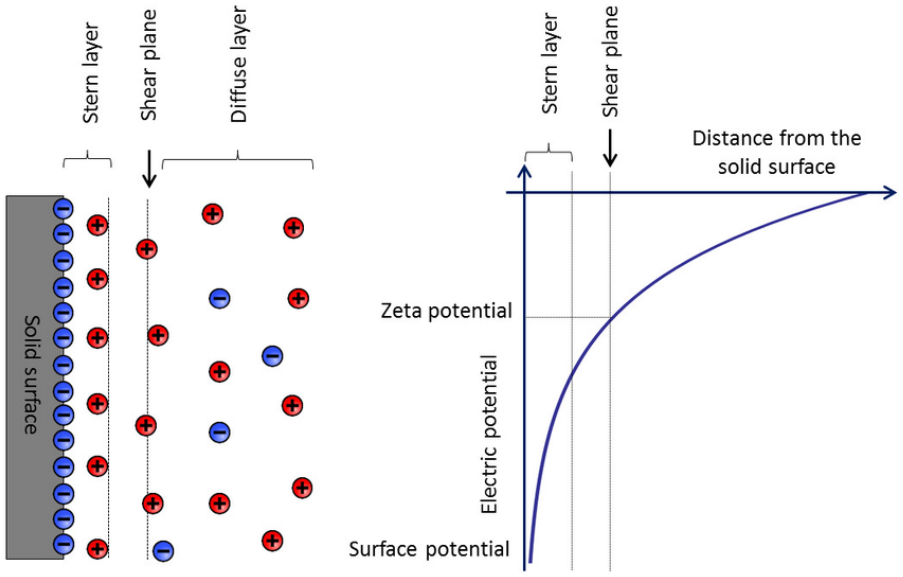


*Figure 2.3 Representation of the electric double layer on a negatively charged surface and electrostatic potential function in function of the distance with emphasis on Stern layer and slipping (shear) plane.*[94]

Where $\varepsilon$ is the solvent dielectric permittivity, $\eta$ is the viscosity at room temperature of the solvent and F(ka) is the Henry's function. F(ka) varies between 1 and 3/2 according to the ratio l/k (particle size to the Debye length). Henry's function can be assumed equal to 1 (Hückel approximation) when dealing with not aqueous suspension and small radius of particles. In pharmaceutical preparations, a value of F(ka) equal to 1.5 is generally taken, assuming an ionic media and a small EDL with respect to the particle radius (Rh < 1 $\mu m$). We have to consider that Zeta potential is sensitive to:

- pH: zeta potential is more positive in acidic pH and more negative in basic ones due to protonation and deprotonation of the external functional group of the particle,
- Stern potential: the value of $\psi_d$ can exchange due to surface chemistry, pH and on the presence of adsorbed molecule such as surfactants and impurities
- Ionic strength: EDL becomes more compressed with increasing the ionic strength while the zeta potential decreases.

As initially stated, zeta potential measures can be used to determine the stability of colloidal suspension based on electrostatic repulsion between the particles preventing their aggregation and sedimentation/flocculation. According to literature, it is defined unstable, a

system for which the ζ-potential is between 0 and ± 10 mV, in the range ± 10 mV and ± 30 mV the system is considered moderately stable, while a net charge greater than ± 30 mV is needed by the system to be completely stable. Nonetheless, these stability considerations take in account only the Columbian repulsive interactions among the particles and not the attractive Van der Waals forces and steric interactions, therefore some dispersions are stable despite a low ZP value.

In the present work, ZP was measured at 25° C in folded capillary cells (U-shaped cells with two gold plated beryllium/copper electrodes at the top) with a Zetasizer Nano ZS (Malvern Instrument, Malvern, Worcestershire, UK), equipped with a 633 nm laser and with a Litesizer 500 (Anton Paar GmbH, Anton Paar, Austria) equipped with a 658 nm laser. Before each measure, the cells were cleaned with mQw and then filled up with sample, checking that the gold-plated electrodes were fully immersed in the solution and no bubbles were present in the cell. Sample was diluted 1:4 V/V with a 1 mM NaCl solution (1 ml total volume), for Zetasizer Nano ZS instruments, and 1:50 V/V with 1 mM NaCl solution (0.5 ml total volume), for Anton Paar instruments, to increase the conductivity of the solution.

### 2.3.5 Fourier Transform Infrared (FTIR) spectroscopy

Fourier transform infrared (FTIR) spectroscopy is a common spectroscopic technique used to obtain precise information about chemical composition of organic and inorganic compounds. IR spectra result from the absorption of electromagnetic radiation at well-known frequencies that are characteristics of specific bonds inside the molecule. In general, molecular vibrations (as stretching and/or bending) possess the same energy of the infrared electromagnetic waves and can be observed and measured through absorption at specific frequencies.[95], [96]

IR spectra can be divided into two main regions (Fig. 2.4), generated by two different signals:

- The ones related to the functional groups
- The ones proper and characteristic of the molecule, the fingerprint region.

Due to the unicity of the fingerprint region, that is specific for every single compound, this technique is particular useful to verify the presence of a specific compound inside a complex

mixture of materials, because its presence is confirmed by the observation of its fingerprint inside the spectrum of the complex mixture, or to investigate modification of the chemical structure of a material due to covalent bond, because these modification produce alteration in the fingerprint region.

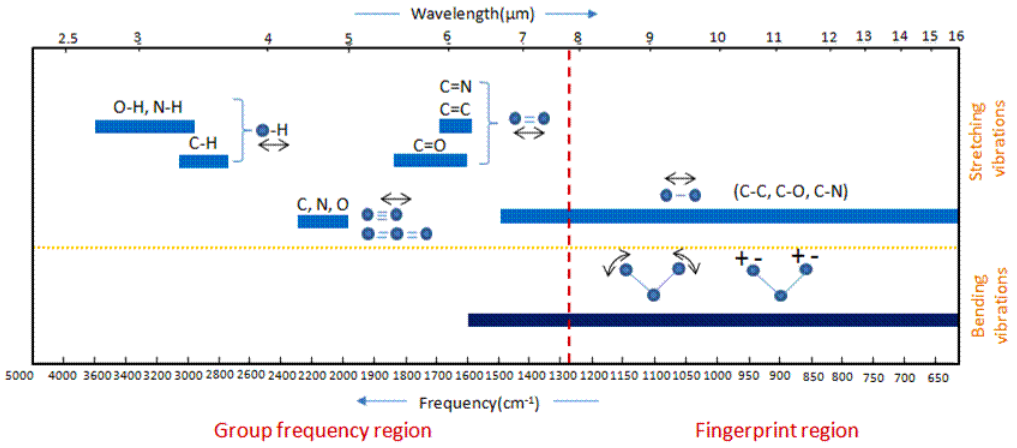


*Figure 2.4: Group frequencies and fingerprint regions in the infrared spectrum.*[97]

FTIR spectroscopy, allows the simultaneous measurement of all the infrared frequencies, rather than individually, as in simple IR spectroscopy, by means of a simple optical device called interferometer. The resulting signal, called interferogram, contains the information about every infrared frequency coming from the source. In order to obtain a plot of the intensity at each individual frequency, the interferogram is decoded by means of Fourier transformation. This transformation is performed by the software, leading to the desired spectral information (Thermo Fisher Scientific).

In this work FTIR analysis was initially performed to verify the presence of PERFECTA inside a polymeric film obtained during the preparation protocol after the evaporation of the solvent to fully remove the organic solvent, later was also used to verify the composition of the obtained NPs and thus the presence of PVA, sodium cholate and PLGA in the different nanoformulations. FTIR spectra were measured with a Thermo Scientific Nicolet iS50 FTIR spectrometer, equipped with iS50 ATR accessory (Thermo Scientific, Madison, USA). The IR signal values were expressed in wavenumber ($cm^{-1}$) and rounded to the nearest whole number through automatically assignment using OMNICTM IR software. A drop of the

nanoformulation dispersed in mQw was deposited on the instrument and dried before the spectra acquisition. Air was recorded as background. The analysis was made in transmittance mode in a wavenumber window of 4000-400 $cm^{-1}$.

### 2.3.6 Nuclear Magnetic Resonance (NMR) spectroscopy and quantitative Nuclear Magnetic Resonance (qNMR) spectroscopy

Nuclear Magnetic Resonance (NMR) Spectroscopy is an analytical technique used for the determination of the chemical structure and composition of compounds exploiting the nuclear magnetic resonance properties of isotopes (generally $^{1}H$, $^{13}C$, $^{15}N$,$^{19}F$ and $^{31}P$). Atoms with at least one between atomic mass (A) or an odd number (Z) of angular momentum, called spin (I), are detectable. The positively charged nuclei, due to the spinning, generate a magnetic momentum (μ) equal to:

$$\mu = \gamma h I \quad (9)$$

Where, γ is the gyromagnetic ratio, defined as the ration between magnetic momentum and angular momentum, $h$ is the Plank's constant divided by $2\pi$ and $I$ is the spin. When an external magnetic field ($B_0$) is applied, the magnetic momentum of the nuclei is affected by $B_0$ and, for atoms with I =1/2, can align parallel (+z) or antiparallel (-z) to the external field due to a processional motion at the Larmor frequency. These two configurations possess different energies (Zeeman effect), where the parallel orientation is at the lower energy while the antiparallel one is at a higher energy state. The parallel orientation is energetically favoured, this is also defined by Boltzmann's law:

$$\frac{n(+\frac{1}{2})}{n(-\frac{1}{2})} = exp(\frac{\Delta E}{kT}) \quad (10)$$

Where n is the population of a spin state, k is the Boltzmann's constant, T is the absolute temperature (express in Kelvins) and $\Delta E$ is the energy difference between the two spin states, equal to:

$$\Delta E = \gamma \frac{h}{2\pi} B_0 \quad (11)$$

As showed in Fig. 2.5 $\Delta E$ is directly proportional to $B_0$.[98]

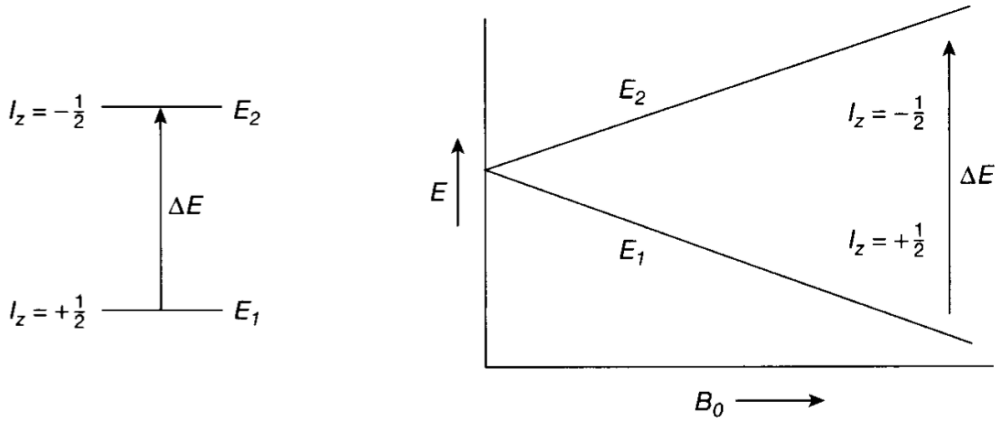


*Figure 2.5: The energy difference between spin states as a function of the external magnetic field $B_0$.*[98]

In addition to $B_0$, an electromagnetic radiation, in form of radiofrequency pulse (RF) is used to detect the magnetic moments of these nuclei. Following the RF pulse, the spins of the lower energy are excited and shift to a more energetic state (absorption process), while switching off the RF the atoms in the upper energetic state, state of non-equilibrium, they continue to rotate into the XY plane generating a signal (FID) detected by a receiver coil until they return to the original equilibrium state. The gradual loss of energy, spin relaxation, can be divided into two different phenomena characterized by two different time constant: the spin-spin relaxation (characterized by the time constant T1) and the spin-lattice relaxation (characterized by the time constant T2). As briefly introduced in 1.1.4, information related to chemical structure and composition rise from peaks and their chemical shifts, where peaks represent specific bonds inside the molecule while chemical shifts of these peaks are associated with groups of surrounding atoms that introduce a shielding effect that reduce the magnetic field felt by the nucleus of the atom.

Moreover, NMR can also be used to determine the concentration of molecules of the analyte inside a complex mixture, this analysis is called quantitative Nuclear Magnetic Resonance (qNMR) spectroscopy. Indeed, the signal in NMR spectroscopy is directly proportional to the number of atoms resonating inside the sample. Through qNMR two different information could be obtained:

- Relative concentration determination, from the molar ratios ($\frac{M_x}{M_y}$) of different compounds and their concentration.

$$\frac{M_x}{M_y} = \frac{I_x}{I_y}\frac{N_y}{N_x} \quad (12)$$

Where I are the integral values and N the number of nuclei giving rise to the signal. [99]

- Absolute concentration determination, by comparing the integral value with a standard.

$$C_x = \frac{I_x}{I_{cal}}\frac{N_{cal}}{N_x}C_{cal} \quad (13)$$

Where I, N and C are the integral area, number of nuclei and concentration of analyte (x) and the standard (cal), respectively.[99]

Both analyses required a reference, a compound of which is known the exact concentration or the number of atoms of interest inside it. This reference can be internal, if putted directly inside the NMR tube with the sample, or external, if loaded inside a coaxial insert and physically divided by the sample.[100]

The presence of PERFECTA inside the different formulations developed during our study was tested by qNMR in order to evaluate the loading efficiency and to observe any structural modifications following the thermal manipulations. Formulations were analysed with an external reference for absolute concentration determination, a total of 400 µl of pure formulation was added inside a co-axial NMR tube with the reference standard placed inside. Each analysis was performed with 256 averages, 14500 points/scan, centred in -73 ppm and with a spectral width of 10 ppm. The reference was prepared by adding a total amount of trifluoroacetic acid (TFA) sufficient to have a final concentration of 1.5e20 $^{19}$F/ml to deuterium oxide ($D_2O$) and 100 µl of this solution was placed inside the standard tube. In addition, samples were also analysed with a large spectral width (100ppm) in order to evaluate the presence of any potential contamination in the formulation.

Labelled cells, after MRI investigations, were collected and analysed by NMR to confirm MRI data. A total amount of 200 000 cells (in a total volume of 50 µl) were collected and resuspended into 500 µl with mQw from which 400 µl was picked up and added inside a co-axial NMR tube containing the standard. Each acquisition was performed with 256 average, 14500 points/scan, centred in -73 ppm and with a spectral width of 10 ppm. The standard was prepared by adding trifluoroacetic acid (TFA) at a concentration of 6e17 $^{19}$F/ml in deuterium oxide ($D_2O$) and used 100 µl of this solution as standard reference.

All the NMR spectra were recorded on a Bruker AV400 spectrometer and data evaluation was done with MestreNova 10.0 from Mestre-Lab. In the result section chemical shifts are reported in parts per million (ppm).

### 2.3.7 Cell Culture

Immortalized murine microglial cell-line (BV-2) (kindly provided by Dr. R. Furlan's lab, San Raffaele Hospital, Milano) was used as *in vitro* model for cell labelling assays system. BV-2 cells was stored at -80°C in cryovials containing 10 million cells inside a cryogenic mix composed by FBS and 10% dimethyl sulfoxide (DMSO), cells was defrosted the week before the *in vitro* experiment, washed in Dulbecco's modified Eagle's medium (DMEM; Lonza), containing 10% fetal bovine serum, 100 mg/ml streptomycin, 100 U/ml penicillin and 2 mM glutamine (Gibco-Invitrogen) and seeded in T75 or T175 flasks, according to the number of cells harvested and needed for the experiment. Cells was incubated at 37°C in 5% $CO_2$ with culture medium to allow them to grow, they were periodically controlled and split into sufficient flask if confluence is reached. The day before the *in vitro* experiment cells are collected from the flask and seeded on 6-multi-well plates (500.000 cells/well) with 1.5 ml of fresh culture medium, they were then incubated at 37°C in 5% $CO_2$. The day designed for *in vitro* experiment the culture medium is changed with fresh one and $^{19}$F-NPs were added to cultures in order to have 1.04e14 $^{19}$F/cell (total volume: 1.5 ml), observed through microscope to verify the condition of the cells after the NPs addition and incubated for 4 hours at 37°C and 5% $CO_2$.

After the 4h incubation culture medium is removed and 0.5 ml of trypsin was added to each well to detach cells from the plate and left to act for 5 min at 37°C, 1 ml of culture medium was added to inactivate trypsin and cells were collected with the help of the scraper. Each well was washed again with 1 ml of culture medium and cells were collected inside a 15 ml Falcon, culture medium was added up to final volume of 10 ml to perform the first wash and 5 ml for subsequent washes.

Cells were washed three times, in culture medium, for 10 min at 300g to remove the excess of NPs resulting suspended in the medium. After the first wash standard trypan blue exclusion method was used to test the cytotoxicity of nanoparticles administered to cells. In particular, 0.4% trypan blue solution was added to an aliquot of cell suspension (1:2 ratio) The haemocytometer was then loaded into a counting chamber and examined immediately under a microscope at low magnification. The percentage of dead cells was estimated counting the number of blue staining cells and the number of total cells. As control, cells without 19F NPs followed the same procedures in the culture medium.

At the end, cells were fixed with 1 ml of 4% paraformaldehyde for 20 min and then washed with PBS. Cells were resuspended in 100 µl of PBS and stored at +4° C.

### 2.3.8 Magnetic Resonance Imaging (MRI)

MRI is a medical imaging technique based on the same explained physical principle of NMR (see paragraph 2.3.6) by adding additional magnetic field gradients to encode the space. The level of image contrasts obtained on the acquired images strongly depends on the chemical composition and physical properties of both tissues and fluids and on the acquisition method used which are a sequence of RF and gradients pulse applied with different time intervals that generate the signal. Through those pulse sequence, sections of patient's body are selected and subsequently divided into a matrix of pixels (2D) or voxels (3D) from which the resulting signal is related to the magnetization of the spins inside tissues (Figure 2.6).

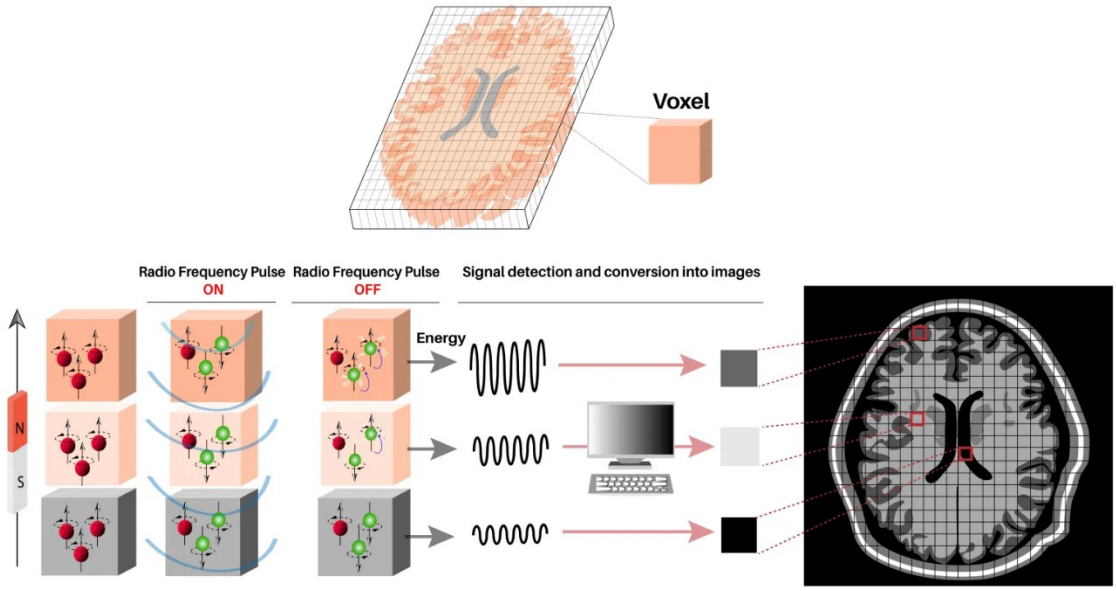


*Figure 2.6:MR imaging process that consist in the acquisition of RF signal from patient's body and its mathematical reconstruction into a 2D grey-scale image based on acquired signals. The brightness of the pixel is determined by the intensity of the RF signal emitted by the tissue voxel.*[101]

The quality of acquired images can be described by: i) tissue contrast sensitivity, ii) the presence of artifacts and iii) the spatial resolution.[30]

The contrast sensitivity is the ability to distinguish tissues with relatively small physical differences or inherent contrast. By changing the acquisition method/parameters, MRI have three intrinsic contrasts (proton density, T1 and T2 relaxation times) able to highlight specific features inside a complex tissue.

The presence of noise background reduces the quality of the image, especially limiting the visibility of low contrast objects and differences inside tissues. Noise in MR images results from random RF energy picked up from the patient's body or, in limited measures, generated by thermal activity inside the electrical circuit of the receiving system. Image quality is not dependent on the absolute value of noise or signal but rather the amount of noise energy in relation to the image signal intensity (signal-to-noise ratio, SNR). The SNR can be improved by increasing the signal average and by reducing the level of noise which depends in part on the imaging sequence (acquisition parameters) and the RF coils used to detect the signal. Indeed, the size of the voxel (spatial resolution) is generally limited by the SNR. The increase

of signal average is also limited to the overall acquisition time that has to be limited for in vivo applications.

To facilitate the MRI analysis on cells, a phantom of agar gel was used in which 12 samples of cells could inserted and image simultaneously.

The phantom was prepared using 2% w/V agar gel (1g of agar in 50 ml of water for phantom), agar gel was poured in a mould and left to rest until solidification of the matrix. MRI references were prepared using nanoformulations with PERFECTA and Pluronic F68 with a concentration of 1 $x10^{19}$ and 2.5$x10^{19}$ $^{19}F$/100 µl, to each reference 100 µl of agar gel (1% w/V) was added to have an homogeneous and stable dispersion of emulsion in the volume of the Eppendorf. Dental cement cap was used to seal the references.

A total number of 300.000 fixed cells were prepared in 100 µl of PBS and putted into 0.2 ml Eppendorf, centrifugated for 5 min at 500g (room temperature) and 50 µl of supernatant was removed from each Eppendorf. Reference and Eppendorf with cells were loaded in the phantom and examined by MRI.

MR Imaging and spectroscopy were performed on a 7T MR system (Biospec, Bruker Biospin) equipped with a horizontal bore magnet (ultra-shielded) and a dual-transmit-receive $^{19}F/^{1}H$ volume coil (35 x 59 mm). $^{19}F$ images were acquired with the resonance frequency centred on PERFECTA, determined with $^{19}F$-NMR according to procedure described in section 2.3.6. Fluorine MR images were acquired by using a 3D-spin echo sequence (number of acquisitions = 80, acquisition time = 40 min) with parameters optimized for a proton density which provides the maximum of signal for detection.

# 3 RESULTS AND DISCUSSION

## 3.1 INTRODUCTION

Different formulations were proposed in this work with the aim to obtain a stable system suitable for cell tracking by $^{19}F$ MRI. PLGA-based NPs were chosen as carriers of PERFECTA in an aqueous environment such as culture media and cytoplasm. Two typologies of PLGA differing for the ending groups were used: carboxylic acids (PLGA-H) and methyl ester (PLGA). PVA and sodium cholate (DS-Na) were chosen as possible stabilizers of the NPs to investigate their effects on the interaction with the cells and NP cellular uptake. Four different NP dispersions, called PLGA-H-PVA, PLGA-PVA, PLGA-H-NaC and PLGA-NaC, were formulated, characterized with different techniques, used for *in vitro* cell labelling and imaged via 7T preclinical MRI.

## 3.2 NANOFORMULATIONS OPTIMIZATION AND PROTOCOL

The formulation protocol used for making NP dispersions was the same for all four types of nanoformulations and was optimized to obtain the maximum efficiency in terms of PERFECTA encapsulation.[71]

The protocol consists in an oil-in-water (o/w) emulsion solvent evaporation with addition of a probe sonication step necessary to provide mechanical energy necessary to stabilize the NPs.

The overall protocol consists of six steps (Fig. 3.1):

1. Dissolution of the surfactant in the aqueous phase and of the polymer and PERFECTA in the organic phase;
2. Mixing of the two solutions and sonication;
3. Mechanical agitation;
4. Solvent evaporation;

5. Centrifugation;
6. Resuspension of the pellets.

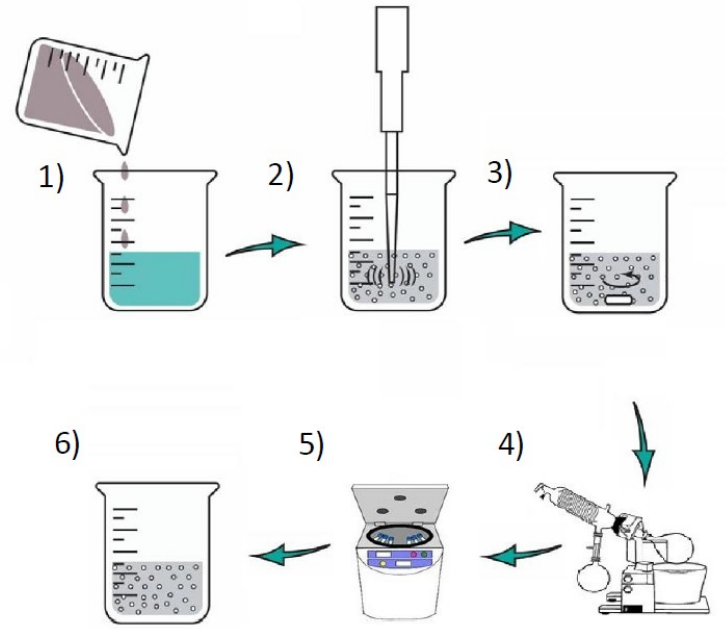


*Figure 3.1: Schematic representation of the adopted protocol of the preparation of PLGA-based NPs. 1) addition of the organic phase to the aqueous phase, 2) probe sonication step, 3) mechanical agitation performed with a magnetic stir, 4) evaporation of the organic solvent at low pressure, 5) centrifugation of the obtained suspension and 6) resuspension of the pellet recovered after centrifugation.*

Different PLGA-based formulations of PERFECTA were developed and tested in this work varying PLGA (PLGA RG 504 and PLGA RG 502H) and the used surfactants (PVA and DS-Na).

*Table 3.1: Nanoformulations proposed in this work:*

| | ***PLGA RG 502H*** | ***PLGA RG 504*** |
|---|---|---|
| **PVA** | PLGA-H-PVA | PLGA-PVA |
| **Sodium cholate** *(DS-Na)* | PLGA-H-NaC | PLGA-NaC |

With the aim to achieve the maximum PERFECTA encapsulation different PLGA/PERFECTA ratios were tried in the range 1 – 10 w/w. PLGA/surfactant ratios were kept constant at 0.83 w/w for DS-Na and 0.2 w/w for PVA, while their concentration in the aqueous phase was kept 0.6% w/V and 2% w/V, respectively.

The first optimization of the nanoformulation was done with PLGA RG 504 (methyl terminated) and sodium cholate. PLGA methyl terminated was chosen for an alleged better affinity with PERFECTA, due to an improved compatibility between hydrophobic methyl groups of PLGA with hydrophobic trifluoromethyl termination of PERFECTA, while sodium cholate was chosen as surfactant principally due to its ability to provide a net negative surface charge able to stabilize the formulation through electrostatic repulsion and to enhance the cellular uptake. All the other formulations were prepared following this optimized procedure and different NP compositions were investigated in terms of stability, PERFECTA encapsulation efficiency and cellular uptake.

DLS measurements were performed at five different time points over two weeks (0, 24h, 48h, 1 week and 2 weeks) to evaluate the stability of the NPs in water. Data acquired were subsequently elaborated to obtain hydrodynamic diameters and PDI, these data were used to determine the stability of the system over time. In Tab 3.2 are showed DLS results obtained for the formulation PLGA-NaC at different PLGA/PERFECTA ratios.

*Table 3.2: PDI and hydrodynamic diameters of PLGA-NaC formulations at different PLGA/PERFECTA ratios. Values are expressed as mean value of the measures obtained over two weeks acquisition, SD is calculated on same data obtained at different time points over two weeks.*

| PLGA/PERFECTA | PDI ± SD | $D_H$ ± SD (nm) |
|---|---|---|
| **1** | 0.18 ± 0.03 | 137 ± 9 |
| **2.5** | 0.17 ± 0.02 | 143 ± 13 |
| **5** | 0.18 ± 0.01 | 119 ± 10 |
| **10** | 0.24 ± 0.01 | 125 ± 6 |

As index of NP stability both PDI and hydrodynamic sizes of these formulations were considered. From data showed in Tab 3.2 it is possible to observe that all formulations are

stable over two weeks with a PDI value lower than 0.25. Only the formulation with a PLGA/PERFECTA ratio of 10:1 showed high values of PDI, principally due to the excess of PLGA which led to the formation of smaller NPs with effects on PDI values.

Beyond stability other used criterion in the determination of the optimal PLGA/PERFECTA ratio was the achieved encapsulation of PERFECTA.

*Table 3.3: Fluorine quantification obtained through $^{19}F$ qNMR of PLGA-NaC formulations at different PLGA/PERFECTA ratios. Theorical $^{19}F$ atoms are the number of fluorine atoms added at the beginning of the formulation procedure and equivalent to 50 mg, 20 mg and 10 mg of PERFECTA, respectively.*

| PLGA/PERFECTA | THEORICAL $^{19}F$ ATOMS ($^{19}F$/ml) | QUANTIFIED $^{19}F$ ATOMS ($^{19}F$/ml) | ENCAPSULATION (%) |
|---|---|---|---|
| **1** | 10.8 x$10^{20}$ | 0.76 x$10^{20}$ | 17.7 % |
| **2.5** | 4.30x$10^{20}$ | 0.18 x$10^{20}$ | 10.4 % |
| **5** | 2.15 x$10^{20}$ | 0.16 x$10^{20}$ | 14.7 % |
| **10** | 2.15 x$10^{20}$ | 0.07 x$10^{20}$ | 6.6 % |

As show in Tab 3.3 the best encapsulation was achieved with 1:1 PLGA/PERFECTA ratio, where 17.7% of the total amount of PERFECTA was recovered at the end of the formulation. The worst result was obtained for the formulation with a 10:1 ratio, where the high amount of PLGA led to the formation of NPs only composed by polymer and surfactant without encapsulation of PERFECTA that was lost during organic solvent evaporation and centrifugation.

From DLS measures and encapsulation values the 1:1 PLGA/PERFECTA ratio was chosen as the best ratio for further formulations, due to good colloidal stability proved by a relatively low PDI (0.18 ± 0.03) related to a reasonably small size (137 ± 9 nm) over two weeks and the best PERFECTA encapsulation.

EtOAc, as said before, was the only non-fluorinated solvent able to dissolve PERFECTA. To improve PERFECTA encapsulation efficiency of these formulations, according to previously works done on other PERFECTA nanoformulations, PERFECTA was melted at 80° C before adding it to the organic phase.[70] This step facilitates the dissolution of

PERFECTA in EtOAc and the homogenization between the aqueous and organic phases. To better improve the homogeneity of the emulsion, the organic phase was added dropwise to the aqueous phase under magnetic stirring.

PLGA RG 502H (carboxylated) was also used to understand if the use of differently functionalized polymer could enhance either the stability or PERFECTA encapsulation of the resulting NPs, while PVA was first introduced after the observation of the loss of colloidal stability of PLGA-NaC NPs in PBS, even if lately we verified that this effect does not occur in the cell culture medium, probably due to an effect of the FBS and probably formation of the protein corona.

*Table 3.4: DLS and $^{19}$F-qNMR data for PLGA-NaC formulations with and without melting of PERFECTA before its addition to the organic phase.*

| **PERFECTA MELT** | **PDI ± SD** | **$D_H$ ± SD (nm)** | **ENCAPSULATION (%)** |
|---|---|---|---|
| **YES** | 0.24 ± 0.01 | 103 ± 5 | 31 % |
| **NO** | 0.15 ± 0.01 | 103 ± 2 | 21% |

The melting of PERFECTA increases the PDI of the system, probably due to a thermal effect on PLGA, but almost double the encapsulation of PERFECTA without showing effects on dimension of NPs as showed in Tab 3.4.

PLGA-H-PVA, PLGA-PVA and PLGA-H-NaC were formulated and analysed to verify the stability of these new nanoformulations and to understand if the melting of PERFECTA could have effects on them. From data acquired all formulations demonstrate better or equal stability with respect to PLGA-NaC one, while negligible effects on stability caused by the melting of PERFECTA were observed. In term of encapsulation efficiency PVA stabilized NPs showed a little improvement, respect to PLGA-NaC, with results between 30% and 40% depending on formulation, PLGA-H-NaC showed result comparable to those obtained for PVA stabilized formulations.

PVA based NPs showed a dimension between 180 nm and 200 nm, proving that PVA has a greater contribution in final dimension of NPs respect sodium cholate.

Further optimization was achieved increasing centrifugation time as the presence of NPs in the recovered supernatant after a second centrifugation was observed. The recovered and re-suspended pellet after the second centrifugation was analysed with 19F qNMR demonstrating the presence of PERFECTA in an amount from 3% to 7% of the total amount of fluorine atoms in the formulation. Doubling the centrifugation time, it was possible to achieve a good yield without losing colloidal stability of the nanoformulations as no effects on PDI and dimension were observed.

In detail, the optimized formulation protocol consists of the following steps:

- PERFECTA is taken in a glass vial and put in a thermoblock at 80° C to melt it,
- PLGA is taken in a glass vial and dissolved in EtOAc and sonicated in an ultrasound bath at 59 kHz for a time needed to ensure the complete dissolution of PLGA,
- Sodium cholate (0.6% w/V) or PVA (2% w/V) is dissolved in 4 ml of mQw and 5 ml of mQw, respectively. After complete dissolution, the aqueous phase is transferred into a 25 ml round-bottomed flask,
- Melted PERFECTA is collected with the addition of EtOAc and mixed with PLGA, the obtained solution is sonicated in an ultrasound bath at 59 kHz,
- The organic phase is added dropwise to the aqueous phase while kept stirring,
- Solution is sonicated using a tip sonicator at 40% amplitude for 25 s,
- Solution is magnetically stirred for 3 h at room temperature,
- Organic solvent is removed through evaporator starting from 250 mbar, lowering to 170 mbar and then lowered by 10 mbar step until 70 mbar and keep working for 15 min,
- The obtained aqueous solution after evaporation is collected in a 15 ml Falcon tube and centrifugated at 10000 rpm for 40 min at 4°C,
- The obtained pellet upon centrifugation is re-suspended in 1 ml of mQw.

The optimised protocol permits to formulate stable NPs with an amount of encapsulated fluorine atoms sufficiently high to label cells with a concentration detectable with MRI.

## 3.3 NANOPARTICLES CHARACTERIZATION

The NPs used for *in vitro* experiments were characterised to obtain their effective composition by FT-IR spectroscopy, their sizes by DLS and NTA, their colloidal stability by ζ-potential measures and their PERFECTA encapsulation efficiency by $^{19}$F-NMR spectroscopy.

### 3.3.1 Composition

FT-IR spectroscopy was initially used to verify the presence of PERFECTA inside the nanoformulation and lately of each material used in the formulation. The analysis of the IR spectra of fluorinated compounds is complex, and its complexity rises from the number of fluorine atoms in the molecule, because these compounds exhibit a whole series of intense bands in the region between 1350 – 1100 $cm^{-1}$ [95], but these peaks are not useful to identify PERFECTA in the formulations because in the same region are also located the C-O bonds vibrations related to the ester and acid groups of PLGA, sodium cholate and PVA. Due to this overlap of the vibrations of interest, the better way to verify the presence of the fluorinated compound in these NPs relies in the direct confront of the spectra of PERFECTA with those of the proposed formulations and looking at common peaks.

In Fig. 3.2 the fingerprint region in the IR spectrum relative to PERFECTA is compared to the same region in the IR spectra of the nanoformulations. The only specific peak of PERFECTA observable in the NP spectra are the two strong peaks around 730 $cm^{-1}$, thus these will be used to confirm the presence of PERFECTA inside the nanoformulations proposed.

In Fig. 3.3 are showed the spectra of PLGA-H-PVA, PLGA-H-NaC, PLGA-PVA and PLGA-NaC formulations, were the presence of fluorinated compounds inside the nanoparticles are confirmed by the presence of the two peaks defined before as characteristic of PERFECTA. Importantly, the FT-IR analysis can confirm presence of PERFECTA in the NPs as PERFECTA is susceptible of sublimation and during the evaporation at low pressure of the organic phase the free amount of fluorinated compound is lost.

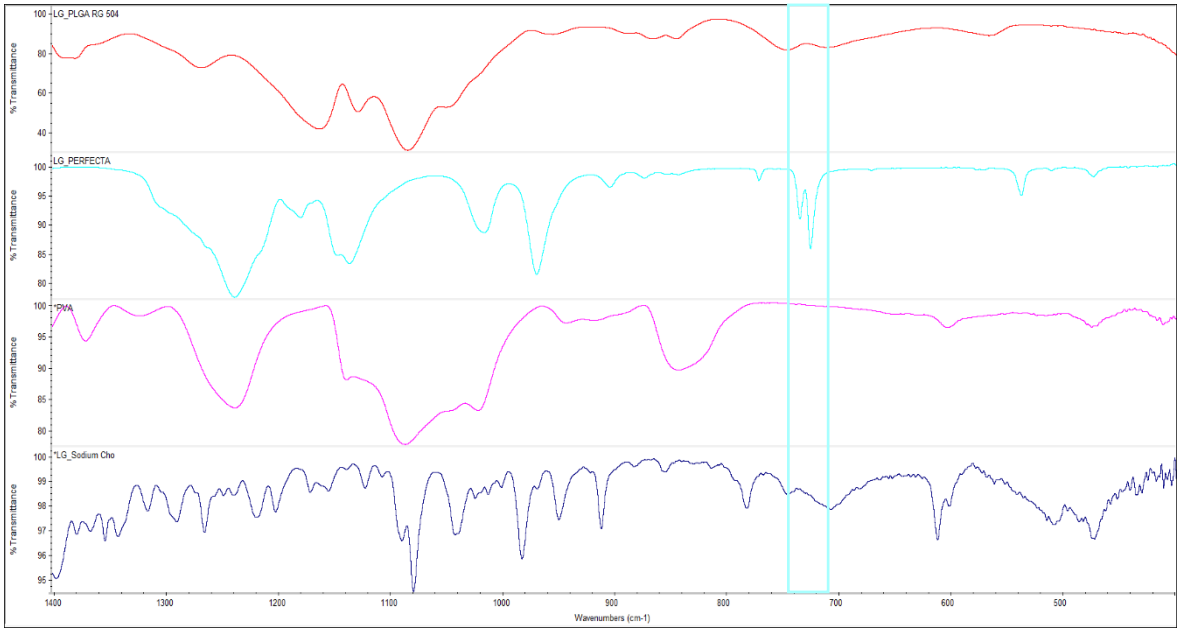


*Figure 3.2: Fingerprint FT-IR spectra of PVA, PLGA RG 504, sodium cholate and PERFECTA. The box highlight the region chosen due to the presence of two intense peaks at 727 and 736 $cm^{-1}$ not observable for other compounds.*

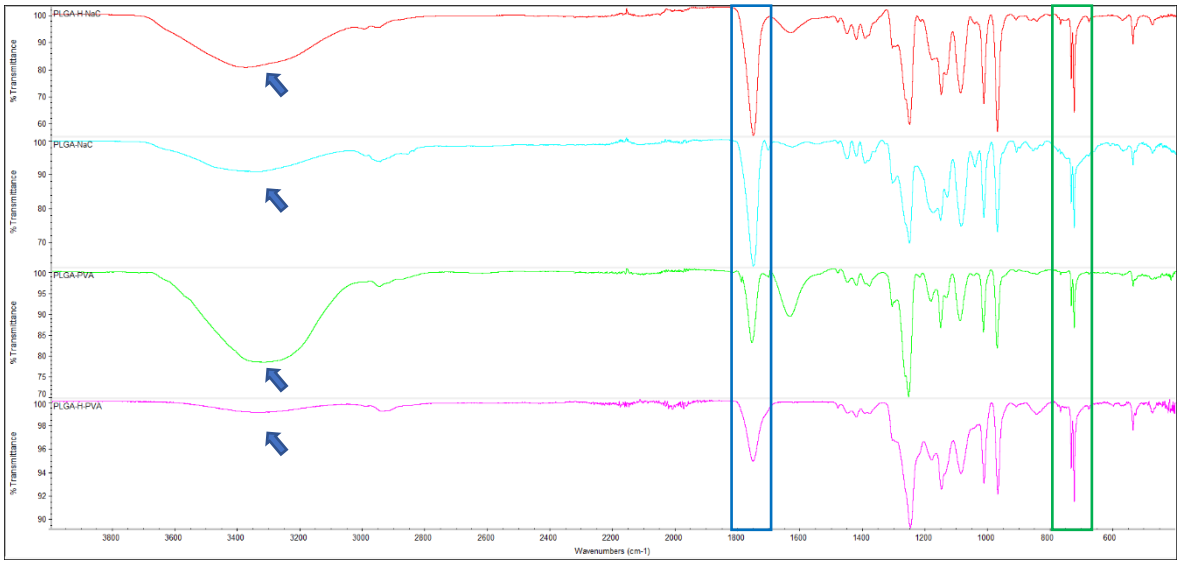


*Figure 3.3: FT-IR spectra of PLGA-H-NaC, PLGA-NaC, PLGA-PVA and PLGA-H-PVA formulations. The green box highlights the peaks used to verify the presence of PERFECTA (C-F bond stretching) while blue box highlights the C=O bond stretching characteristic of PLGA polymers backbone. Blue arrows point to the region characteristic of C-H bonds of PVA and sodium cholate.*

The confirmation of the presence of PERFECTA through FT-IR was crucial at the beginning of this work because in literature it is reported that the encapsulation of PERFECTA in PLGA NPs cannot be achieved without the use of a second PFC or a fluorinated surfactant.[72]

This was further confirmed through $^{19}$F-NMR where it was possible to observe the characteristic single and sharp peak of PERFECTA at -73.3 ppm. In Fig. 3.4 $^{19}$F-NMR spectra for a PLGA-PVA formulations are reported: it is possible to observe the characteristic peak of PERFECTA and a second peak, at -76.5 ppm, related to TFA used as standard for the quantification. A second spectrum (Fig. 3.5) was acquired increasing the acquisition windows looking for impurities or artefacts. The presence of the two expected peaks confirms that the nanoformulation is only loaded with PERFECTA and no artefacts are raised during the acquisition of the first spectrum.

The presence of PLGA is confirmed by the presence of the intense peak around 1800 cm$^{-1}$ observable in Fig.3.3, characteristic of the C=O bond (stretching) present in high number inside the PLGA structure. Sodium cholate and PVA presence are verified by the broad peaks in the region between 3700-3100 cm$^{-1}$ that is characteristic for O-H stretching, bond present in high number inside the molecular structure of both surfactants.

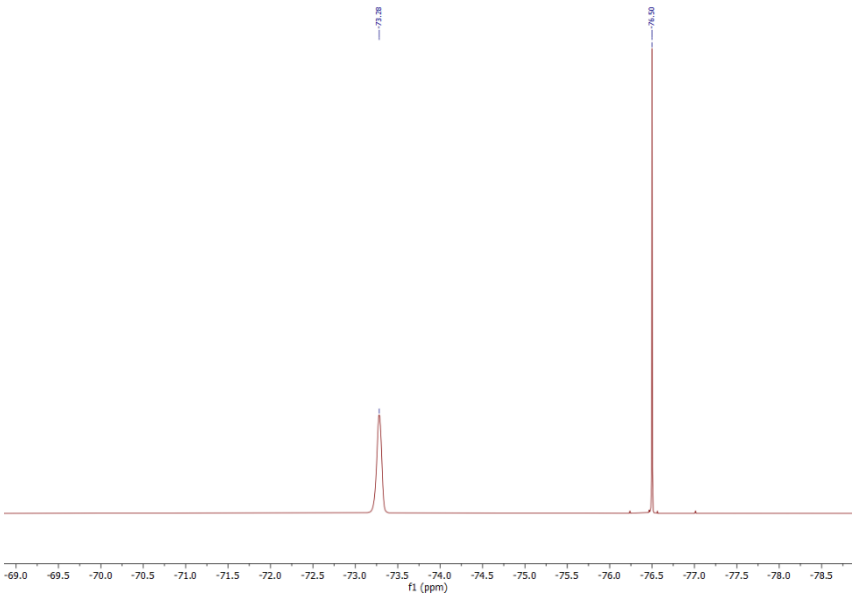


*Figure 3.4: $^{19}$F-NMR spectra of PERFECTA and TFA (standard for quantification). The sharpness of the PERFECTA peak (-73.3 ppm) confirms that no chemical modification occurs during formulation.*

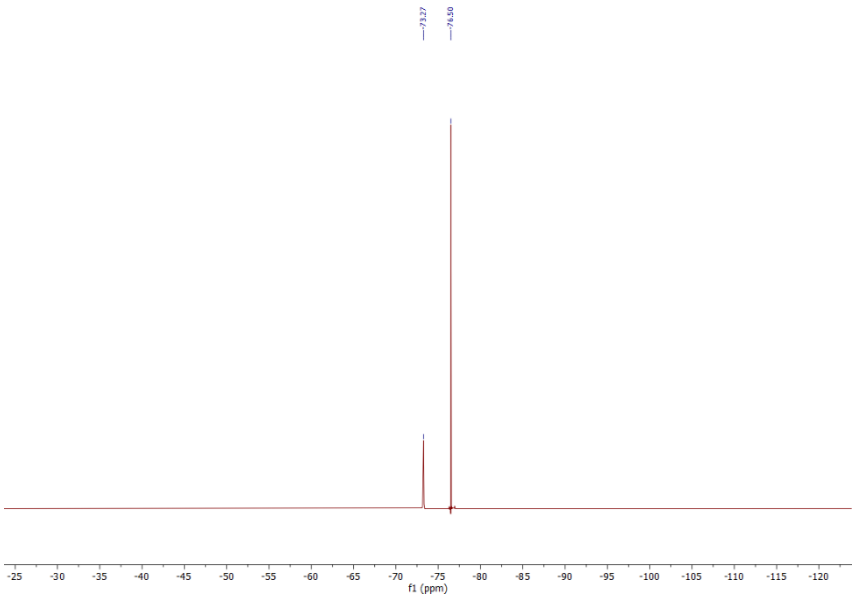


*Figure 3.5: 19F-NMR spectra of PERFECTA and TFA acquired using a wider window for investigation of impurities inside the formulation and to verify the absence of artefacts raised from the cut-off effects at the extremities of the window.*

### 3.3.2 Colloidal stability of the PERFECTA loaded PLGA NPs

Hydrodynamic diameters and colloidal stability of all nanoparticles were evaluated through DLS and NTA analysis and ζ-potential measurements. DLS analysis were performed in diluted conditions (1:100 V/V ratio of the stock in mQw) at four different angles (70°, 90°, 110° and 130°) at three time points (T0, 24h and 48h). These measures were performed to verify the stability of the formulation over time.

Data obtained from DLS measurements ($D_H$ and PDI) are plotted in the graph showed in Fig. 3.6, from which is possible to observe the different behaviour related to the two surfactants used. Indeed, PVA permits to obtain larger NPs with a very low PDI while NaC stabilized NPs are more heterogeneous systems with an overall lower diameter.

The mean values and standard deviations are reported in Tab. 3.5 and the autocorrelation functions at 90° scattering angle and relative unweighted size distributions are shown in Fig. 3.7.

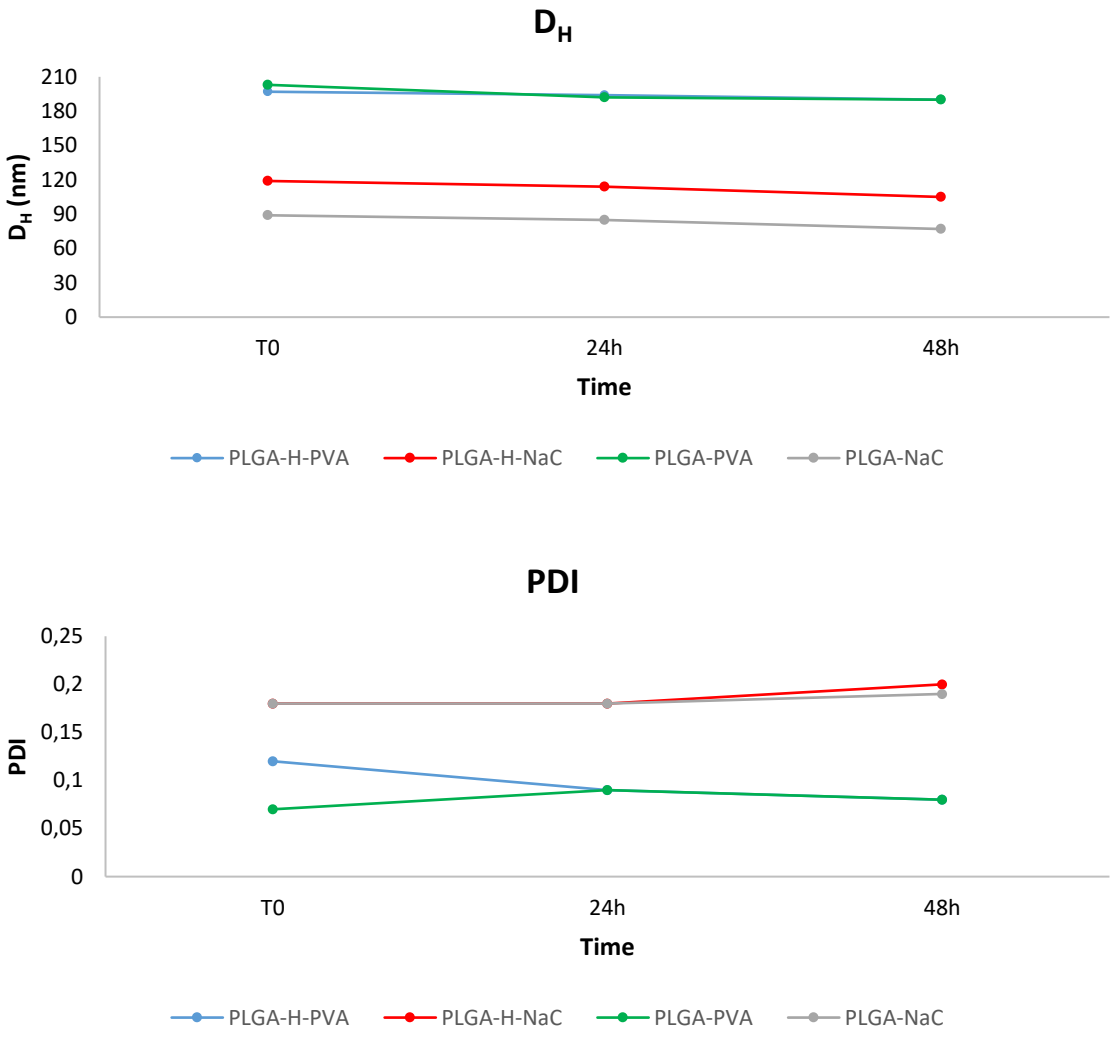


*Figure 3.6: Hydrodynamic diameter of the four formulations (upper) and PDI measurements (lower) over three days.*

*Table 3.5:Measure of hydrodynamic diameters and PDI values for the obtained formulations. Results are expressed as mean values over three time points. SD are calculated on same data.*

| FORMULATION | $D_H$ ± SD (nm) | PDI ± SD |
|---|---|---|
| **PLGA-H-PVA** | 194 ± 4 | 0.10 ± 0.02 |
| **PLGA-H-NaC** | 113 ± 7 | 0.19 ± 0.01 |
| **PLGA-PVA** | 195 ± 7 | 0.08 ± 0.01 |
| **PLGA-NaC** | 84 ± 6 | 0.18 ± 0.01 |

The proposed formulations are all stable with mean values of PDI lower than 0.25, threshold value for NPs stability in the aqueous environment, these values are stable over three days, confirmed by a low standard deviation. These data are confirmed by autocorrelation functions where no effects of abnormal scattering could be observed. Higher polydispersity values of PLGA-H-NaC and PLGA-NaC formulations are related to a more heterogeneous system composed of NPs with a broader distribution, as observable from unweighted size distributions, with respect to the very sharp distributions of PLGA-H-PVA and PLGA-PVA. Hydrodynamic diameters are in range with formulations obtained during the optimisation of the protocol, with negligible variations during the three days of analysis, demonstrating again the stability of these systems.

The only exception can be observed for PLGA-NaC, where the dimension obtained in this formulation is lower than expected, but due invariance of the size and acceptable PDI values was considered stable and used for cell labelling experiments.

Same consideration was done on PLGA-H-NaC formulation, where the size profile at 48 h was not optimal but from data acquired no evidence of instability was observed.

For PLGA-H-NaC and PLGA-NaC can be observed a smaller peak in the range 8-20 nm of radius, these are related to sodium cholate micelles present in low number inside the NPs dispersion. Due to low number in which they are present inside the emulsion minor importance was given to them.

Formulations stability were further confirmed by Nanoparticles Tracking Analysis (NTA) acquisition.

Comparing result exposed in Tab 3.6 with those obtained from DLS (Tab 3.5) it is evident a difference, especially for what concerns the hydrodynamic diameter and size distributions of these NPs. These differences are related to the different way by which the mean $D_H$ values are calculated and to the fact that DLS give an intensity weighted distribution, that is better to detect aggregates, while NTA give a number weighted distribution, that provide a higher resolution for polydisperse distributions. Thus, NTA gives a mode value, representative of the estimated $D_H$ value common to the higher number of NPs inside the dispersion, which is closer to the DH value calculated through DLS measurements.

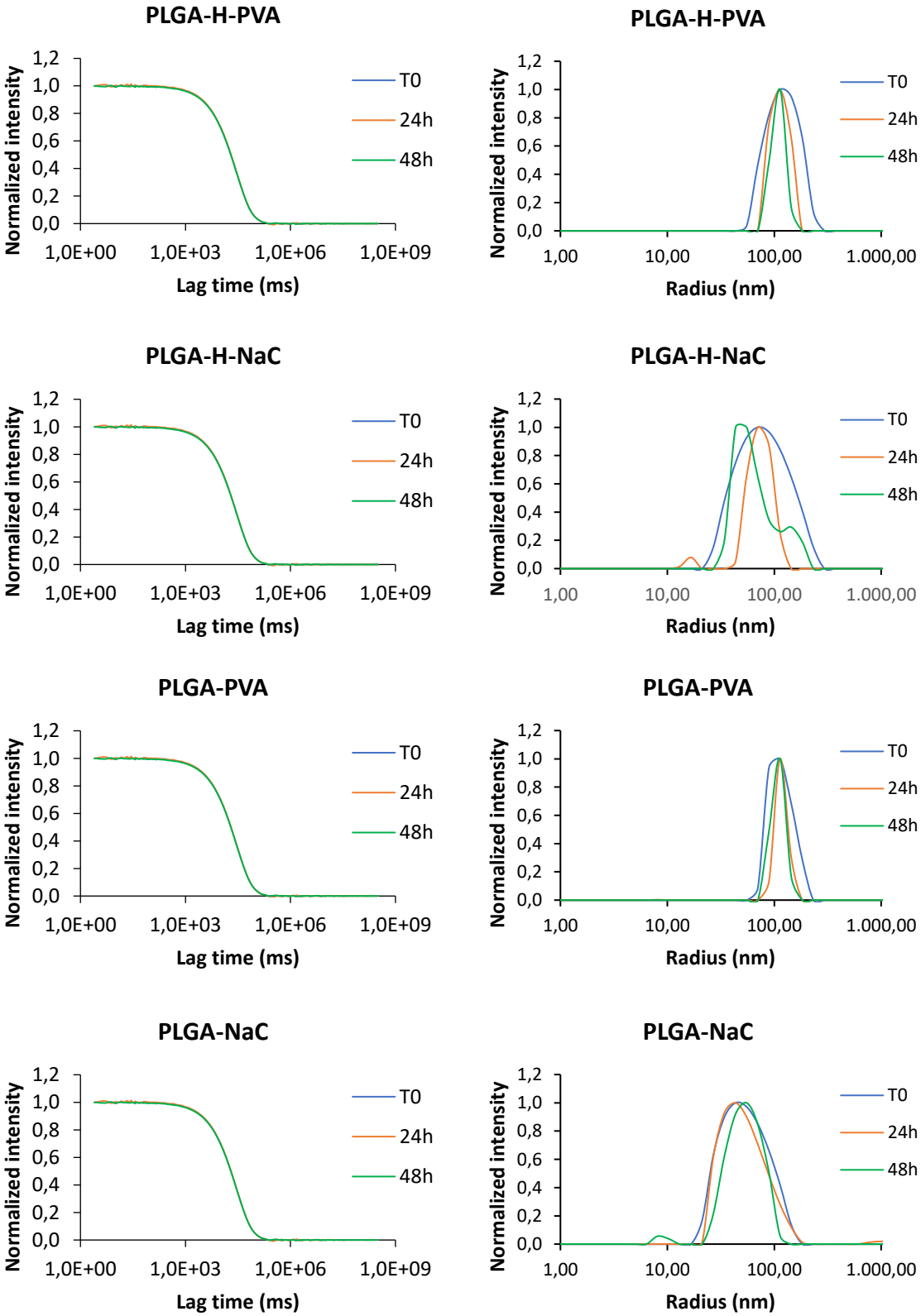


Figure 3.7: Correlation function (left column) and unweighted size distribution (right column) for nanoformulation administered to microglial murine BV-2 cells line taken at three different time points and 90°.

Moreover, the results from NTA experiments give a mean hydrodynamic diameter, $D_H$, a standard deviation (SD) and the mode value. SD indicates the broadness of the Gaussian distribution and according to the obtained values it is possible to understand if the NPs in the solution are polydisperse, the same information can be achieved comparing the values of $D_H$ and mode, more these two value are similar more the NPs are monodispersed.

*Table 3.6: Mean hydrodynamic diameter, standard deviation and mode obtained from NTA measurement. The SD values expressed are related to the broadness of the gaussian curve characteristic for the size distribution of these NPs. These values provide an idea of the polydispersity of the NPs.*

| FORMULATION | $D_H$ (nm) | SD (nm) | MODE (nm) |
|---|---|---|---|
| **PLGA-H-PVA** | 203 | 65.2 | 166 |
| **PLGA-H-NaC** | 136 | 53 | 117 |
| **PLGA-PVA** | 203 | 59 | 181 |
| **PLGA-NaC** | 156 | 58 | 140 |

The NTA size distributions relative to the data shown in Tab 3.6 are reported in Figure 3.8. PLGA-NaC NPs, for which $D_H$ and mode have similar values, possess a really sharp profile, while the SD is still relatively high due to two lower peaks above 200 nm, PLGA-H-NaC NPs show a slightly higher difference between mean value and mode diameter, but the standard deviation of this formulation is lower due to a more homogenous distribution in size. Both PLGA-H-PVA and PLGA-PVA formulations, being composed by larger NPs, show broader distributions with respect to those stabilized with sodium cholate. The difference in sharpness of the size distributions obtained from NTA and DLS experiments is related to a better sensibility of NTA to smaller NPs.

ζ-potential measures were also performed to further verify the colloidal stability of the formulated suspensions and to investigate how the surface charge can influence NP cellular uptake. NPs were diluted with 1 mM NaCl solution to provide a sufficient conductivity to run the measurements. In Tab. 3.7 ζ-potential values are shown, while in Fig. 3.9 ζ-potential distributions for NPs dispersions in 1 mM NaCl (obtained with an Antoin Paar Litesizer 500 instruments).

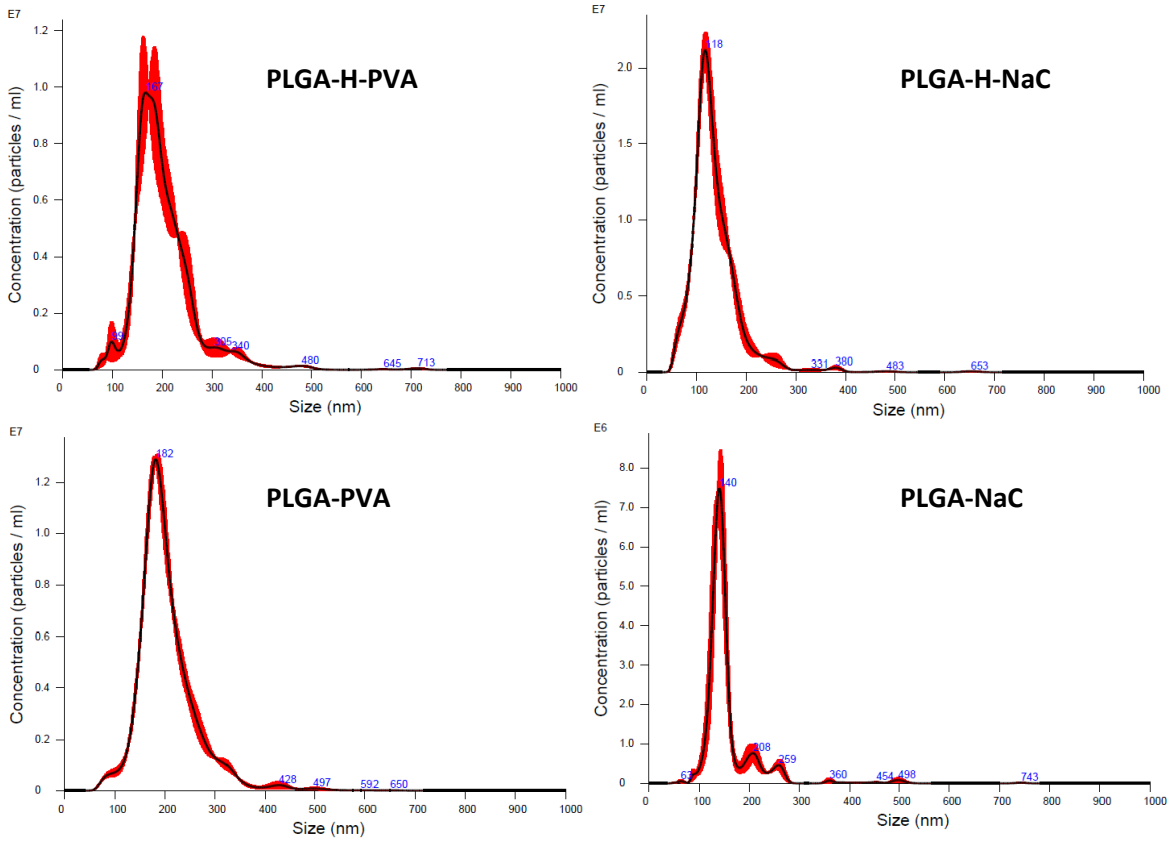


*Figure 3.8: NTA size distributions of the obtained formulations performed with NanoSight NS 300. The red profile represents the concentration profile of the NPs as a function of the hydrodynamic radius.*

*Table 3.7: Mean Zeta-potential values, standard deviation and conductivity of nanoparticles measured in a dilution 1:50 (V7V) in 1 mM NaCl solution.*

| FORMULATION | Z-POTENTIAL (mV) | SD (mV) | CONDUCTIVITY (mS/cm) |
|---|---|---|---|
| **PLGA-H-PVA** | - 5.2 | 0.2 | 0.124 |
| **PLGA-H-NaC** | - 43 | 0.2 | 0.105 |
| **PLGA-PVA** | - 5.4 | 0.2 | 0.125 |
| **PLGA-NaC** | - 39 | 0.6 | 0.102 |

Is known that sodium cholate stabilizes the NPs conferring a net negative charge and providing a slipping plane able to maintain the colloidal stability. PVA, instead, is known to shield the negative charge that rises from the deprotonation of the carboxyl group of PLGA

decreasing the surface charge of the system, but due to its high molecular weight PVA stabilizes the system through steric interaction. These different stabilization effects are confirmed by data, where both PVA stabilized NPs show a low surface charge (-5 mV) while sodium cholate stabilized formulations possess a net negative charge around -40 mV.

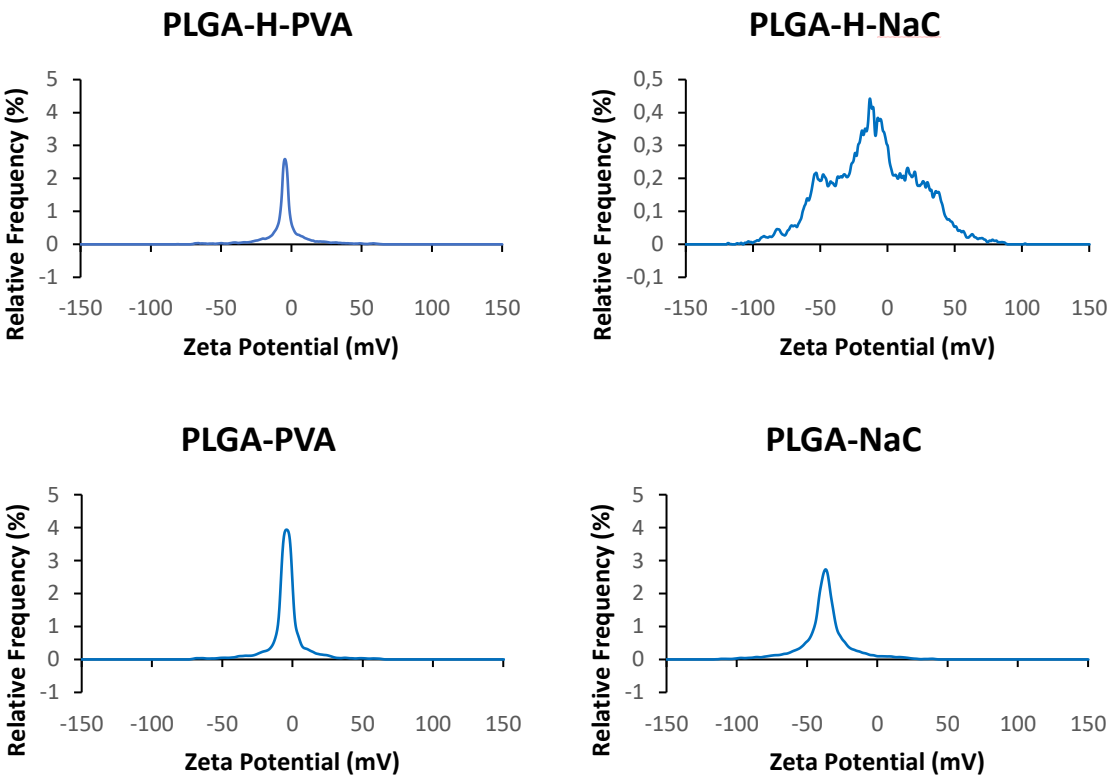


*Figure 3.9:Zeta-potential distribution of NPs in dilution 1:50 in 1mM NaCl solution.*

The ζ-potential distributions appear quite sharp, resulting in a surface charge common to most of the NPs that compose the system. The only exception is related to PLGA-H-NaC formulation for which the distribution appears particularly broad and for which the relative frequency is quite low compared to those of the other formulation distributions.

PLGA-H-PVA and PLGA-H-NaC NPs were also measured in mQw to check the behaviour of these formulations in absence of external ions. The obtained results, Tab. 3.8, and ζ-potential distributions (Fig. 3.10) confirm what said above about sodium cholate formulation and its role in the electrostatic stabilization of NPs. For what concerns PVA stabilized

formulations it is evident the presence of a shielding effect of free ions in 1 mM NaCl solution, in fact removing the salt the mean value of the ζ-potential passes from -5 mV to -27 mV. Values obtained for PLGA-H-PVA formulations are lower to those obtained for PLGA-H-NaC, and lower with respect to the threshold required for electrostatic stabilization confirming that PVA stabilizes the NPs through steric effects.

*Table 3.8: Mean Zeta-potential values, standard deviation and conductivity of NPs diluted 1:50 in mQw.*

| FORMULATION | Z-POTENTIAL (mV) | SD (mV) | CONDUCTIVITY (mS/cm) |
|---|---|---|---|
| **PLGA-H-PVA** | - 27.2 | 0.7 | 0.004 |
| **PLGA-H-NaC** | - 38.6 | 1.3 | 0.007 |

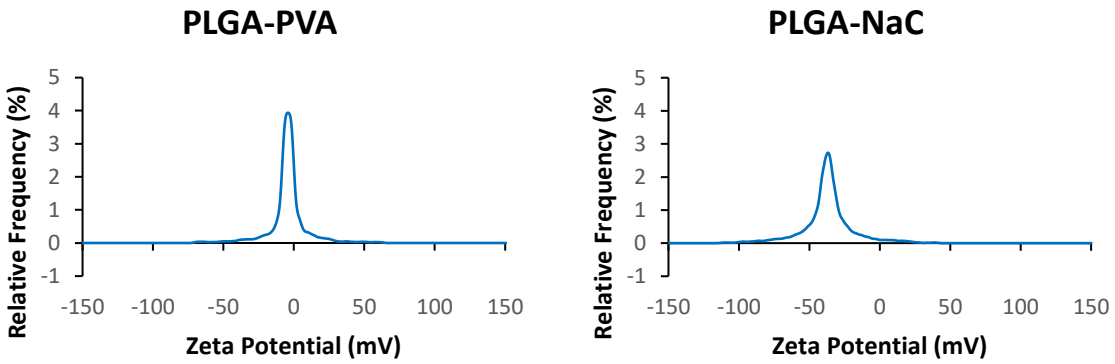


*Figure 3.10: Zeta potential distribution for PLGA-H-PVA and PLGA-H-NaC formulation diluted 1:50 in mQw to verify the shielding effects of $Na^+$ and $Cl^-$ atoms on deprotonated carboxylic groups and alcohol groups of PLGA, sodium cholate and PVA.*

### 3.3.3 $^{19}$F-NMR Analysis and Quantification

One limitation of $^{19}$F-MRI, as said before, is related to is limited sensibility: a $^{19}$F concentration higher than $10^{-3}$ and $10^{-6}$ M is required, based on intensity of the field generated, and equivalent to $2x10^{19}$ – $2x10^{16}$ $^{19}$F/ml. However, for cell tracking by $^{19}$F-MRI the indicated concentration ($2x10^{19}$ $^{19}$F/ml) should be taken as a minimum threshold of the

formulation, also considering that not all formulated NPs will be phagocyted by the cells during incubation. At the same time high concentrations could cause negative effects on cells viability.

Setting the $^{19}$F labelling concentration to 1x10$^{14}$ $^{19}$F/cell and aiming to label a million of cells means that a total amount of fluorine atoms of 1.04x10$^{20}$ $^{19}$F is required. Considering the encapsulation efficiency, it was chosen an initial amount of 6.45 x10$^{20}$ $^{19}$F, which resulted in a final concentration of $^{19}$F of about 3x10$^{20}$ $^{19}$F/ml.

To quantify and verify the exact content of fluorine atoms,$^{19}$F-NMR experiments with an external standard (TFA) were performed. From the acquired spectra comparing the areas of the peaks between PERFECTA and TFA it was possible to determine the total number of $^{19}$F atoms in the measured formulation (thus also their concentration in the stock formulation). In Fig. 3.11 the $^{19}$F-NMR spectrum used for the quantification of fluorine atoms in PLGA-H-PVA formulation.

For the quantification of $^{19}$F concentration the following equation was used:

$$N_f{}^{19F} = \frac{I_f}{I_{std}} x\ N_{std}^{19F} \quad (14)$$

Where: $I_f$ and $I_{std}$ are the integral values of the peak related to PERFECTA and to the standard (TFA), respectively, while $N_f{}^{19F}$ and $N_{std}^{19F}$ are the numbers of fluorine atoms in PERFECTA and in the standard, respectively. The solution of the standard had a total number of fluorine atoms equal to 1.42x10$^{19}$ $^{19}$F.

Substituting the experimental values in the equation (14) it is possible to determine the number of fluorine atoms in the 0.4 mL used for the analysis, from that value the initial concentration of the stock formulation is calculated.

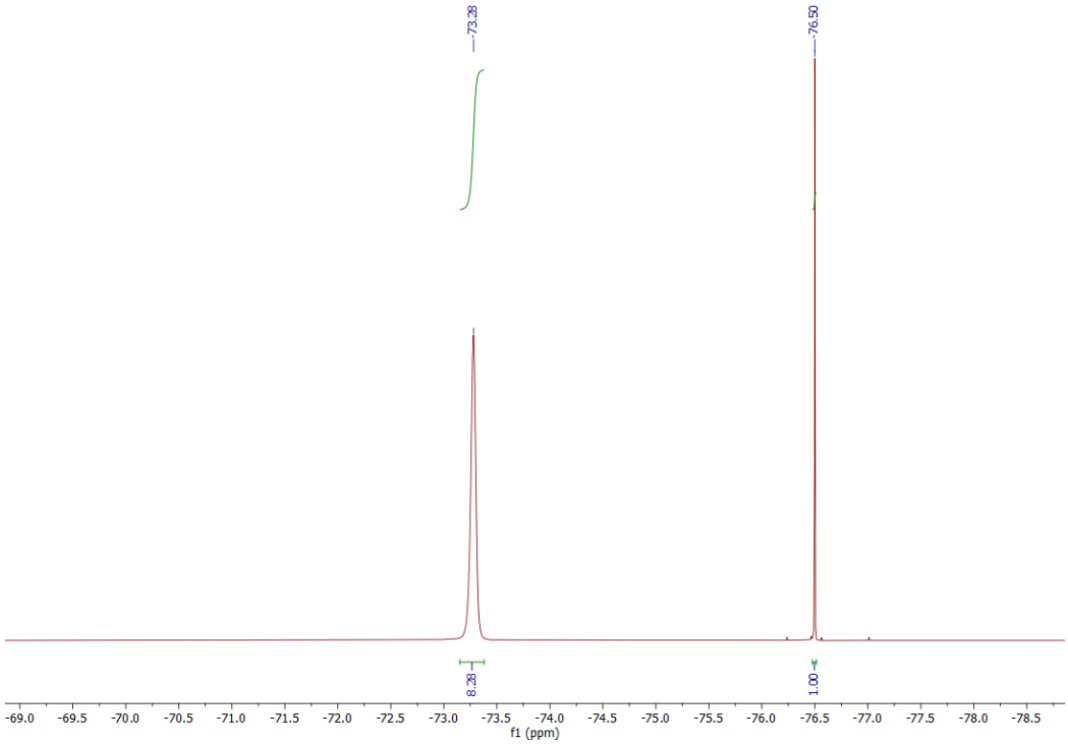


*Figure 3.11: 19F-qNMR spectra of PLGA-H-PVA formulation with integral values used for the quantification of fluorine atoms in the formulation. The integral value of PERFECTA is normalized according to the value obtained from the standard, the normalization is performed by the software when the integral areas are taken.*

*Table 3.9: Fluorine content and encapsulation efficiency measured through $^{19}$F-NMR of the nanoformulation proposed. Theorical $^{19}$F atoms are the number of fluorine atoms added at the beginning of the formulation procedure and equivalent to 30 mg of PERFECTA.*

| FORMULATION | THEORICAL $^{19}$F ATOMS ($^{19}$F/ml) | QUANTIFIED $^{19}$F ATOMS ($^{19}$F/ml) | ENCAPSULATION (%) |
|---|---|---|---|
| **PLGA-H-PVA** | $6.45 \times 10^{20}$ | $2.94 \times 10^{20}$ | 45.6 % |
| **PLGA-H-NaC** | $6.45 \times 10^{20}$ | $2.04 \times 10^{20}$ | 31.6 % |
| **PLGA-PVA** | $6.45 \times 10^{20}$ | $2.96 \times 10^{20}$ | 45.9 % |
| **PLGA-NaC** | $6.45 \times 10^{20}$ | $1.39 \times 10^{20}$ | 21.5 % |

PERFECTA encapsulation efficiencies were determined according to the following equation:

$$\%_{encapsulation} = \frac{Quantified}{Theorical} x100 \quad (15)$$

The results obtained from NMR analysis are in agreement with those found after the protocol optimization on similar formulations, except for the PLGA-NaC that showed a quantity of fluorine atoms lower than it was expected. Experimental losses of PERFECTA could occur during the preparation of the formulation and some differences were also observed by DLS analysis.

Overall, all the formulations are considered good in terms of colloidal stability and encapsulation efficiencies.

The results obtained by $^{19}$F-NMR were lately normalized with the NP concentration estimation measured by NTA to estimate the mean value of $^{19}$F atoms for single nanoparticle and expressed in Tab. 3.10. The number of fluorine atoms encapsulated in a single NP is quite important in the perspective to use these formulations for labelling non-phagocytic cells, where NP uptake is limited due to their nature and in particular to their small size that does not permit the uptake of large amounts of NPs. Thus, a high amount of fluorine atoms in a single NP is preferred for labelling a non-phagocytic cell.

*Table 3.10: Measures of NP concentration (from NTA measurements) and fluorine concentration (from $^{19}$F-NMR) integrated to obtain the value of fluorine content for nanoparticle.*

| FORMULATION | QUANTIFIED $^{19}$F ATOMS ($^{19}$F/ml) | NPS CONCENTRATION [NPs/ml] | $^{19}$F/NP |
|---|---|---|---|
| **PLGA-H-PVA** | 2.94 x$10^{20}$ | 9.8x$10^{12}$ | 3x$10^{7}$ |
| **PLGA-H-NaC** | 2.04 x$10^{20}$ | 2.4 x$10^{12}$ | 8.4 x$10^{7}$ |
| **PLGA-PVA** | 2.96 x$10^{20}$ | 1.2 x$10^{12}$ | 26 x$10^{7}$ |
| **PLGA-NaC** | 1.39 x$10^{20}$ | 0.3 x$10^{12}$ | 45 x$10^{7}$ |

## 3.4 *IN VITRO* EXPERIMENT

In *vitro* experiments were done twice using the obtained formulations described above. The first experiment (data in supporting materials) was aimed to early investigate the cytotoxicity of the NPs. Verified of a good cytocompatibility the labelling was confirmed through MRI. The second experiment was done to better investigate what was observed in the early one.
The formulations were prepared few days in advance with respect to their administration to cells and during those days they were characterized to verify their stability and verify the amounts of $^{19}F$.
These experiments were performed using as model a murine microglial cell-line (BV2), the conditions of cells were verified before their seeding into the culture well, before the administration of the formulation and after 4h incubation of with the NPs.

### 3.4.1 Labelling and Viability

Labelling efficiency of each formulations developed in the present work was compared to the PERFECTA-F68 (F68) formulation initially investigated by Dr. Cristina Chirizzi,[70] that was used as internal standard. For each formulation, two pools of $5x10^5$ cells were incubated with a fixed dose of $1x10^{14}$ $^{19}F$/cell, equivalent to a concentration of PERFECTA of 1.54 mM/well. Due to the instability shown by sodium cholate stabilized NPs in PBS, all formulations were administered dispersed in mQw, while cells were kept into complete culture medium.

Cell viability after labelling was assessed by using the trypan blue exclusion method, that relies on the principle that only dead or dying cells with damaged membranes are stained by trypan blue so the number of dead cells can be quantified using a haemocytometer. As a control, cells without 19F formulations followed the same procedures of labelling. In particular, control cells received a volume of fresh PBS or mQw, equivalent to that of formulations for labelled cells.

Before and immediately after the administration of NPs each well was observed through bright-field microscopy to verify the healthy condition of the cells. The healthy state of cells

was confirmed by morphological inspection and adhesion to the well, while the presence of NPs within them were stated by the presence of small dark spots. At the end of the incubation, cells' state was again verified with bright-field microscopy and then they were harvested from wells.

The addition of 0.5 ml of trypsin was not sufficient to detach the cells and the use of scraper was necessary. Once collected and washed a first time, cells were counted and their viability (Fig. 3.12) was estimated through a standard trypan blue exclusion assay.

A total number of 300 000 cells were collected for MRI analysis for each tested condition.

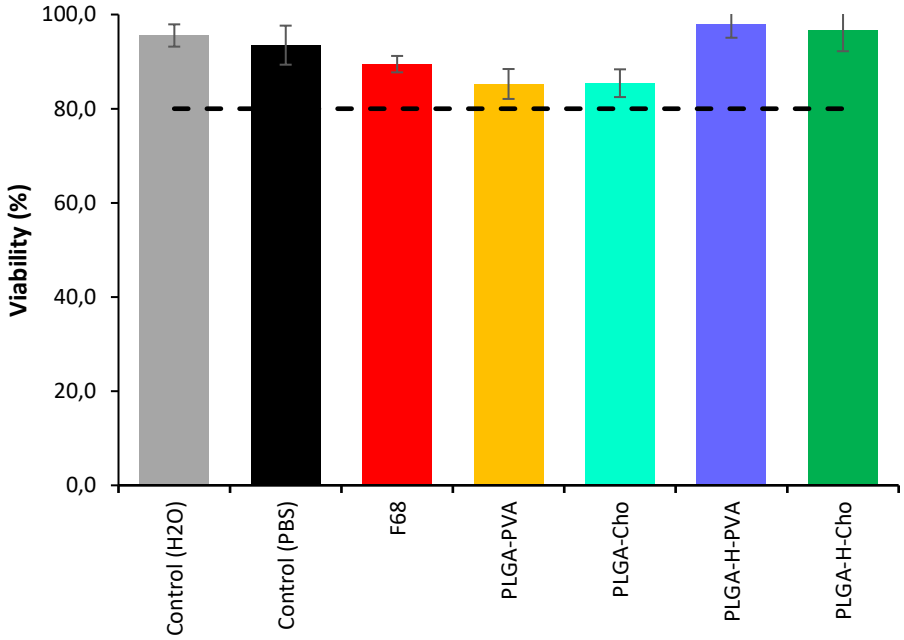


*Figure 3.12: Viability of immortalized BV-2 cells labelled with different formulations performed with trypan blue exclusion assay. Control (H2O) and Control (PBS) are cultures in which the same volume added for each formulation was replaced with mQw or PBS.*

The lowest number of harvested cells is related to the PLGA-NaC formulation. After trypsin inactivation an insoluble aggregate was found in both wells, these aggregates were probably formed by NPs by including a large number of cells. This effect was observed only for this condition, and could be also related to some initial instability of the formulation not observed during the characterization.

For all formulations tested a good cytocompatibility was observed. Both PLGA-H (acid terminated) based NPs showed a cells viability comparable to those found for the control and even slightly better than the internal standard (F68) while cells labelled with NPs with PLGA (methyl terminated) showed a lower compatibility. These data suggest that the acid terminated (PLGA-H) is better tolerated with respect to the methyl terminated (PLGA), while both surfactants NaC and PVA have no relevant impact on cell's viability.

A common problem with cell labelling experiments is the presence of free NPs although different washing steps are performed , if not totally removed these NPs provide a false positive signal in MRI that leads to an overextimation of NPs uptake by cells. Following the administration of labeled cells including free NPs, free NPs will probably be dispersed in the bloodstream and might be redistributed in organs different from cell's target. This false signal, can lead to missread in cell tracking and in the worst case also determine negative biological responses.

For adherent cells, like the BV-2 used in this work, free NPs were easily removed after the incubation. The free NPs are mostly removed with the medium before the first wash, as observed through bright field microscopy. Two more washes ensure the removal of the free NPs.

### 3.4.2 $^{19}$F-MRI

Cell labelling efficiency was performed through $^{19}$F-MRS and $^{19}$F-MRI experiments. Cells were fixed into paraformaldehyde and resuspended into PBS, a pellet of 300 000 cells for each tested condition was positioned into a phantom of agar gel which helps to perform pre-adjustments for MRI (RF power and field shimming) and limits air artefacts on MR images. With PLGA-NaC formulation, the number of collected cells was limited (120 000 and 160 000 for each sample). Together with cells, two samples of PERFECTA emulsion formed with the surfactant F68 were also placed as reference at known concentration ($2x10^{19}$ and $5x10^{19}$ $^{19}$F atoms in 0.15 mL).

As shown in Fig. 3.13, the fluorine signal from each sample (in red) perfectly matched with each sample localized with the standard proton MR image (gray). A clear signal is visible

for cells labelled with PLGA-H-NaC(samples 3 and 6), with a higher intensity than cells labelled with the F68 formulation (samples 1 and 7). While a weak signal was observed for cells labelled with PLGA-H-PV (samples 5 and 11) and mild signal was obtained with PLGA-NaC and PLGA-PVA (samples 10 and 9, respectively).

| | | |
|---|---|---|
| **1** F68 | **5** PLGA-H-PVA | **9** PLGA-PVA |
| **2** PLGA-NaC | **6** PLGA-H-NaC | **10** PLGA-NaC-bis |
| **3** PLGA-H-NaC-bis | **7** F68-bis | **11** PLGA-H-PVA-bis |
| **4** **Ref.** **5x10^19** | **8** **Ref.** **2x10^19** | **12** PLGA-PVA-bis |

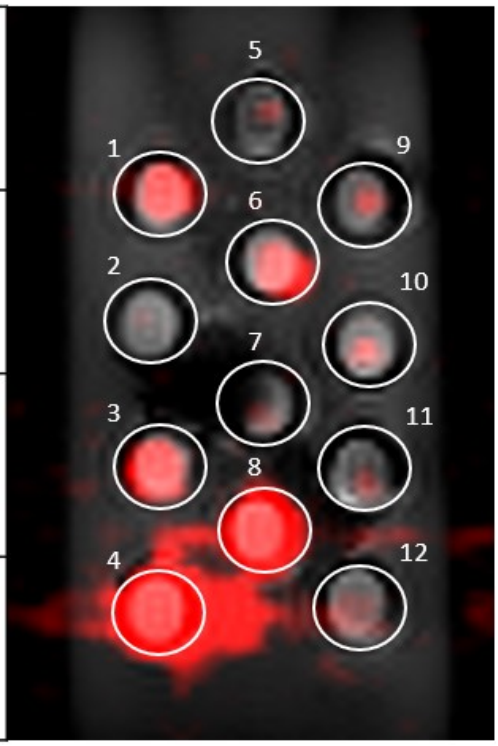


*Figure 3.13: Positions of the cells culture labelled with the different formulations inside the phantom and merged MR images of 19F (red) and 1H (gray). The signal around the sample 4 is due the high intensity obtained for the most concentrated reference (5x10^19 atoms) that is enlarged by increasing the intensity scale.*

For each sample, the signal to noise ratio was measured on 19F-MR images (Tab 3.11). SNR value below 4 are considered as noise and classified as not detectable. The observable signal from cells labelled with PLGA-PVA (sample 12) is due to a contamination introduced by the Ref 5 in position 4 that was too high.

As shown, a high variability between duplicates was found which might be related to the short incubation time (4 hours) and underline the need to further investigate the dynamic of cellular uptake that might be different for each formulation. In addition, the optimal dose for cellular uptake might also differ between formulations.

*Table 3.11: SNR values related to the MRI acquisition on 300 000 BV-2 cells labelled with the different formulations and references. For two formulations, the collected cells were limited to 120 000 (*) and 160 000 cells (**). SNR values below 4 are considered as not detectable (nd).*

| **FORMULATION** | **SNR** | | **UPTAKE (x10$^{12}$ $^{19}$F/CELL)** | |
|---|---|---|---|---|
| **SAMPLES** | 1 | 2 | 1 | 2 |
| **F68** | 14.3 | 4.0 | 5.35 | 1.49 |
| **PLGA-H-PVA** | 3.7 | 4.3 | 3.41 | 2.99 |
| **PLGA-H-NaC** | 13.8 | 17.6 | 5.14 | 6.59 |
| **PLGA-PVA** | 4.5 | nd | 1.69 | nd |
| **PLGA-NaC** | nd* | 3.99** | nd | 1.49 |
| **REF 2 (x10$^{19}$ $^{19}$F)** | 21.2 | | / | |
| **REF 5 (x10$^{19}$ $^{19}$F)** | 63.6 | | / | |

A key advantage of the MRI is the possibility to provide quantitative analysis of fluorine. From the references with a known amount of fluorine, the $^{19}$F/cell was calculated (Tab 3.11) and was found a maximum of 6.59x10$^{12}$ $^{19}$F/cell, with PLGA-H-NaC, and a minimum of 1.49x10$^{12}$ $^{19}$F/cell, with F68 and with PLGA-NaC. These values correspond to a concentration of PERFECTA, inside the 50 µl of cells suspension, respectively of 1.8 mM and 0.4 mM.

Following MRI, $^{19}$F-NMR spectroscopy analysis is ongoing done to further confirm the effective fluorine atoms for each sample. Data was acquired for F68, PLGA-H-NaC and for PLGA-PVA. These data confirm what was observed through MRI, in particular the higher signal detected through $^{19}$F-NMR is related to the PLGA-H-PVA (15.2x10$^{12}$ $^{19}$F/cell) while a lower signal was observed for PLGA-PVA (4.46 x10$^{12}$ $^{19}$F/cell) and F68 (5.58 x10$^{12}$ $^{19}$F/cell) samples.

However, the quantification of the remaining labelled cells through $^{19}$F-NMR is mandatory to provide a clear explanation of the behaviour of these formulations *in vitro*.

# 4 CONCLUSIONS

The aim of this thesis work was the development and optimization of a cell labelling formulation using a superfluorinated molecule as PERFECTA for $^{19}$F-MRI cell tracking. PERFECTA is an excellent candidate for the development of $^{19}$F based contrast agents, but its insolubility in common solvents makes its encapsulation difficult in PLGA based NPs. The dissolution of PERFECTA was made possible through a combination of melting and dissolution in an organic solvent (EtOAc), that allowed us to encapsulate high amounts of PERFECTA in colloidal stable NPs composed by PLGA and stabilized by either PVA or sodium cholate. PERFECTA encapsulation was qualitatively verified by FT-IR analysis as well as the presence of all constituent of the nanoformulation.

The obtained PERFECTA-PLGA loaded NPs demonstrated a good stability in aqueous environment maintaining their size and PDI constant up to 2 weeks, when stored properly at + 4°C. The colloidal stability was reached by adding surfactants: an electrostatic stabilization with sodium cholate by a net negative charge (ζ-potential ~ - 40 mV); a steric stabilization with PVA, which has a low (ζ-potential ~ - 5 mV), not sufficient to stabilize the nanoformulation through electrostatic interaction. In addition, the hydrodynamic diameter differed between both surfactants: 100 nm (PDI = 0.18) with sodium cholate and 195 nm (PDI = 0.10) with PVA. These difference in size had an impact on the cellular uptake.

Furthermore, the 19F-NMR profile of PERFECTA, a single and sharp signal at -73.3 ppm, remained unchanged following formulation process for its encapsulation in both PLGA products. The optimization of formulation protocol permitted to reach an optimal encapsulation efficiency with a mean value of 45% of total fluorine atoms found in the PVA stabilized nanoformulations and between 20% and 30% with the sodium cholate.

These NPs were also tested to verify the cytocompatibility after 4 h of incubation using immortalized microglial murine cell line (BV 2), with optimal results with the PLGA acid terminated formulations, for which the viability was maintained similar to unlabelled cells while it was reduce to 85% with the PLGA methyl terminated. In the cell culture with PLGA-NaC formulation, insoluble aggregates of NPs mixed with cells was found.

From both $^{19}$F-MRI and $^{19}$F-NMR, the highest cellular uptake was found with PLGA-H-NaC formulation. The negative charge of these NPs could have a main role in the interaction with the cell membrane while their low dimensions could help in their uptake. Considering also the signal acquired for cells labelled with PLGA-NaC, which is comparable to other formulations but with half of the labelled cells, the superficial charge seems to be the key factor that drive the uptake.

The NPs developed during this thesis work demonstrate to be good probes for labelling phagocytic cells with a sufficient high concentration of fluorine atoms for MRI. However, due to a better cytocompatibility and due to the uptake efficiency PLGA-H-NaC was selected for future investigation aimed to understand the uptake pathways. PLGA-NaC could be a good candidate but before further application it is necessary to understand what led to the formation of the aggregation. A stability study in DMEM (with and without serum) is ongoing to verify the interactions of the NPs with the serum proteins.

Data obtained from 19F-NMR and from the stability study in culture medium will help to better understand the cell uptake of 19F-NPs and if the uptake is correlated to particular interaction with the serum proteins.

By defining the internalization pathways of these NPs by cells, we might be able to further optimize cell labelling and consequently improve MRI sensitivity to detect small number of cells. While the addition of a PLGA functionalized with a fluorophore could enable the visualization of the labelled cells with confocal microscopy or FACS, to fully characterize cell's function and the endocytic mechanism.

A future perspective of this work is the use of these NPs for labelling non phagocytic cells such as T-cells and stem cells, for which it is quite challenging to find effective labelling agents.

In the first *in vitro* experiment the cytocompatibility of PLGA-H-PVA, PLGA-H-NaC, PLGA-PVA and PLGA-NaC was investigate.

Except for PLGA-PVA, that lost its colloidal stability at 48 h, all other formulations were stable until the incubation as observable in Fig. 0.1.

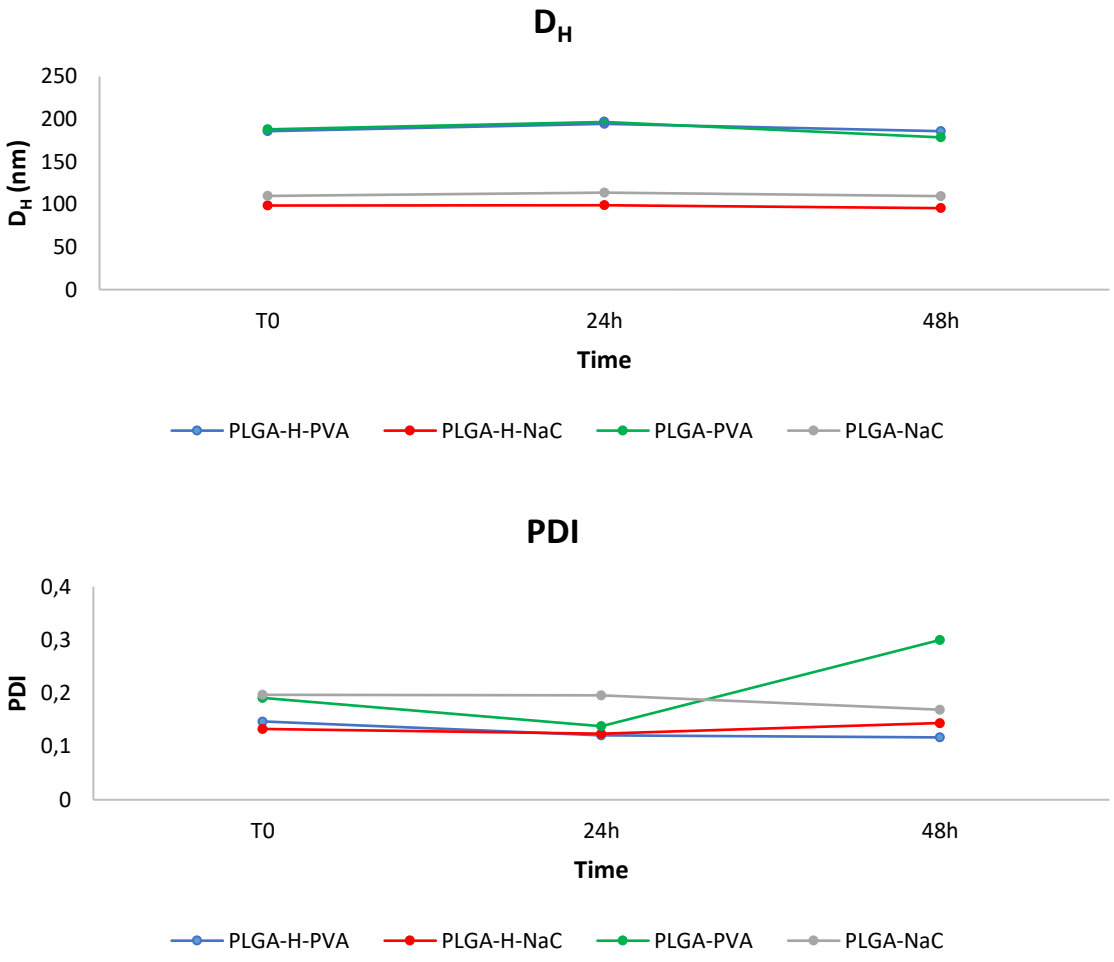


*Figure 0.1:Hydrodynamic diameters of the four formulations (upper) and PDI measurements (lower) over three days.*

The PLGA-PVA instability is related to the formation of aggregates, visible in the size distribution function in Fig 0.2.

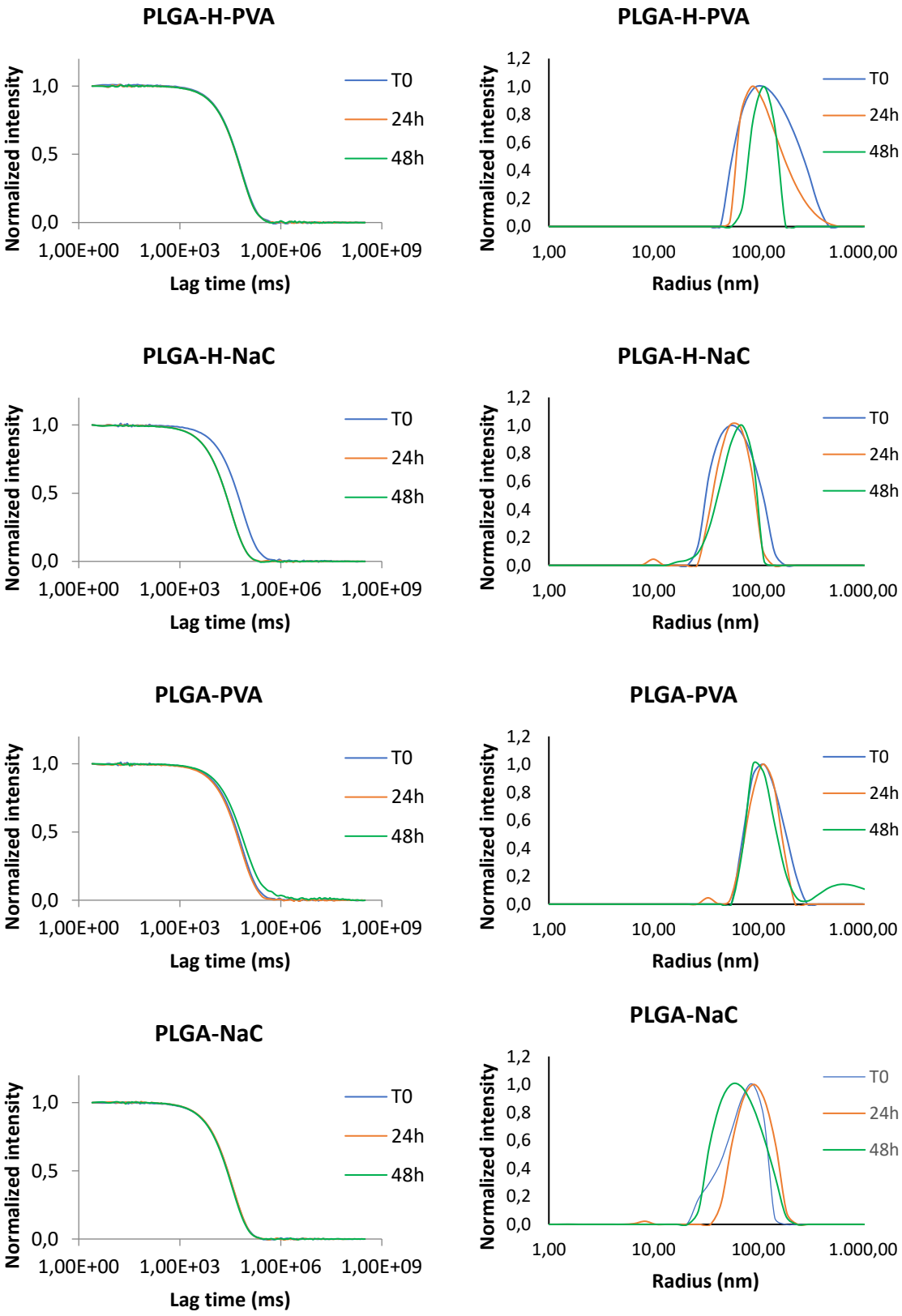


*Figure 0.2: Correlation function (left column) and unweighted size distribution (right column) for nanoformulations administered to cells for the first in vitro experiment at three different time points and 90°.*

19F-NMR spectroscopy on these formulations permits to find the 19F concentration reported in Tab. 0.1

*Table 0.1:* Fluorine content and encapsulation efficiency measured through 19F-NMR of the nanoformulation proposed. Theorical 19F atoms are the number of fluorine atoms added at the beginning of the formulation procedure and equivalent to 20 mg of PERFECTA.

| FORMULATION | THEORICAL $^{19}F$ ATOMS ($^{19}F$/ml) | QUANTIFIED $^{19}F$ ATOMS ($^{19}F$/ml) | ENCAPSULATION (%) |
|---|---|---|---|
| **PLGA-H-PVA** | $4.30 \times 10^{20}$ | $1.49 \times 10^{20}$ | 34.64 % |
| **PLGA-H-NaC** | $4.30 \times 10^{20}$ | $1.07 \times 10^{20}$ | 24.88 % |
| **PLGA-PVA** | $4.30 \times 10^{20}$ | $0.76 \times 10^{20}$ | 17.67 % |
| **PLGA-NaC** | $4.30 \times 10^{20}$ | $1.08 \times 10^{20}$ | 25.11 % |

A lower initial concentration of PERFECTA was chosen to formulate these NPs. Starting from less compound a lower final concentration was found, however these values permits to label $1 \times 10^6$ cells with $1 \times 10^{14}$ $^{19}F$/cell.

The low stability of PLGA-PVA NPs had effects also on encapsulation efficiency, resulting in a very low encapsulation.

To investigate the effects of these NPs, a viability study was done. Cells were incubated with NPs for 4 h and a trypan blue exclusion method was used to estimate the cytotoxicity. Results obtained from viability assay is showed in Fig. 0.3.

The low viability of cells labelled with PLGA-PVA are related to instability in the formulation. While for all other conditions no evident cytotoxicity effects were observed.

Confirmed the overall good compatibility of these formulation, 200 000 cells were collected and investigated through MRI to verify the labelling. In Fig. 0.4 the MRI acquisition is showed while results obtained are reported in Tab 0.2 within the $^{19}F$ quantification from SNR and $^{19}F$-NMR.

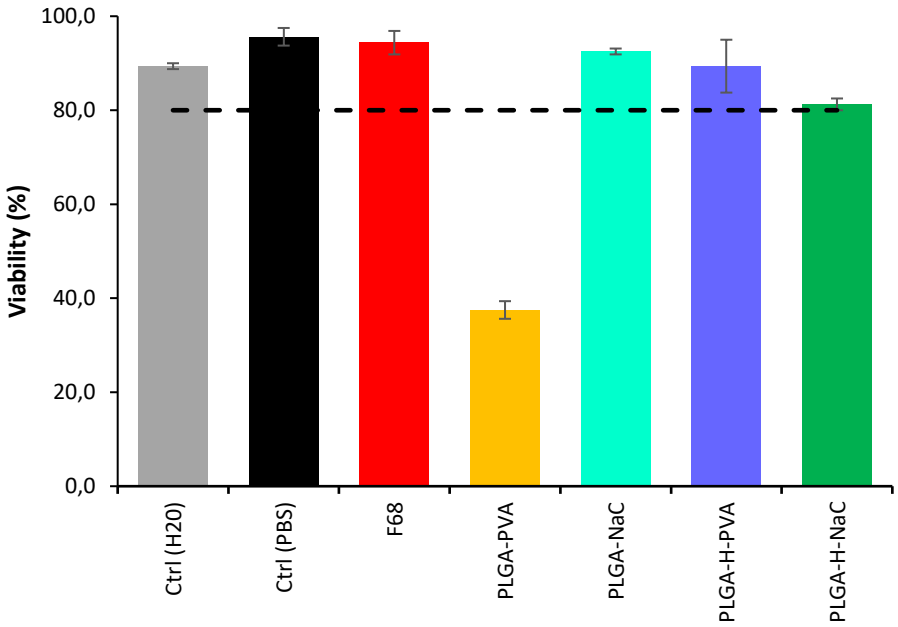


*Figure 0.3: Viability of immortalized BV-2 cells labelled with different formulations performed with trypan blue exclusion assay. Control (H2O) and Control (PBS) are cultures in which the same volume added for each formulation was replaced with mQw or PBS.*

| | | |
|---|---|---|
| **1** PLGA-PVA | **5** PLGA-H-PVA | / |
| **2** PLGA-NaC | **6** PLGA-H-NaC | **10** PLGA-NaC-bis |
| **3** PLGA-H-NaC-bis | **7** PLGA-PVA-bis | **11** PLGA-H-PVA-bis |
| **4** **Ref.** **5x10^19** | **8** **Ref.** **2x10^19** | / |

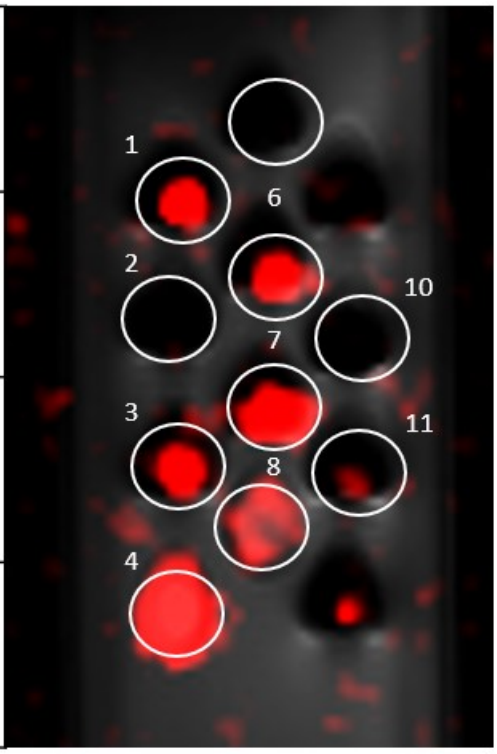


*Figure 0.4:* Positions of the cells culture labelled with the different formulations inside the phantom and merged MR images of 19F (red) and 1H (gray).

MRI signal related to PLGA-PVA (samples 1 and 7) are provided by free NPs due to cell lysis.

*Table 0.2:* SNR values related to the MRI acquisition on 200 000 BV-2 cells labelled with the different formulations and references. SNR values below 4 are considered as not detectable (nd).

| **FORMULATION** | | **SNR** | **UPTAKE (x10$^{13}$ $^{19}$F/CELL)** | |
|---|---|---|---|---|
| | Sample | | MRI | NMR |
| **PLGA-H-PVA** | 1 | nd | nd | 0.04 |
| | 2 | 4.7 | 2.56 | 0.07 |
| **PLGA-H-NaC** | 1 | 15.5 | 8.44 | 1.76 |
| | 2 | 16.0 | 8.71 | 1.76 |
| **PLGA-PVA** | 1 | 16.8 | 9.15 | 0.54 |
| | 2 | 49.2 | 26.8 | 0.98 |
| **PLGA-NaC** | 1 | nd | nd | 0.08 |
| | 2 | nd | nd | 0.05 |
| **REF 2 (x10$^{19}$ $^{19}$F)** | | 5.8 | / | |
| **REF 5 (x10$^{19}$ $^{19}$F)** | | 14.9 | / | |

This first experiment was useful to investigate the viability and labelling efficiency of the nanoformulations. All formulations were well tolerated from BV 2 cells resulting in a viability comparable to those found for the controls, except the PLGA-PVA formulation for which a high cytotoxicity was observed. This effect however could be related to instability in the formulation that lead to the cell lysis, in fact during bright-field microscopy observation NPs aggregates were found in both wells.

PLGA-H-NaC labelled cells (positions e and 6) were the only with an appreciable signal while PLGA-H-PVA labelled cells (position 11) provide a mild signal. $^{19}$F-NMR spectroscopy was done to confirm data obtained. $^{19}$F-NMR should have provided a better signal compared to $^{19}$F-MRI due to a greater sensibility, founding a lower signal has been hypothesized a loose of $^{19}$F in MRI references and also part of the possible loss of cells during samples transfer between MRI and NMR. Despite the similar SNR values, for cells

labelled with PLGA-H-NaC were found a total of $1.7x10^{19}$ $^{19}F$ ($^{19}F$-MRI) and $3.5x10^{18}$ $^{19}F$ ($^{19}F$-NMR), respectively 3 times and 10 times lower than REF 5.

Due to the low signal found, we decided to increase the number of cells to 300 000 for the second *in vitro* experiment.

[1] M. J. Lysaght and J. Crager, “Origins,” *Tissue Enginnering Part A*, vol. 15, no. 7, pp. 1449–1450, 2009, [Online]. Available: https://www.liebertpub.com/doi/full/10.1089/ten.tea.2007.0412?url_ver=Z39.88-2003&rfr_id=ori:rid:crossref.org&rfr_dat=cr_pub%3Dpubmed.

[2] K. T. Ip, *Regenerative Medicine*, Third Edit. Elsevier Inc., 2012.

[3] E. H. Ntege, H. Sunami, and Y. Shimizu, “Advances in regenerative therapy: A review of the literature and future directions,” *Regen. Ther.*, vol. 14, pp. 136–153, Jun. 2020, doi: 10.1016/j.reth.2020.01.004.

[4] R. Mahla, “Adipose Stem Cells Applications in Regenerative Medicine,” vol. 3, no. 4, pp. 151–157, 2015, doi: 10.1155/2016/6940283.

[5] J. Wang *et al.*, “Characterization and therapeutic applications of mesenchymal stem cells for regenerative medicine,” *Tissue Cell*, vol. 64, no. 126, p. 101330, 2020, doi: 10.1016/j.tice.2020.101330.

[6] A. I. Caplan, “Mesenchymal Stem Cells,” *Essentials Stem Cell Biol.*, pp. 243–248, 2009, doi: 10.1016/B978-0-12-374729-7.00029-9.

[7] J. M. Gimble, A. J. Katz, and B. A. Bunnell, “Adipose-derived stem cells for regenerative medicine,” *Circ. Res.*, vol. 100, no. 9, pp. 1249–1260, 2007, doi: 10.1161/01.RES.0000265074.83288.09.

[8] A. Klimczak and U. Kozlowska, “Mesenchymal stromal cells and tissue-specific progenitor cells: Their role in tissue homeostasis,” *Stem Cells Int.*, vol. 2016, 2016, doi: 10.1155/2016/4285215.

[9] H. W. Lee, P. Gangadaran, S. Kalimuthu, and B. C. Ahn, “Advances in Molecular Imaging Strategies for in Vivo Tracking of Immune Cells,” *Biomed Res. Int.*, vol. 2016, no. Dc, 2016, doi: 10.1155/2016/1946585.

[10] C. H. June and M. Sadelain, “Chimeric antigen receptor therapy,” *N. Engl. J. Med.*, vol. 379, no. 1, pp. 64–73, 2018, doi: 10.1056/NEJMra1706169.

[11] S. A. Rosenberg and N. P. Restifo, “Adoptive cell transfer as personalized

immunotherapy for human cancer," *Science (80-. ).*, vol. 348, no. 6230, pp. 62–68, 2015, doi: 10.1126/science.aaa4967.

[12] FDA, "Content and Review of Chemistry, Manufacturing, and Control (CMC) Information for Human Somatic Cell," *Guid. FDA Rev. Spons.*, no. April, 2008.

[13] L. Accomasso, C. Gallina, V. Turinetto, and C. Giachino, "Stem cell tracking with nanoparticles for regenerative medicine purposes: An overview," *Stem Cells Int.*, vol. 2016, no. d, 2016, doi: 10.1155/2016/7920358.

[14] C. Villa *et al.*, "Stem cell tracking by nanotechnologies," *Int. J. Mol. Sci.*, vol. 11, no. 3, pp. 1070–1081, 2010, doi: 10.3390/ijms11031070.

[15] R. T. Sadikot and T. S. Blackwell, "Bioluminescence imaging," *Proc. Am. Thorac. Soc.*, vol. 2, no. 6, pp. 537–540, 2005, doi: 10.1513/pats.200507-067DS.

[16] C. H. Contag and M. H. Bachmann, "Advances in In Vivo Bioluminescence Imaging of Gene Expression," *Annu. Rev. Biomed. Eng.*, vol. 4, no. 1, pp. 235–260, 2002, doi: 10.1146/annurev.bioeng.4.111901.093336.

[17] S. Hu *et al.*, "Bioluminescence imaging of exogenous & endogenous cysteine in vivo with a highly selective probe," *Bioorganic Med. Chem. Lett.*, vol. 30, no. 6, p. 126968, 2020, doi: 10.1016/j.bmcl.2020.126968.

[18] T. Schomann, L. Mezzanotte, J. C. M. J. de Groot, C. W. G. M. Löwik, J. H. M. Frijns, and M. A. Huisman, "Imaging Bioluminescent Exogenous Stem Cells in the Intact Guinea Pig Cochlea," *Anat. Rec.*, vol. 303, no. 3, pp. 427–440, 2020, doi: 10.1002/ar.24068.

[19] J. V. Frangioni, "In vivo near-infrared fluorescence imaging," *Curr. Opin. Chem. Biol.*, vol. 7, no. 5, pp. 626–634, 2003, doi: 10.1016/j.cbpa.2003.08.007.

[20] W. Lim, B. Kim, G. Jo, D. H. Yang, M. H. Park, and H. Hyun, "Bioluminescence and near-infrared fluorescence imaging for detection of metastatic bone tumors," *Lasers Med. Sci.*, vol. 35, no. 1, pp. 115–120, 2020, doi: 10.1007/s10103-019-02801-9.

[21] V. Ntziachristos, "Going deeper than microscopy: The optical imaging frontier in

biology," *Nat. Methods*, vol. 7, no. 8, pp. 603–614, 2010, doi: 10.1038/nmeth.1483.

[22] P. Beard, "Biomedical photoacoustic imaging," *Interface Focus*, vol. 1, no. 4, pp. 602–631, 2011, doi: 10.1098/rsfs.2011.0028.

[23] M. Xu and L. V. Wang, "Photoacoustic imaging in biomedicine," *Rev. Sci. Instrum.*, vol. 77, no. 4, 2006, doi: 10.1063/1.2195024.

[24] J. Le Floc'h *et al.*, "Transcranial Photoacoustic Detection of Blood-Brain Barrier Disruption Following Focused Ultrasound-Mediated Nanoparticle Delivery," *Mol. Imaging Biol.*, vol. 22, no. 2, pp. 324–334, 2020, doi: 10.1007/s11307-019-01397-4.

[25] A. Berger, "Positron emission tomography," *Br. Med. J.*, vol. 326, no. 7404, p. 1449, 2003, doi: 10.1136/bmj.326.7404.1449.

[26] S. Kitson, V. Cuccurullo, A. Ciarmiello, D. Salvo, and L. Mansi, "Clinical Applications of Positron Emission Tomography (PET) Imaging in Medicine: Oncology, Brain Diseases and Cardiology," *Curr. Radiopharm.*, vol. 2, no. 4, pp. 224–253, 2012, doi: 10.2174/1874471010902040224.

[27] B. R. Smith and S. S. Gambhir, "Nanomaterials for in Vivo Imaging," *Chem. Rev.*, vol. 117, no. 3, pp. 901–986, 2017, doi: 10.1021/acs.chemrev.6b00073.

[28] J. H. F. Rudd *et al.*, "Atherosclerosis inflammation imaging with 18F-FDG PET: Carotid, iliac, and femoral uptake reproducibility, quantification methods, and recommendations," *J. Nucl. Med.*, vol. 49, no. 6, pp. 871–878, 2008, doi: 10.2967/jnumed.107.050294.

[29] R. A. Pooley, "AAPM/RSNA physics tutorial for residents: fundamental physics of MR imaging.," *Radiographics*, vol. 25, no. 4, pp. 1087–1099, 2005, doi: 10.1148/rg.254055027.

[30] J. C. P. Heggie, "Magnetic Resonance Imaging: Principles, Methods and Techniques by Perry Sprawls," *Australas. Phys. Eng. Sci. Med.*, vol. 24, no. 1, p. 57, 2001, doi: 10.1007/BF03178286.

[31] R. Health and U. S. Food, "Initiative to Reduce Unnecessary Radiation Exposure from Medical Imaging," *Cent. Devices Radiol. Heal.*, no. February, 2010.

[32] C. Burtea, S. Laurent, L. Vander Elst, and R. N. Muller, “Contrast Agents : Magnetic Resonance,” 2008.

[33] A. A. Gilad *et al.*, “MR tracking of transplanted cells with ‘positive contrast’ using manganese oxide nanoparticles,” *Magn. Reson. Med.*, vol. 60, no. 1, pp. 1–7, 2008, doi: 10.1002/mrm.21622.

[34] S. Zhang, M. Merritt, D. E. Woessner, R. E. Lenkinski, and A. D. Sherry, “PARACEST Agents: Modulating MRI Contrast via Water Proton Exchange,” *Acc. Chem. Res.*, vol. 36, no. 10, pp. 783–790, 2003, doi: 10.1021/ar020228m.

[35] I. Hancu, W. T. Dixon, M. Woods, E. Vinogradov, A. D. Sherry, and R. E. Lenkinski, “CEST and PARACEST MR contrast agents,” *Acta radiol.*, vol. 51, no. 8, pp. 910–923, 2010, doi: 10.3109/02841851.2010.502126.

[36] H. Shokrollahi, “Contrast agents for MRI,” *Mater. Sci. Eng. C*, vol. 33, no. 8, pp. 4485–4497, 2013, doi: 10.1016/j.msec.2013.07.012.

[37] Y. Xiao, R. Paudel, J. U. N. Liu, C. Ma, Z. Zhang, and S. Zhou, “MRI contrast agents : Classification and application ( Review ),” pp. 1319–1326, 2016, doi: 10.3892/ijmm.2016.2744.

[38] P. Caravan, J. J. Ellison, T. J. Mcmurry, and R. B. Lauffer, “Gadolinium ( III ) Chelates as MRI Contrast Agents : Structure , Dynamics , and Applications,” no. Iii, 1999, doi: 10.1021/cr980440x.

[39] A. Spinazzi, “MRI Safety Update 2008: Part 1, MRI Contrast Agents and Nephrogenic Systemic Fibrosis,” no. October, pp. 1129–1139, 2008, doi: 10.2214/AJR.08.1038.1.

[40] European Medicines Agency, “EMA’s final opinion confirms restrictions on use of linear gadolinium agents in body scans Recommendations conclude EMA’s scientific review of gadolinium deposition,” *Eur. Med. Agency*, vol. November, no. 23rd, p. Document Reference: EMA/625317/2017 EMA’s, 2017, doi: 10.1016/j.rse.2010.12.006.

[41] U. S. F. and D. Administration, “FDA warns that gadolinium-based contrast agents (GBCAs) are retained in the body; requires new class warnings.,” *U.S. Food Drug*

*Adm. Drug Saf. Commun.*, vol. December, no. 19th, p. Document Reference: 109825, 2017, [Online]. Available: www.fda.gov/Drugs/DrugSafety/ucm589213.htm.

[42] A. C. Silva and N. A. Bock, "Manganese-enhanced MRI: An exceptional tool in translational neuroimaging," *Schizophr. Bull.*, vol. 34, no. 4, pp. 595–604, 2008, doi: 10.1093/schbul/sbn056.

[43] G. Saar and A. P. Koretsky, "Manganese enhanced MRI for use in studying neurodegenerative diseases," *Front. Neural Circuits*, vol. 12, no. January, pp. 1–11, 2019, doi: 10.3389/fncir.2018.00114.

[44] M. Thuen *et al.*, "Manganese-Enhanced MRI of the Rat Visual Pathway : Acute Neural Toxicity , Contrast Enhancement , Axon Resolution , Axonal Transport , and Clearance of Mn 2 ⁺," vol. 865, pp. 855–865, 2008, doi: 10.1002/jmri.21504.

[45] H. Bin Na, I. C. Song, and T. Hyeon, "Inorganic nanoparticles for MRI contrast agents," *Adv. Mater.*, vol. 21, no. 21, pp. 2133–2148, 2009, doi: 10.1002/adma.200802366.

[46] B. Xia *et al.*, "Activatable Cell-Penetrating Peptide Conjugated Polymeric Nanoparticles with Gd-Chelation and Aggregation-Induced Emission for Bimodal MR and Fluorescence Imaging of Tumors," *ACS Appl. Bio Mater.*, vol. 3, no. 3, pp. 1394–1405, 2020, doi: 10.1021/acsabm.9b01049.

[47] P. Šimečková *et al.*, "Gadolinium labelled nanoliposomes as the platform for MRI theranostics: in vitro safety study in liver cells and macrophages," *Sci. Rep.*, vol. 10, no. 1, pp. 1–13, 2020, doi: 10.1038/s41598-020-60284-z.

[48] J. Perrin *et al.*, "Cell Tracking in Cancer Immunotherapy," *Front. Med.*, vol. 7, no. February, pp. 1–16, 2020, doi: 10.3389/fmed.2020.00034.

[49] J. W. M. Bulte and D. L. Kraitchman, "Iron oxide MR contrast agents for molecular and cellular imaging," pp. 484–499, 2004, doi: 10.1002/nbm.924.

[50] N. J. Serkova, "Nanoparticle-based magnetic resonance imaging on tumor-associated macrophages and inflammation," *Front. Immunol.*, vol. 8, no. MAY, pp. 1–7, 2017, doi: 10.3389/fimmu.2017.00590.

[51] Jasmin, G. T. Souza, R. Andrade Louzada, P. H. Rosado-de-Castro, R. Mendez-Otero, and A. C. C. Carvalho, “Tracking stem cells with superparamagnetic iron oxide nanoparticles: perspectives and considerations,” *Int. J. Nanomedicine*, vol. Volume 12, pp. 779–793, Jan. 2017, doi: 10.2147/IJN.S126530.

[52] Y.-X. J. Wang, “Current status of superparamagnetic iron oxide contrast agents for liver magnetic resonance imaging,” *Magma Magn. Reson. Mater. Physics, Biol. Med.*, vol. 11, no. 1, pp. 65–67, 2000, doi: 10.1007/bf02678498.

[53] Y. C. Ou, X. Wen, and R. Bardhan, “Cancer Immunoimaging with Smart Nanoparticles,” *Trends Biotechnol.*, vol. 38, no. 4, pp. 388–403, 2020, doi: 10.1016/j.tibtech.2019.11.001.

[54] S. Rizzo *et al.*, “In vitro labelling and detection of mesenchymal stromal cells: a comparison between magnetic resonance imaging of iron-labelled cells and magnetic resonance spectroscopy of fluorine-labelled cells,” *Eur. Radiol. Exp.*, vol. 1, no. 1, pp. 1–7, 2017, doi: 10.1186/s41747-017-0010-9.

[55] N. Singh, G. J. S. Jenkins, R. Asadi, and S. H. Doak, “Potential toxicity of superparamagnetic iron oxide nanoparticles (SPION),” *Nano Rev.*, vol. 1, no. 1, p. 5358, 2010, doi: 10.3402/nano.v1i0.5358.

[56] I. Tirotta *et al.*, “19 F Magnetic Resonance Imaging (MRI): From Design of Materials to Clinical Applications,” *Chem. Rev.*, vol. 115, no. 2, pp. 1106–1129, Jan. 2015, doi: 10.1021/cr500286d.

[57] M. Srinivas, A. Heerschap, E. T. Ahrens, C. G. Figdor, and I. J. M. de Vries, “19F MRI for quantitative in vivo cell tracking,” *Trends Biotechnol.*, vol. 28, no. 7, pp. 363–370, 2010, doi: 10.1016/j.tibtech.2010.04.002.

[58] C. Craik, “基因的改变NIH Public Access,” *Bone*, vol. 23, no. 1, pp. 1–7, 2008, doi: 10.1038/jid.2014.371.

[59] E. T. Ahrens, R. Flores, H. Xu, and P. A. Morel, “In vivo imaging platform for tracking immunotherapeutic cells,” *Nat. Biotechnol.*, vol. 23, no. 8, pp. 983–987, 2005, doi: 10.1038/nbt1121.

[60] J. Ruiz-Cabello, B. P. Barnett, P. A. Bottomley, and J. W. M. Bulte, “Fluorine (19

F) MRS and MRI in biomedicine," *Bone*, vol. 23, no. 1, pp. 1–7, 2008, doi: 10.1038/jid.2014.371.

[61] J. G. Riess and J. G. Riess, "Oxygen carriers ('blood substitutes') - Raison d'etre, chemistry, and some physiology," *Chem. Rev.*, vol. 101, no. 9, pp. 2797–2919, 2001, doi: 10.1021/cr970143c.

[62] C. Constantinides *et al.*, "Temporal accumulation and localization of isoflurane in the C57BL/6 mouse and assessment of its potential contamination in 19F MRI with perfluoro-crown-ether-labeled cardiac progenitor cells at 9.4 Tesla," *J. Magn. Reson. Imaging*, vol. 45, no. 6, pp. 1659–1667, 2017, doi: 10.1002/jmri.25564.

[63] D. K. Kadayakkara, K. Damodaran, T. K. Hitchens, J. W. M. Bulte, and E. T. Ahrens, "19F spin-lattice relaxation of perfluoropolyethers: Dependence on temperature and magnetic field strength (7.0-14.1 T)," *J. Magn. Reson.*, vol. 242, pp. 18–22, 2014, doi: 10.1016/j.jmr.2014.01.014.

[64] M. Srinivas, M. S. Turner, J. M. Janjic, P. A. Morel, D. H. Laidlaw, and E. T. Ahrens, "In vivo cytometry of antigen-specific T cells using 19F MRI," *Magn. Reson. Med.*, vol. 62, no. 3, pp. 747–753, 2009, doi: 10.1002/mrm.22063.

[65] P. Boehm-Sturm, L. Mengler, S. Wecker, M. Hoehn, and T. Kallur, "In Vivo tracking of human neural stem cells with 19F magnetic resonance imaging," *PLoS One*, vol. 6, no. 12, 2011, doi: 10.1371/journal.pone.0029040.

[66] B. M. Helfer *et al.*, "Functional assessment of human dendritic cells labeled for in vivo 19F magnetic resonance imaging cell tracking," *Cytotherapy*, vol. 12, no. 2, pp. 238–250, 2010, doi: 10.3109/14653240903446902.

[67] H. Vu-Quang *et al.*, "Chitosan-coated poly(lactic-co-glycolic acid) perfluorooctyl bromide nanoparticles for cell labeling in 19F magnetic resonance imaging," *Carbohydr. Polym.*, vol. 136, pp. 936–944, 2016, doi: 10.1016/j.carbpol.2015.09.076.

[68] M. Srinivas, P. Boehm-Sturm, C. G. Figdor, I. J. de Vries, and M. Hoehn, "Labeling cells for in vivo tracking using 19F MRI," *Biomaterials*, vol. 33, no. 34, pp. 8830–8840, 2012, doi: 10.1016/j.biomaterials.2012.08.048.

[69] O. Diou *et al.*, “Long-circulating perfluorooctyl bromide nanocapsules for tumor imaging by 19FMRI,” *Biomaterials*, vol. 33, no. 22, pp. 5593–5602, 2012, doi: 10.1016/j.biomaterials.2012.04.037.

[70] C. Chirizzi *et al.*, “Multispectral MRI with dual fluorinated probes to track mononuclear cell activity in mice,” *Radiology*, vol. 291, no. 2, pp. 351–357, 2019, doi: 10.1148/radiol.2019181073.

[71] I. Tirotta *et al.*, “A superfluorinated molecular probe for highly sensitive in vivo 19F-MRI,” *J. Am. Chem. Soc.*, vol. 136, no. 24, pp. 8524–8527, 2014, doi: 10.1021/ja503270n.

[72] O. Koshkina *et al.*, “Nanoparticles for ‘two color’ 19F magnetic resonance imaging: Towards combined imaging of biodistribution and degradation,” *J. Colloid Interface Sci.*, vol. 565, pp. 278–287, 2020, doi: 10.1016/j.jcis.2019.12.083.

[73] F. Chapelin, C. M. Capitini, and E. T. Ahrens, “Fluorine-19 MRI for detection and quantification of immune cell therapy for cancer,” *J. Immunother. Cancer*, vol. 6, no. 1, pp. 1–11, 2018, doi: 10.1186/s40425-018-0416-9.

[74] E. Swider *et al.*, “Design of triphasic poly(lactic-co-glycolic acid) nanoparticles containing a perfluorocarbon phase for biomedical applications,” *RSC Adv.*, vol. 8, no. 12, pp. 6460–6470, 2018, doi: 10.1039/c7ra13062g.

[75] J. M. Janjic and E. T. Ahrens, “Fluorine-containing nanoemulsions for MRI cell tracking,” *Nanomedicine*, vol. 1, pp. 492–501, 2009, doi: 10.1002/wnan.035.

[76] J. Rejman, V. Oberle, I. S. Zuhorn, and D. Hoekstra, “Size-dependent internalization of particles via the pathways of clathrin-and caveolae-mediated endocytosis,” *Biochem. J.*, vol. 377, no. 1, pp. 159–169, 2004, doi: 10.1042/BJ20031253.

[77] G. M. Lanza *et al.*, “A Novel Site-Targeted Ultrasonic Contrast Agent With Broad Biomedical Application,” *Circulation*, vol. 94, no. 12, pp. 3334–3340, 1996, doi: https://doi.org/10.1161/01.CIR.94.12.3334.

[78] P. Taylor, “Ostwald ripening in emulsions,” *Adv. Colloid Interface Sci.*, vol. 75, no. 2, pp. 107–163, 1998, doi: 10.1016/S0001-8686(98)00035-9.

[79] S. Verma, S. Kumar, R. Gokhale, and D. J. Burgess, “Physical stability of nanosuspensions: Investigation of the role of stabilizers on Ostwald ripening,” *Int. J. Pharm.*, vol. 406, no. 1–2, pp. 145–152, 2011, doi: 10.1016/j.ijpharm.2010.12.027.

[80] J. M. Janjic, M. Srinivas, D. K. K. Kadayakkara, and E. T. Ahrens, “Self-delivering nanoemulsions for dual fluorine-19 MRI and fluorescence detection,” *J. Am. Chem. Soc.*, vol. 130, no. 9, pp. 2832–2841, 2008, doi: 10.1021/ja077388j.

[81] M. Hirenkumar and S. Steven, “Poly Lactic-co-Glycolic Acid (PLGA) as Biodegradable Controlled Drug Delivery Carrier,” *Polymers (Basel).*, vol. 3, no. 3, pp. 1–19, 2012, doi: 10.3390/polym3031377.Poly.

[82] M. Srinivas, L. J. Cruz, F. Bonetto, A. Heerschap, C. G. Figdor, and I. J. M. de Vries, “Customizable, multi-functional fluorocarbon nanoparticles for quantitative in vivo imaging using 19F MRI and optical imaging,” *Biomaterials*, vol. 31, no. 27, pp. 7070–7077, 2010, doi: 10.1016/j.biomaterials.2010.05.069.

[83] M. Srinivas *et al.*, “PLGA-encapsulated perfluorocarbon nanoparticles for simultaneous visualization of distinct cell populations by 19F MRI,” *Nanomedicine*, vol. 10, no. 15, pp. 2339–2348, 2015, doi: 10.2217/nnm.15.76.

[84] S. Rezvantalab *et al.*, “PLGA-based nanoparticles in cancer treatment,” *Front. Pharmacol.*, vol. 9, no. NOV, pp. 1–19, 2018, doi: 10.3389/fphar.2018.01260.

[85] A. H. J. Staal *et al.*, “In vivo clearance of 19F MRI imaging nanocarriers is strongly influenced by nanoparticle ultrastructure,” *Biomaterials*, 2020, doi: 10.1016/j.jns.2019.116544.

[86] E. Swider, O. Koshkina, J. Tel, L. J. Cruz, I. J. M. de Vries, and M. Srinivas, “Customizing poly(lactic-co-glycolic acid) particles for biomedical applications,” *Acta Biomater.*, vol. 73, pp. 38–51, 2018, doi: 10.1016/j.actbio.2018.04.006.

[87] P. Foroozandeh and A. A. Aziz, “Insight into Cellular Uptake and Intracellular Trafficking of Nanoparticles,” *Nanoscale Res. Lett.*, vol. 13, 2018, doi: 10.1186/s11671-018-2728-6.

[88] A. E. Nel *et al.*, “Understanding biophysicochemical interactions at the nano-bio interface,” *Nat. Mater.*, vol. 8, no. 7, pp. 543–557, 2009, doi: 10.1038/nmat2442.

[89] S. Bhattacharjee, “DLS and zeta potential - What they are and what they are not?,” *J. Control. Release*, vol. 235, pp. 337–351, 2016, doi: 10.1016/j.jconrel.2016.06.017.

[90] J. Stetefeld, S. A. McKenna, and T. R. Patel, “Dynamic light scattering: a practical guide and applications in biomedical sciences,” *Biophys. Rev.*, vol. 8, no. 4, pp. 409–427, 2016, doi: 10.1007/s12551-016-0218-6.

[91] A. G. Mailer, P. S. Clegg, and P. N. Pusey, “Particle sizing by dynamic light scattering: Non-linear cumulant analysis,” *J. Phys. Condens. Matter*, vol. 27, no. 14, 2015, doi: 10.1088/0953-8984/27/14/145102.

[92] P. Hole *et al.*, “Interlaboratory comparison of size measurements on nanoparticles using nanoparticle tracking analysis (NTA),” *J. Nanoparticle Res.*, vol. 15, no. 12, 2013, doi: 10.1007/s11051-013-2101-8.

[93] V. Filipe, A. Hawe, and W. Jiskoot, “Critical evaluation of nanoparticle tracking analysis (NTA) by NanoSight for the measurement of nanoparticles and protein aggregates,” *Pharm. Res.*, vol. 27, no. 5, pp. 796–810, 2010, doi: 10.1007/s11095-010-0073-2.

[94] L. D. Thanh and R. Sprik, “Zeta Potential Measurement Using Streaming Potential in Porous Media,” *J. Sci. Nat. Sci. Technol.*, vol. 31, no. 4, pp. 56–65, 2015.

[95] J. L. Walter, *The Infrared Spectra of Complex Molecules*, vol. 59, no. 4. 1982.

[96] J. Coates, “Interpretation of Infrared Spectra, A Practical Approach,” *Encycl. Anal. Chem.*, pp. 10815–10837, 2000, doi: 10.1097/00010694-197107000-00005.

[97] P. Y. Bruice, “The Intensity of Absorption Bands,” in *Organic Chemistry*, Pearson Education, 2016.

[98] J. B. Lambert, E. P. Mazzola, and L. N. Holland, *Nuclear Magnetic Resonance Spectroscopy: An Introduction to Principles, Applications, and Experimental Methods*. Pearson Education, 2004.

[99] and S. W. Jonathan Clayden, Nick Greeves, “Quantitative NMR Spectroscopy.docx Quantitative NMR Spectroscopy,” *Org. Chem.*, pp. 1–8, 2012, [Online]. Available:

http://nmrweb.chem.ox.ac.uk/Data/Sites/70/userfiles/pdfs/quantitative-nmr.pdf.

[100] Sigma-Aldrich, “QUANTITATIVE NMR - Technical Details and TraceCERT® Certified Reference Materials,” *Sigma-Aldrich*, 2017, [Online]. Available: https://www.sigmaaldrich.com/content/dam/sigma-aldrich/docs/Sigma-Aldrich/Brochure/1/qnmr-brochure-rjo.pdf.

[101] G. Torre, “The Brain’s Building Blocks: Of Protons and Voxels.” 2017, [Online]. Available: https://knowingneurons.com/2017/09/27/mri-voxels/.

# RINGRAZIAMENTI

Dedico questa tesi al ricordo di mia nonna, colei che ancora prima che iniziassi il percorso di magistrale mi salutò augurandomi di non perdere mai la buona volontà e di continuare a impegnarmi in quello che credevo come mi aveva sempre visto fare. Nei momenti più bui di questi anni di studio è stato il ripensare a te che mi ha spinto a ritrovare le forze per andare avanti e a te va il mio più sentito ringraziamento poiché nonostante tutto non mi hai mai fatto mancare il tuo incoraggiamento.

Ringrazio di cuore la professoressa Francesca Bombelli Baldelli per l'opportunità concessami, dei consigli e delle spiegazioni datimi durante tutto il periodo e della disponibilità ad aiutarmi a chiarire ogni dubbio o incertezza, fossero essi di tipo professionale o personale. Ringrazio la dottoressa Linda Chaabane con lo stesso entusiasmo per tutto il tempo speso ad aiutarmi a comprendere meglio un campo affascinante ma complesso quale quello della risonanza magnetica e di tutti i consigli datimi che terrò sempre a mente nelle future esperienze che andrò ad affrontare.

Un caloroso ringraziamento va a Cristina, che nemmeno io so bene come abbia fatto a sopportarmi in tutti questi mesi. Grazie a lei ho imparato cosa significhi lavorare in un laboratorio di ricerca condividendo successi e fallimenti, osservandola al lavoro ho capito che l'impegno e la buona volontà possano battere ogni avversità e che l'importante è imparare qualcosa da ogni singolo risultato, indipendentemente dall'esito positivo di questo.

Ringrazio tutti i professori e i ragazzi del SupraBioNanoLab per tutte le risate nelle pause e gli aiuti durante il lavoro. Tra tutti un particolare ringraziamento va a Marta ed Andrea, per essersi sempre dimostrati disponibili a chiarire dubbi chimici e ad aiutarmi con dettagli e suggerimenti, e ad Alessandro, per la disponibilità infinita in ogni occasione. Spero, prima o poi, di poter lavorare nuovamente con voi

Di certo non possono mancare le persone che da sempre hanno contribuito, in maniera più o meno attiva, al rendermi la persona che sono. Mia madre e mio padre che comprendendo

ogni mio stato d'animo hanno sempre cercato di confortarmi e di lasciarmi i miei spazi quando necessario. Ringrazio mio fratello, che nonostante i percorsi diversi si è sempre dimostrato disponibile a supportarmi e ad offrirmi una diversa lettura della vita. Proprio grazie alle diverse esperienze che ci hanno condotto dove siamo arrivati siamo stati finalmente in grado di stringere quel legame che ora ci stringe. Un grazie in tutto questo va anche alla sua ragazza, Stella, che negli anni ha cercato di fare da ponte permettendo tutto questo.

Ringrazio la mia ragazza, Elena, per la pazienza dimostrata a sopportarmi in un periodo della mia vita sicuramente non tra i più facili e sereni. Mi hai sopportato 10 anni come amico e ormai sono 5 anni che stiamo assieme, sei forse la persona che mi conosce meglio avendo condiviso moltissimo in questi 15 anni. A causa della tua influenza ho scelto questa facoltà e solo per questo ti dovrei un immenso grazie, ma se mi limitassi a ringraziarti solo per quello sarei un fallimento come fidanzato. Le cose per cui ti dovrei ringraziare sono davvero troppe da elencare qua e sai che le smancerie non sono nemmeno il mio forte, quindi perdonami se mi limiterò a ringraziarti di tutto. Grazie di tutto ciò che sei e fai per me.

Ringrazio gli amici di una vita. Lorenzo, l'amico più caro e che da più tempo conosco. So che non lo accetterai mai apertamente perché sei più orgoglioso e chiuso di me ma ti ritengo davvero un fratello dopo tutti questi anni. Tara, sei sicuramente la persona con cui credo di aver legato un rapporto vero in così poco tempo da essermi stupito da solo. Sei una persona d'oro e non smetti mai di dimostrarlo. A voi vanno i momenti di pausa finito di studiare o di scrivere e le serate rilassate in compagnia utili a smorzare l'ansia e la stanchezza mentale. Chiara, grazie dell'aiuto sotto forma di parere o di materiale di studio, grazie delle sveglie nell'ultimo periodo e di avermi obbligato a lavorare alla stesura della tesi permettendomi di finirla in tempi brevi. A te vanno principalmente i momenti di studio più intensivi e qualche pausa meritata alla fine di lunghe giornate di studio. Andrea, Marco, Mattia e Toni, a voi che vicini o lontani mi avete sempre incoraggiato a fare del mio meglio e ad andare avanti per quella che ho deciso essere la mia strada.

A voi tutti, grazie di avermi aiutato a diventare la persona che sono e spero che la cosa vi renda fiero di me.

*Lodovico*